# SMALL COSMIC RAY AIR SHOWERS OBSERVED BY THE EXTENDED BUCKLAND PARK ARRAY

BY

CLAIRE LESLIE CORANI B.Sc. (Hons)

A Thesis
Presented for the degree of
MASTER OF SCIENCE
at the
UNIVERSITY OF ADELAIDE
( Department of Physics )

September 1986

Awarded 13/1/87

– TO MY HUSBAND, JOHN –

# STATEMENT

To the best of the author's knowledge and belief, this thesis contains no material previously published or written by another person, except where due reference is made in the text. It contains no material which has been submitted or accepted for the award of any other degree or diploma in any University.

Claire L. Corani
Adelaide
September 1986.

## TABLE OF CONTENTS

### CHAPTER ONE

### COSMIC RAYS

### CHAPTER TWO

### BACKGROUND FOR THE EXPERIMENT

CHAPTER TWO ( continued )

2.2 The "Knee" in the Spectrum

## CHAPTER THREE

## THE BUCKLAND PARK ARRAY

3.3 The New Array for Small Showers

## CHAPTER FOUR

### SIMULATIONS AND STATISTICAL CONSIDERATIONS

4.1 Simulated Performance Of The New Array

4.2 Statistical Considerations

## CHAPTER FIVE

### RESULTS

## CHAPTER SIX

APPENDIX 2
Shower Size Derivation

# ACKNOWLEDGMENTS

I would like to thank my two supervisors, Dr. Roger Clay and Dr. John Patterson for their bountiful encouragement, enthusiasm and patience. They have made the work both enjoyable and rewarding.

Professor John Prescott is thanked for his helpful comments and interest in the work, as is Dr. Ray Protheroe and other members of the academia of the Adelaide Physics Department.

The support that has been given by the technical staff of the department is gratefully acknowledged, in particular that of Neville Wild and Graeme Eames.

The Adelaide Physics department is renowned world-wide for its "super secretaries" and helpers. Thanks go to all of them for their friendship and help in times of crises, but most especially to my "co-athlete" Argy for typing the figure captions and never being too busy to help a friend in need.

The valuable assistance of Lawrence Campbell with the computing that was involved in this work is much appeciated, especially with the plotting routines. Thanks also go to Steven Marks for his excellent diagrams, David Bird for his data on maximum likelihood and Andre Phillips for the loan of his computer.

The C.R.G.G.C. ( Int.) must not be forgotten and thanks go to all members of that venerable institution that I have known, especially Greg Thornton, Dave Liebing, Peter Gerhardy, Bruce Dawson, Dominic Ciampa, Stephen Elton and Phillip Edwards.

My other co-students with whom I have shared many cups of tea ( and other drinks a little stronger ) have all afforded me friendship and have made my time as a post-graduate thoroughly enjoyable. These include Steven Gibson, Ron Craig, Lewis Jones, Nigel Spooner, Riaz Akber, Michael Hennessy, Mark Panizza, Tony Signal, Bruce Candy, Ruth Fazakerley, Phillip Fox, Peter May, ( and Alison! ) and the annual groups of toiling Honours students. A special word of thanks is also due to my very own Positive Reinforcement Officer, Damian Murphy, whose effort has earned the promised half glass of Scotch and who may even get a full one.

My parents, who have always encouraged me to do my best, deserve my sincere thanks. Finally my husband, John, who has helped in innumerable ways and put up with me for the duration, is lovingly thanked.

# ABSTRACT

The Buckland Park array has proved a very useful tool in studying the cosmic ray all-particle spectrum, in particular the feature at approximately 3 x $10^{15}$ eV known as the "knee". To further this work the array has recently undergone substantial extensions to enable showers with sizes down to 3 x $10^{4}$ particles at sea level to be studied.

This thesis discusses the motivation for the extensions and the experimental operation of the new Buckland Park array, with particular reference to the data collection and shower analysis. A number of possible analysis techniques have been studied and the advantages and disadvantages of these are presented.

# PREFACE

The author's work was undertaken at a time when the extensions to the Buckland Park cosmic ray air shower array discussed in this thesis, were past the design stage but before the experimental work involved in the extensions had been completed. As a consequence the project undertaken by the author contained as an integral part of its work a contribution to the construction of the extended array, including the installation of the array as well as the testing of the new detectors and final simulations of the expected array performance.

Once the array was commissioned, the author undertook the analysis of the raw data so that the air shower parameters could be extracted. Initially this involved finding the shower directions from the raw timing information. It then involved a study of the shower analysis methods available to find the core, shower size and age parameters from the raw density information.

Happy the Man

  Who studying Nature's laws,

Through known effects can

  Trace the secret cause.

Virgil: *Georgics*, Book II.

( Drydens's Translation ).

# CHAPTER ONE

# COSMIC RAYS

## 1.1 WHAT ARE COSMIC RAYS ?

Cosmic rays are high energy particles. These "primary" particles, which are thought to exist throughout the universe, can be detected near the Earth. They bombard the Earth, and interact with the atmosphere to produce showers of "secondary" particles, some of which reach ground level. Both the secondary particles and the incident primary particles are loosely termed cosmic rays.

Primary cosmic rays are mostly protons. They also consist of helium nuclei and some heavier nuclei. The exact composition of the cosmic ray flux varies with the energy of the particles and the investigation of this forms one of the main areas of cosmic ray research. Secondary cosmic rays consist of the products of interactions between particles and the atmosphere. These comprise further nucleons, electrons, positrons, photons, mesons and neutrinos, plus an assortment of rare sub-atomic species in small quantities.

## 1.2 A HISTORY OF THE STUDY OF COSMIC RAYS

The existence of cosmic radiation was first demonstrated when electrometers were taken above the Earth in balloons. Previously, workers had observed a gradual charge leakage in electroscopes (Wilson 1901). Their explanation was that the leakage was caused by weak radiation from nearby objects. However this explanation became doubtful when Hess (1912) and Kolhörster (1914) made balloon flights to measure the ionisation in air. They found that above approximately 1 km the ionisation level increased with altitude. Had the weak radiation been of terrestrial origin the opposite effect would have been observed. This was the first definite evidence of radiation from above the Earth's atmosphere, or "cosmic radiation" as it was termed by Millikan in 1926.

Further experiments, using both manned and unmanned balloons showed that at altitudes from approximately 1 to 20 km the ionisation level continued to increase to a maximum before decreasing above 20km (Pfotzer 1936). This was a mystery to early investigators in the field. Only when the true nature of cosmic rays became known could this feature (the "Pfotzer maximum" ) be explained.

Early investigators working on cosmic radiation were aware that they were studying two separate phenomena, namely primary and secondary radiation. However their understanding of the nature of these radiations was incorrect. They observed cosmic radiation high in the atmosphere and at ground level and found it to be very energetic. Consequently it became known as the "penetrating radiation" for many years. They believed that the primary cosmic rays were gamma-rays (γ-rays) as these were the most energetic rays known at the time. The supposed primary γ-ray passed through most of the atmosphere before giving up almost all of its energy to an atomic electron via Compton scattering. Electrons (β-rays) were known to cause ionisation in detectors and hence the recoil electrons from the Compton scattering were thought to be the observed secondary cosmic rays.

The main tool of this research on secondary radiation was the cloud chamber. With this instrument energetic β-rays (the supposed recoil electrons) were seen (Skobelzyn 1929). When Geiger-Muller counting tubes were used to study cosmic rays new evidence about their nature came to light. Bothe and Kolhörster conducted an experiment that placed doubt on the γ-ray nature of the ground level radiation. They put two tubes in coincidence, one above the other, and found that the tubes were frequently discharging simultaneously. It seemed unlikely that such "coincidences" could occur so frequently if these were due to secondary electrons being produced by separate γ-rays. This implied that the radiation was not composed of γ-rays but that it was composed of some form of charged particles. Bothe and Kolhörster concluded: "...each coincidence signifies the passage of one and the same corpuscular ray through both counters..." (Bothe and Kolhörster 1929). The experiments of Bothe and Kolhörster, and later work during the 1930's by Rossi ( as described by Rossi 1964 ) , showed that these particles were very energetic and hence must come from high in the atmosphere. These experiments, by placing great doubt on the existing theory of the nature of cosmic radiation, provided the impetus for much study into the true identity of both primary and secondary radiation.

We now know that when primary particles enter the atmosphere they produce cascades of large numbers of secondary particles, of which most are electrons and mu-mesons. The region where the greatest number of secondaries occurs is, on average ,at the height of the Pfotzer maximum, i.e. at ~ 20 km. This maximum is due mainly to low energy cascades and explains the early balloon observations. Larger cascades, with more particles produce what are known as Extensive Air Showers (EAS) at ground level. These EAS were discovered in 1938 by Auger, Maze and Grivet-Mayer. They used counters separated by several metres and with timing resolution improved to a few microseconds, they were still able to observe particles passing through their detectors simultaneously. These "related" particles indicated that a shower of particles had arrived at ground level. In further work Auger and his collaborators ( Auger et al. 1939 ) found coincidences with up to 300 metres separation, giving an indication of the extent of air showers.

The study of the nature of secondary radiation still continues. Work performed from the 1930's to the 1950's showed that there are not only electrons and mu-mesons present but positrons, $\gamma$-rays and neutrinos. There are also other more rare subatomic particles such as K-mesons and $\lambda$-particles as well as the various nucleons remaining from the primary's atmospheric interactions. The research into secondary cosmic radiation has resulted in the discovery and verification of the existence of many new particles. It contributed to the beginning of the field of elementary particle physics which now uses giant accelerators to further probe the nature of the nucleus.

Concurrent with research into secondary radiation further investigation was made into the nature of primary cosmic radiation. In 1927 Clay examined the variation of cosmic ray intensity with latitude and found the intensity at the equator to be 16% lower than at latitude 46° North. Compton produced a similar figure south of the equator (Compton 1932). This could not be explained if the primary cosmic rays were the supposed $\gamma$-rays ( as previously mentioned ) but could be if the primaries were charged particles. These particles would then be deflected by the Earth's magnetic field, so that fewer would arrive at equatorial latitudes.

These corpuscular charged primaries were initially thought to be electrons. However it was observed that an excess of particles came from west of the zenith as compared to the east. This showed that the primaries must contain more positively charged particles (e.g. Johnson 1933). Later it was shown that most of the primaries must be positively charged, and it was hypothesised that they were protons which then interacted in the atmosphere ( Schein et al. 1941). This protonic nature was confirmed by using nuclear photographic emulsions in high altitude balloon flights. Such emulsions produce a visible track for every energetic, charged particle passing through them; the density of the track and its associated scattering indicate the charge and velocity of the particle (Powell et al. 1959).

Using improved technology, the charge composition and energy spectra of low energy cosmic ray primaries have been the subjects of considerable study. Using nuclear emulsions primaries heavier than protons were seen. Electrons and positrons were found in the primary radiation (Earl 1961), as were X-rays (Giacconi et al. 1962) and y-rays (Kraushaar et al. 1968). Also found were nuclei heavier than iron, including uranium and transuranic elements (Fowler et al. 1967). However, these other constituents make up only a small part of the composition of the low energy primaries which are mostly protons. Above $10^{14}$ electron volts (eV) ( i.e. for higher energy primaries ) this is not necessarily true. Study of the exact quantity of other heavier elements such as helium or iron in the primary flux has provided a rich field of research.

## 1.3 THE COSMIC RAY ENERGY SPECTRUM

An energy spectrum shows how the cosmic ray intensity varies with primary particle energy. There are two common methods of representing the cosmic ray energy spectrum : the "integral" spectrum and the "differential" spectrum.

Figure 1.1 shows the integral spectrum. This displays the intensity of cosmic rays above a particular energy as the number of particles per square metre ($m^2$) per steradian (sr) per second (s), versus primary energy (E). The ordinate is commonly notated I(>E) and the measured spectrum can be fitted by the power law:

$$I(>E)\ dE \quad \alpha \quad E^{-1.8}\ dE$$

However it can be seen from Figure 1.1 that this expression will simply be an approximate fit to the observed spectrum. This is due to the large regions of uncertainty near $3 \times 10^{15}$ eV ( the "knee" ) and > $10^{18}$ eV ( the "ankle" ). The true cosmic ray energy spectrum (i.e. devoid of all observational error ) is probably not described by such a simple power law.

The other method of representation is the differential spectrum which is shown in Figure 1.2. This gives the intensity of cosmic rays per unit energy interval as the number of particles, per $m^2$, per sr, per s, and is generally notated as J.

If the relation between intensity and particle energy was a simple power law, a conversion could be made from an integral to a differential spectrum, as follows:

$$I(>E)\ dE \ \alpha \ E^{-x}\ dE \qquad \text{( integral form )}$$

$$\text{then} \qquad J(E)\ dE \ \alpha \ E^{-x-1}\ dE \qquad \text{( differential form )}$$

Consequently, the differential spectrum can be approximated by:

$$J(E)\ dE \quad \alpha \quad E^{-2.8}\ dE$$

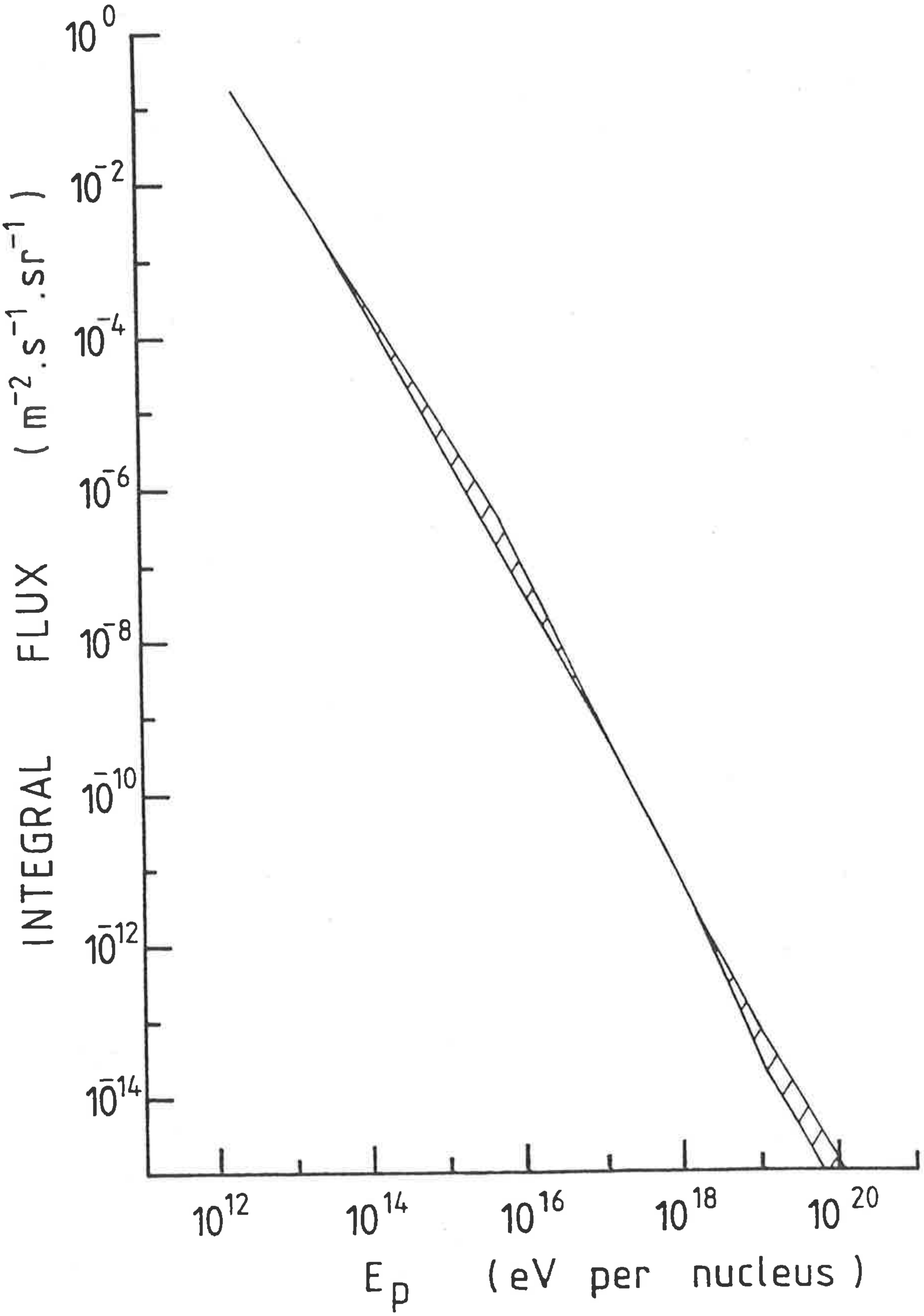

Figure 1.1 The integral spectrum for cosmic rays at the top of the atmosphere. The hatched areas indicate areas of uncertainty. (after Gaisser and Yodh 1980)

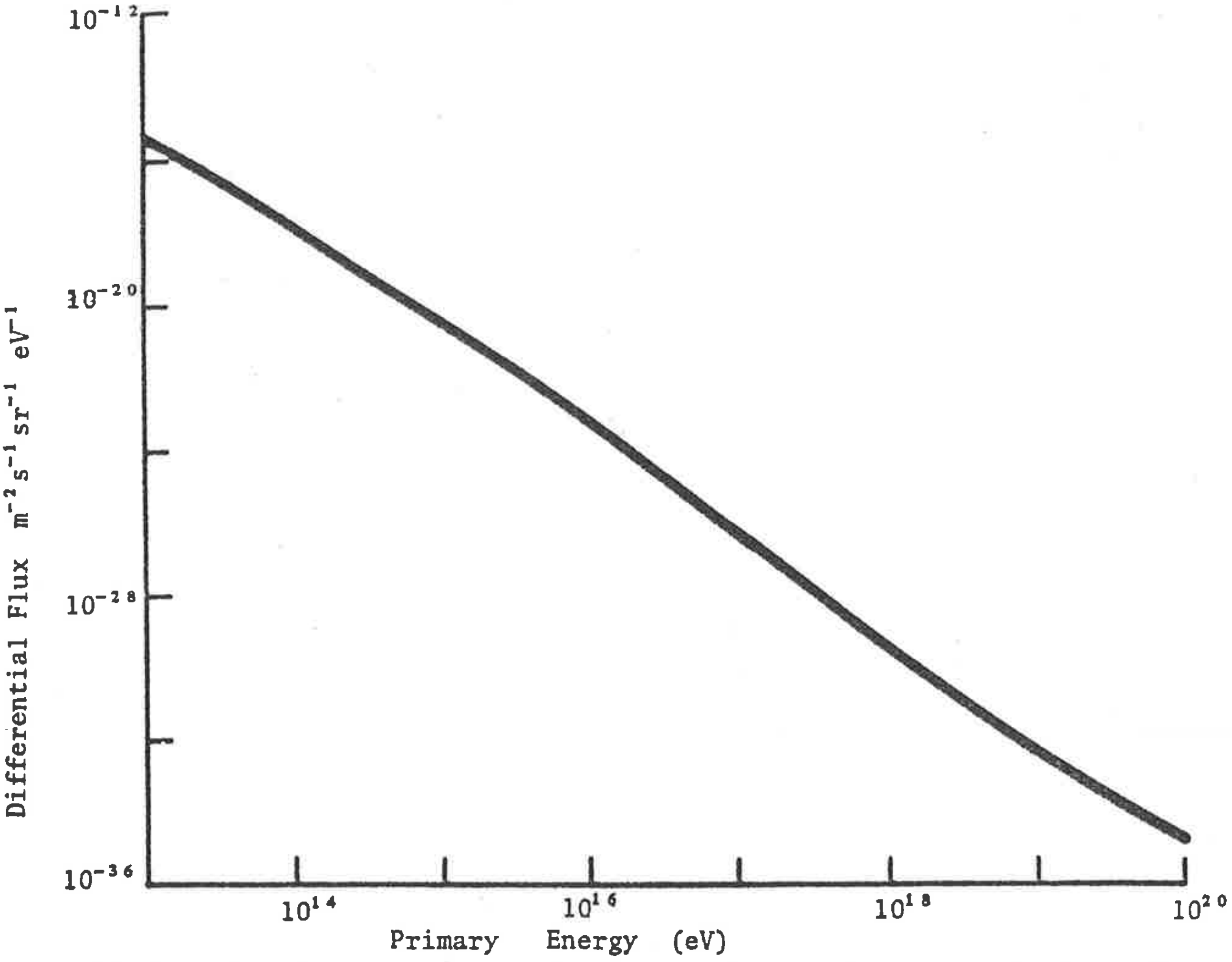

Figure 1.2 The approximate differential spectrum for cosmic rays at the top of the atmosphere. (from Gregory and Clay 1982)

On the spectra shown in Figures 1.1 and 1.2, deviations from simple power law behaviour are not readily seen due to the many orders of magnitude over which the intensity axes fall. To highlight these deviations the integral intensity can be multiplied by $E^{1.5}$. This flattens part of the spectrum whilst emphasising features such as the knee. Figure 1.3 shows results in this form from a number of workers.

## 1.4 EXTENSIVE AIR SHOWERS (EAS)

### 1.4 (a) Introduction

The energies of primary cosmic rays span a very large range, from $10^{9}$ eV up to $10^{20}$ eV. Part of this range is shown in the differential energy spectrum in Figure 1.2. The steep slope of the spectrum has resulted in limitations being placed on observational techniques. Due to the large number of primaries at very low energies ( those < $\sim 10^{13}$ eV ) direct measurements can made of these primaries from satellites and balloons. However, above this energy, the intensity drops to levels where such direct methods are not possible. For example, the intensity at a primary energy of $10^{16}$ eV is only 2 or 3 events per $m^2$, per sr, per year, while at $10^{19}$ eV the intensity is less than one event per $m^2$, per sr, per century! Fortunately, the cascades of particles in the atmosphere produced by primaries with energies above $10^{14}$ eV, are large enough to permit observable numbers of particles to reach ground level. The particles at ground level have considerable lateral extent and are known as Extensive Air Showers or EAS. Air showers resulting from primaries with energies between $10^{13}$ and $10^{14}$ eV can only be directly observed at high altitudes ( e.g. Morello et al. 1983 ) where significant numbers of electromagnetic component particles remain (as

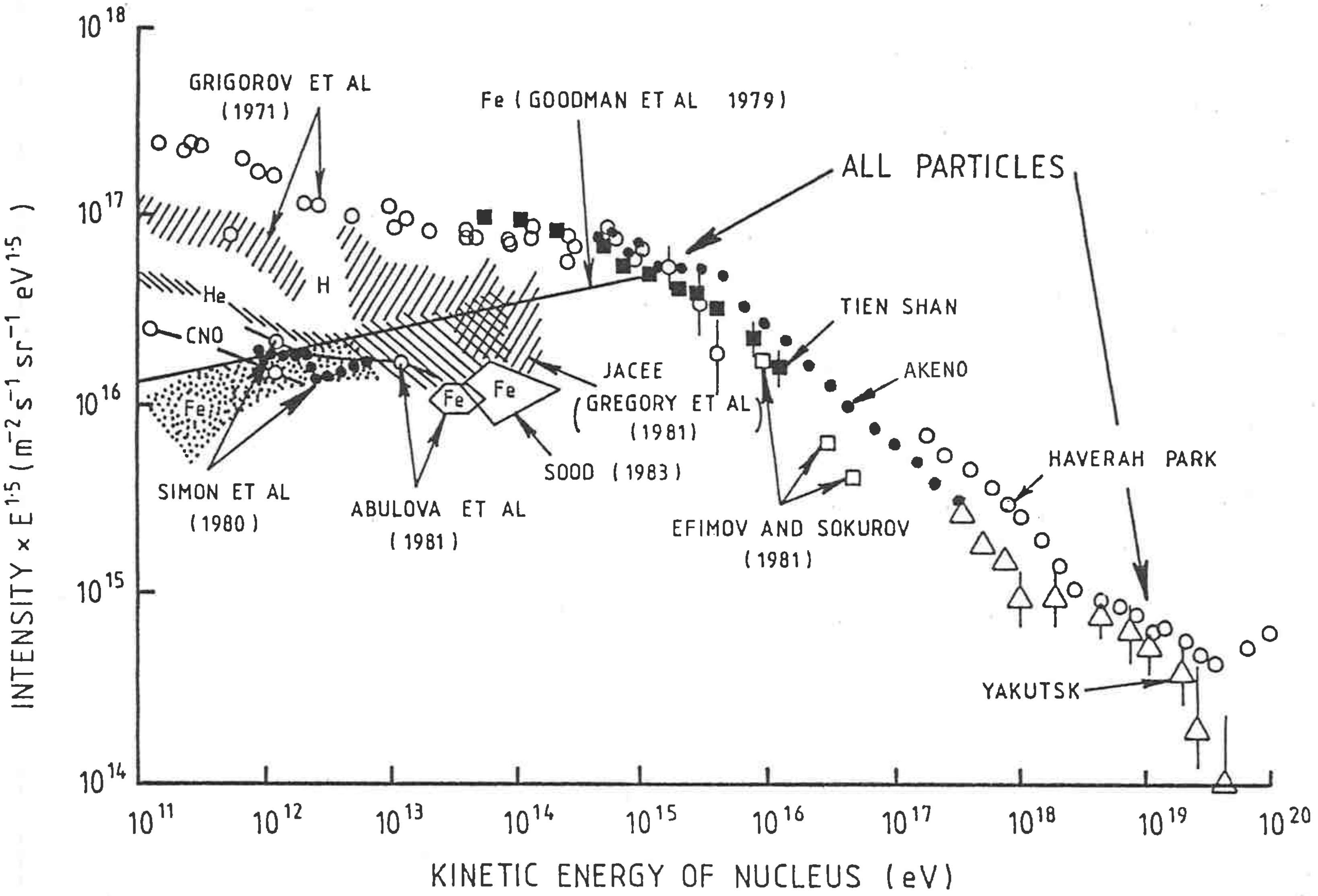

Figure 1.3 The integral intensity spectrum, multiplied by $E^{1.5}$. Various individual components in the low energy region are also shown. (After Hillas 1981a and Hillas 1984)

explained in section 1.4 (b) ). Consequently there is very little EAS data in this energy region.

The lateral spread of EAS permits their observation by arrays of appropriately spaced detectors which use coincidence techniques to sample the showers. EAS caused by low energy primaries require fewer, more closely spaced detectors than higher energy EAS which need more detectors spread over a larger area. Hence, though direct measurements cannot be made on primaries with energies > $10^{14}$ eV, it is still possible to effectively study them using EAS arrays.

### 1.4 (b) Shower Development

A shower is initiated when a primary cosmic ray collides inelastically with the nucleus of an atmospheric molecule. There are numerous products of this first interaction. These consist of the primary particle ( called the leading particle as it is usually still the most energetic), the fragments of the atmospheric nucleus (including nucleons and anti-nucleons) and a large quantity of $\pi$-mesons (called pions), as well as small quantities of rarer species. Three types of pions are produced, namely $\pi^0$, $\pi^+$ and $\pi^-$, in roughly equal proportions. Quantitative details of these collisions are unknown at energies $> \simeq 10^{14}$ eV as this is the limit for modern accelerators. ( The equivalent highest energy studied to date using the $Sp\bar{p}S$ accelerator at CERN is $1.5\times10^{14}$ eV (Eichten et al. 1984). While further experiments at laboratory energies of $2\times10^{15}$ eV have been performed, the results have yet to be finalised ). Hence quantities such as the inelasticity (the fraction of energy given up by the primary) and the multiplicity (the number of particles produced per interaction) can only be extrapolated from lower energy accelerator data at present.

The products of this first collision travel on, and either interact further or decay into other secondary particles. In this way the number of particles in the shower increases and the average energy of each particle decreases. This building process continues while the particles have sufficient energy to create new secondaries. When the average particle energy drops below the critical energy ( ~ 84 MeV in air ), ionisation takes over as the major energy loss process and the number of shower particles begins to decline. In this way a shower has a "maximum" particle number at a certain depth in the atmosphere, the depth being related to the energy of the primary. This "depth of maximum" is also dependent on the nature of the primary; a proton initiated shower will generally have a greater depth of maximum than a shower initiated by a heavier nucleus.

The superposition model can explain the dependence of the depth of maximum on the nature of the primary ( this model, however, is only an approximation ). A "heavy" primary such as iron can be considered as 56 nucleon primaries each with 1/56th of the energy of the iron primary. The initial collision breaks the iron nucleus into 56 nucleons which then initiate separate, overlapping showers. These showers are less energetic and so reach maximum higher in the atmosphere. The net effect is that the whole iron shower develops higher in the atmosphere. Hence the depth of maximum below the top of the atmosphere for an iron initiated shower is, on average, less when compared to a proton initiated shower of the same energy. Additionally, heavy nuclei have a larger nuclear cross-section for interaction and so interact earlier in the atmosphere which also contributes to the dependence of depth of maximum on nuclear species.

### 1.4 (c) The Decay Processes

The three pion species ( $\pi^0$, $\pi^+$, $\pi^-$ ) created by the primary's interaction decay via the following reactions:

$$\pi^0 \rightarrow 2\gamma$$

$$\pi^+ \rightarrow \mu^+ + \nu_\mu$$

$$\pi^- \rightarrow \mu^- + \nu_\mu$$

The $\pi^0$, or neutral pions, have a very short half-life, namely $\simeq 2\times10^{-16}$ s, and decay almost immediately into the two photons. These photons give rise to an electron-photon cascade known as the electromagnetic component of EAS. The half-lives of the charged pions are much longer ($2.6\times10^{-8}$ secs) allowing some to interact with further atmospheric nuclei before decay can occur. However, many of the charged pions decay into $\mu$-mesons or muons. High energy muons will be created only during the early development of the shower. These muons have a long interaction length and hence many arrive intact at the Earth's surface. The relatively few low energy muons produced in the later stages of shower development have time to decay to electrons and positrons which make a small contribution to the electromagnetic component of EAS. The decay processes for muons are shown below:

$$\mu^+ \rightarrow e^+ + \nu_e + \bar{\nu}_\mu$$

$$\mu^- \rightarrow e^- + \bar{\nu}_e + \nu_\mu$$

The neutrinos (symbol $\nu$ ) produced in most of these decays have essentially no cross-section for interaction with matter and so travel on through the Earth unimpeded.

### 1.4 (d) Major Components of EAS

There are three main components of air showers :

(1) The nuclear core ( also known as the hadronic core ),
(2) The "hard" or muon component,
(3) The "soft" or electromagnetic component.

Figure 1.4 is a schematic diagram of these three components.

### 1.4 (d) (i) The Nuclear Core

This consists of the hadronic disintegration products that result from the interactions between primary particles and atmospheric nuclei. The nucleons that emerge from these collisions interact further with atmospheric nuclei to produce more nucleons and secondaries, to form the energetic core of the shower. The charged pions formed in these interactions continue to either interact to maintain the core, or decay and so contribute to the muon or electromagnetic components.

The relatively high energies and large mass of the core particles leads to a small Coulomb scattering for these particles and so the core travels through the atmosphere as a narrow cone. For a typical $10^{16}$ eV shower the nuclear component at sea level comprises approximately 1% of the total shower particles and has a lateral extent of a few metres.

### 1.4 (d) (ii) The Muon Component

As seen from the decay processes in section 1.4(c), the muon component originates from the charged pions. Whether the charged pions decay or interact depends on two factors, namely the air density and the energy of the pion. In general the more energetic the pion the more likely it is to interact. However energetic pions are produced high in the atmosphere where the density is low (making interaction less likely) and so many of

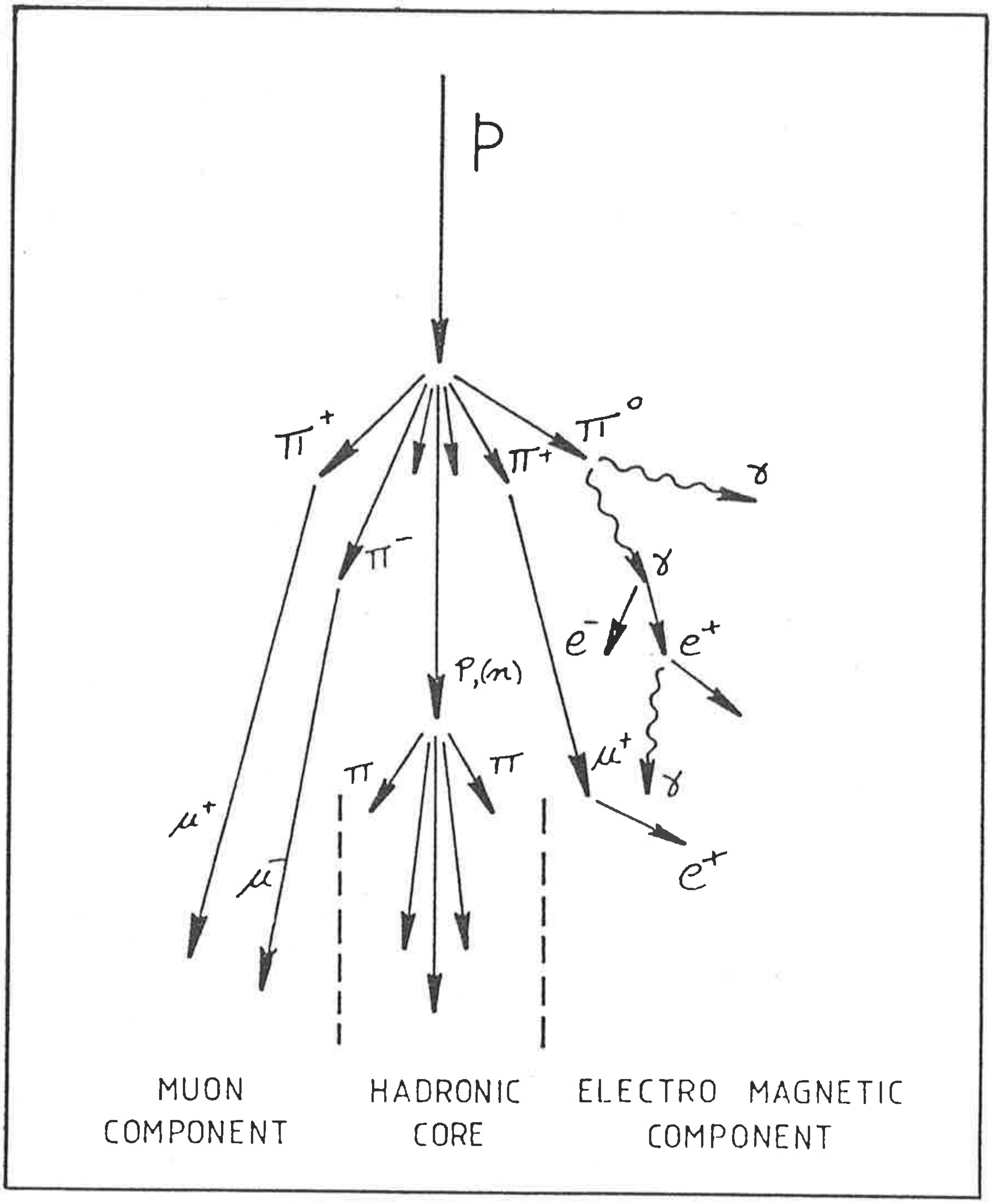

Figure 1.4 Schematic diagram of the major processes that occur in an EAS. The associated neutrinos have been omitted. (from Thornton 1984)

these pions can decay to muons. In this way high energy muons are created. These muons have small cross-sections for nuclear interaction and if their Lorentz factor is > 20 they have a very high probability of surviving to reach sea level, where they constitute approximately 10% of the particles in a $10^{16}$ eV shower. This survival is due to the time dilation of their $2 \times 10^{-6}$s life-time from the Earth's frame of reference. It is because these muons are very penetrating that they are called "hard" muons.

As the shower progresses, the muon numbers will continue to rise to a maximum as long as the nuclear cascade has sufficient energy to continue creating new secondaries. When the nuclear cascade dies out, no new muons are created and the number of existing penetrating muons stays roughly constant. The result is that the flux of high energy muons at ground level is the sum of all high energy muons produced during the whole cascade, and this can include muons produced as high as 20 km above sea level. Hence high energy muon measurements give information about early shower development and this technique is used by a number of groups ( e.g. Watson and Walker 1981, Kakimoto et al. 1985 ). Though muons have small Coulomb scattering and are not significantly deflected by the Earth's magnetic field, they still have a lateral spread at ground level of a few hundred metres due to their very high origin in the atmosphere.

### 1.4 (d) (iii)

### Electromagnetic Cascades and the Electromagnetic Component

The $\gamma$-rays from the $\pi^0$ 's interact with the atmosphere in two main ways, namely by pair-production or Compton scattering. For $\gamma$-rays in air with energy of $\simeq$ 20 MeV both processes equally contribute to the interactions whereas below this energy, Compton scattering dominates and above it pair-production is the dominant process. Pair-production refers to the process where an electron-positron pair is spontaneously created to replace the γ-ray. In the initial stages of most developing showers γ-ray energies are far in excess of 20 MeV and so pair-production is essentially the only process taking place. γ-rays can also interact with the atmosphere via the photoelectric effect but this process is only important towards the end of the cascade when the individual γ-rays are of low energy.

A similar situation exists for the electrons and positrons created from the process of pair-production. At a critical energy ($E_c$) of 77 MeV, ionisation of nearby atoms and bremsstrahlung equally contribute to the energy loss. Bremsstrahlung ( German for "braking radiation" ) describes the process where a γ-ray is emitted as the $e^-$ or $e^+$ is decelerated in the field of a nucleus. Below the critical energy ionisation dominates whereas bremsstrahlung dominates at higher energies. Again, in the early stages of development, the electrons and positrons produced are of sufficient energy to make bremsstrahlung the main process.

At energies much greater than $E_c$ the interaction lengths for pair production and bremsstrahlung are approximately the same, at about 36 g $cm^{-2}$. Hence a schematic diagram can be drawn to show the stages of cascade development only depicting the processes of pair-production and bremsstrahlung. This is given in Figure 1.5. As the cascade continues the number of particles doubles and the energy per particle halves with each interaction length. When the energy per particle has decreased to reach the critical energies for ionisation or Compton scattering, new cascade

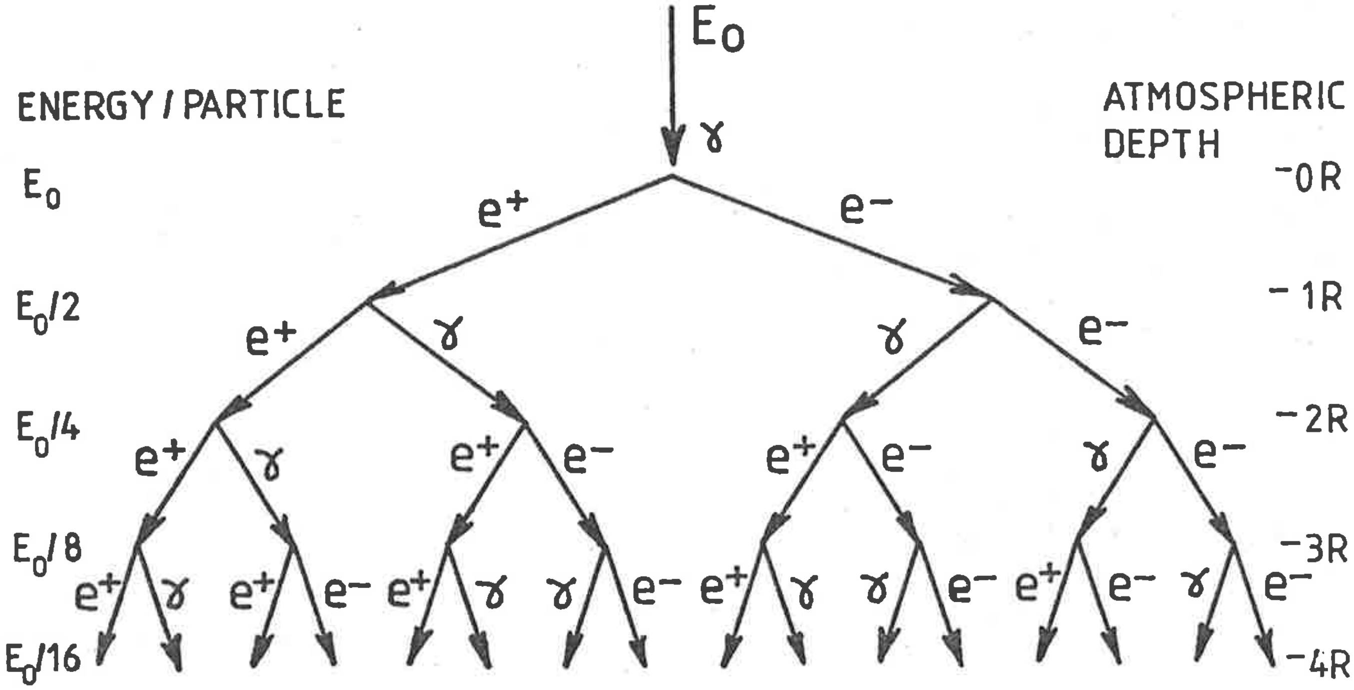

Figure 1.5 Schematic diagram showing the processes of pair-production and bremsstrahlung occurring in an EAS. (from Liebing 1983)

particles are not created and the cascade begins to die out. This simple model leads to some useful conclusions, such as the number of particles at maximum being proportional to the primary energy, and that the depth of maximum is proportional to the logarithm of this energy. Another useful result (Cocconi 1961) for real EAS with energies close to $10^{15}$ eV, is that the ratio of the sea level shower size to primary energy is $\simeq 10^{-10}$.

$$\text{i.e.} \qquad \frac{Ne}{E_o} \simeq 10^{-10}$$

This rough empirical relation which is useful at the energies used in this work follows from another of Cocconi's results: from a measurement of size at maximum development, the primary energy $E_o$ is given by:

$$E_o = N_{MAX} \times (1.3\times10^{9}) \text{ eV}$$

The processes described above are concerned with the mechanism of electromagnetic cascades. It is these cascades that form the third main component of EAS, the electromagnetic (e-m) component. For primary energies below $10^{14}$ eV the electromagnetic component of EAS is absorbed high in the atmosphere leaving only the muon component at sea level. However for primaries of energies greater than this, gradually more of the e-m component remains at sea level. A typical $10^{16}$ eV shower has approximately 90% of all its particles consisting of e-m particles, i.e. the photons, electrons and positrons described previously. Multiple Coulomb scattering is significant for this component and hence the particles are scattered well away from the axis of the shower. ( The shower axis is that path that the primary would have taken had it not interacted with the atmosphere ). This scattering results in the shower particles travelling down through the atmosphere as a shallow disc. The disc is of the order of a few hundred metres in lateral extent and a few metres thick with a radius of curvature of more than a kilometre. The highest energy particles are found concentrated at the front of the disc and near the axis.

The e-m component originating from the decay of $\pi^0$'s remains numerically dominant as long as the nuclear component has sufficient energy to generate new pions. The $\gamma$-rays produced from the $\pi^0$'s each initiate e-m cascades and so the EAS is the superposition of many e-m cascades. Hence, for a study of high energy EAS a good understanding of e-m cascade theory is needed. Fortunately a number of workers have studied this problem with the result that, while the nuclear processes in showers are not well known, the pure e-m cascades are well understood. EAS are not "pure" e-m cascades but, as this component is so dominant at high energies, it is a useful approximation to use equations describing e-m cascades for simulation and analysis of showers.

### 1.4 (e) Lateral Distributions: Moscow-MIT and NKG

From the theory of e-m cascades a lateral distribution function is used to describe the way the particle numbers vary with distance (r) from the core of the shower ( the point where the axis strikes the ground ). There are two commonly used lateral distribution functions. The first is the Moscow-MIT function ( e.g. Greisen 1960 ), initially formulated at Moscow University and then modified by the Massachusetts Institute of Technology group.

The Moscow-MIT function is:

$$\rho(Ne,r) = \frac{Ne}{2\pi r_o} \frac{e^{-r/r_o}}{r} \qquad m^{-2}$$

where $\rho$ is the particle number density at a distance r metres from the core, in particles per square metre,

r is the distance from the core in metres,

Ne is the number of particles in the shower at sea level ( the size of the shower)

and $r_o$ is a constant ≃ 60 metres.

The second important lateral distribution function is the NKG (Nishimura-Kamata-Greisen) function. Kamata and Nishimura (1958) formulated a theoretical function to describe pure e-m cascades and Greisen (1956) produced an empirical approximation to enable this function to be used for EAS. This function includes a new variable stemming from pure e-m theory. This is the "age" parameter known as "s". Every stage in an e-m cascade's development can be described by a particular value of s. S increases from zero to reach unity at the point of cascade maximum, and then increases from unity to two in the later stages of the cascade. This variable is well defined for a single pure e-m cascade but for an EAS, which is actually a superposition of many sequential cascades, s is not well defined. However there is value in assigning an age for each shower observed, as an indicator of the overall development that the shower attained. A small s ( <1 ) implies a "young" shower not yet at maximum development with a steep lateral distribution, while a larger s ( > 1) implies an "older", flatter shower which developed higher in the atmosphere. However, it must be remembered that s measurements for individual showers are not especially reliable. The age results are generally binned into shower size intervals to produce useful mean ages for various size ranges ( e.g. Abdullah et al. 1981 ).

The NKG function is:

$$\rho(Ne,r) = \frac{C(s)Ne}{r_o^2} (r/r_o)^{s-2} ( 1+ r/r_o )^{s-4.5} \quad m^{-2}$$

where $\rho$ is the particle number density,

$Ne$ is the sea level shower size,

$r$ is the distance from the core in metres,

$r_o$ is the Moliere radius $\approx$ 80 metres,

$s$ is the age parameter,

$$\text{and } C(s) = \frac{\Gamma(4.5 - s)}{2\pi\Gamma(s)(4.5 - 2s)}$$

where $C(s)$ is a normalising factor,

and $\Gamma(x)$ represents the Gamma function.

# CHAPTER TWO

# BACKGROUND FOR THE EXPERIMENT

## 2.1 THE COMPOSITION PROBLEM

### 2.1 (a) Low Energy Composition

The composition of primary cosmic rays above $\sim 10^{14}$ eV is still uncertain. In comparison, below $10^{14}$ eV, the composition of cosmic rays has been successfully studied using detectors carried on satellites and balloons. The relative abundances of elements in low energy cosmic rays are shown in Figure 2.1. Also, in Figure 1.3, results for individual elements can be seen.

When discussing composition measurements the energy of the species can be described in two ways, namely energy per nucleus and energy per nucleon. All energy values used so far have been given as energy per nucleus. A primary cosmic ray nucleus with any number of nucleons has a certain energy for the whole nucleus. This description is used for high energy cosmic rays where the number of nucleons is not known. In contrast, the identity of low energy primaries can be found from direct measurements as these yield the nucleon number and the charge of the nucleus. In these instances composition measurements are referred to in terms of constant energy per nucleon.

Table 2.1 shows the relative abundances of low energy cosmic rays at $10^{11}$ eV per nucleon at the top of the atmosphere. It can be seen from the table that protons are the main constituents

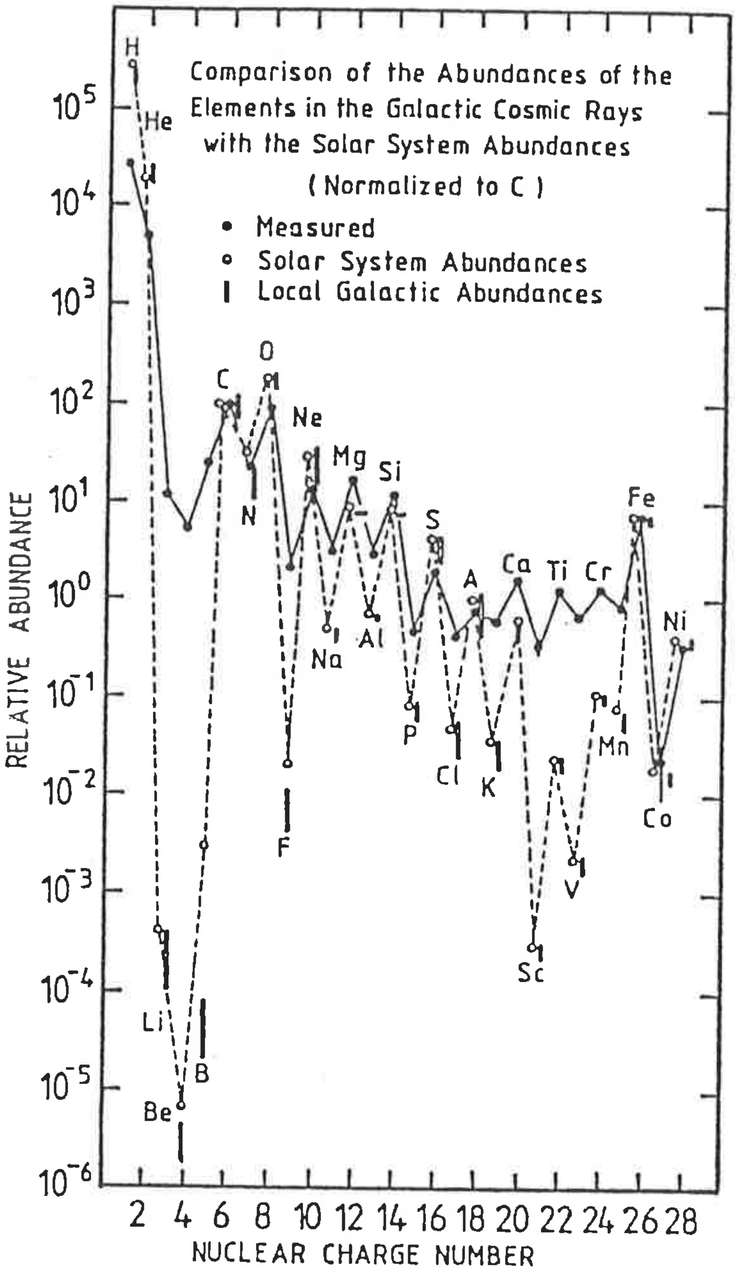

Figure 2.1 The relative abundances of the elements up to Ni of low energy cosmic rays. (after Müller 1982)

Table 2.1 Nuclear Abundances Below $\simeq 10^{11}$ eV Per Nucleon (from Hillas 1975 and Longair 1981)

| Z value(s) | Relative Composition Normalised to Carbon of 1000 | Percentage | Solar System % (*) |
|---|---|---|---|
| 1 (H) | 240000 | 85 | 93.4 |
| 2 (He) | 37500 | 13 | 6.5 |
| 3,4,5 (Li,Be,B) | 514 | .18 | $10^{-6}$ |
| 6,7,8,9 (C,N,O,F) | 2168 | .77 | .07 |
| 10 to 20 (Ne to Ca) | 652 | .23 | .019 |
| 21 to 28 (Sc to Ni) | 164 | .06 | .0027 |
| 29 =< Z =< 80 (*) | .06 | $2\times10^{-5}$ | $1.2\times10^{-6}$ |
| Z > 80 (*) | .001 | $3\times10^{-7}$ | $10^{-8}$ |

(*) - from Longair

of the low energy cosmic ray beam. Light nuclei (Li, Be, B) and heavy nuclei ( i.e. Z between 20 and 28) are both highly overabundant when compared with the solar system composition. The accepted explanation of this is the spallation (i.e. fragmentation) of heavier elements as they traverse and interact with the interstellar medium. Consequently the quantities of these spallation products can indicate the amount of matter that the primary nuclei have traversed since their production. Muller (1982) found a decrease in matter path length as the energy of the primaries increased. A possible explanation for this is that the more energetic cosmic rays are trapped within a larger confinement region near our galaxy which includes the less dense galactic halo. When spallation effects are removed, the cosmic ray source (CRS) composition can be found which is more similar to the solar system (SS) abundances. In fact, Meyer (1981) found the CRS composition very close to the composition of energetic solar particles, with the exception of carbon. Hillas ( 1983 ) in his overview stated that while some isotopic abundances are abnormal ( e.g. $^{22}$Ne ) the CRS composition is only slightly different to SS composition in that it may contain slightly more evolved material similar to that nearer the galactic centre.

The spectrum shown in Figure 1.3 contains composition information concerning specific elements in the low energy range. It shows the early composition work by Grigorov et al. (1971a). This was the PROTON series of satellites where each satellite carried a large ionisation calorimeter to measure the charge and energy of primary particles. These calorimeters had an energy cut-off which probably produced the steepening observed in the proton spectrum above $10^{12}$ eV (Ellsworth 1977). The JACEE experiment (Gregory et al. 1981) produced a proton spectrum that does not exhibit this steepening which is now thought to be correct.

At low energies ( $\simeq < 3\times10^{11}$ eV per nucleon ) many experiments on abundances have been performed (e.g. Simon et al. 1980, Dwyer and Meyer 1981, Engelmann et al. 1983, Barthelmy et al. 1985 ). Similarly, experiments on the spectra of individual elements at these energies have been done ( e.g. Chappell and Webber 1981, Israel et al. 1981, Burnett et al. 1985a). Above these low energies, up to energies near $\simeq 10^{14}$ eV per nucleon, only a few direct experiments have been performed such as that on the H and He spectra (e.g. Gregory et al. 1981, Burnett et al. 1982 ) and the iron spectra (e.g. Abulova 1981, Sood 1983, Streitmatter et al. 1985 ).

The lower energy experiments ( tens of Gev ) indicate that there are different spectral indices (i.e. different power law slopes on the spectrum) for the light and heavy nuclei. The logarithmic protonic spectrum has an integral slope of $\simeq -1.7$ whereas there is considerable evidence that the slope of the iron spectrum is in the range $-1.2$ to $-1.5$. (e.g. Simon et al. 1980, Sato et al. 1985, Engelmann et al. 1985 ). However at higher energies the spectrum appears to steepen, as the spectral indices for all nuclear groups approach $\simeq -1.7$ at an energy of $> 10^{11}$ eV per nucleon (i.e. $\simeq 6\times10^{12}$ eV for an iron nucleus) ( Webber 1982 ). This result is supported by the recent iron results of the JACEE collaboration ( Burnett et al. 1985b ).

When low energy composition results are examined in detail some areas of contention still exist. These include some discrepancies in the values for the nuclear abundances, the need for a complete explanation for the CRS composition and further improved statistics on the individual spectra. However, the fact remains that the wealth of accumulated data on the low energy cosmic ray composition gives quite consistent results. The same cannot be said for the high energy cosmic ray composition. At energies in excess of $10^{14}$ eV indirect methods must used due to the low fluxes. These indirect methods create large uncertainties in the composition results due to the variety of techniques used and the unavoidable selection effects which are present in such methods.

(Energy units are now given in eV per nucleus unless otherwise stated.)

### 2.1 (b) High Energy Composition

At energies around $10^{14}$ eV and above, the atmosphere becomes the cosmic ray physicist's detector. It can be considered as a giant ionisation calorimeter with a thickness of $\simeq$ 1000 g cm$^{-2}$. ( A g cm$^{-2}$ is a general unit used to describe the thickness of a layer of any sort of absorber; it is the mass of a column of unit area through the layer. )

As mentioned in Chapter One the nuclear physics of the collisions at these energies is not well known. A number of models have been proposed to extend nuclear interaction laws applicable at lower energies to the higher energy realm. The most common of these is termed Feynman scaling (Feynman 1969) in which the longitudinal momentum obtained by particles emerging from interactions is essentially independent of incident energy. In addition, accelerator work has shown that as hadrons approach high energies, their interaction cross-sections rise slowly. It is plausible to suppose that this trend continues to air shower energies. These two processes, Feynman scaling and rising cross-sections, have become the usual model for high energy nuclear interactions. The current highest energy data indicates minor violations of Feynman scaling at accelerator energies but major violations may occur at energies greater than $2\times10^{14}$ eV.

Feynman scaling results in a logarithmic dependence of multiplicity ( or secondary particle production ) on incident laboratory particle energy ( E ). Other models give a higher multiplicity with energy dependences of $E^{0.25}$ ( e.g. the CKP model as described by De Beer (1966) ) or $E^{0.33}$. To use these models to fit experimental data, a particular composition for the primary beam must be chosen. However no consistent picture has emerged from the various attempts to fit experimental data with interaction models.

Generally speaking the same data can be explained with a number of different models ( such as a heavy composition with scaling or a light composition with scaling violation ) but no model is capable of definitively explaining all available data. Wrotniak and Yodh (1985) after performing extensive simulations concluded that the air shower observables were more sensitive to the primary mass composition than the nuclear interaction model. However Kubiak et al. (1985) found that variation in primary composition could not reconcile their simulations with available data and that some scaling violation was needed. Rao (1983) assessed the evidence for scaling violation and decided that: "Whether or not scaling in the fragmentation region is valid in hadron-hadron collisions, it seems to be violated in hadron-nucleus interactions". He concluded that evidence for scaling violation is growing and that composition changes are occurring in the spectrum, but that the situation is far from resolved. Additionally work on high energy interactions has revealed that high energy particles do not emerge evenly from collisions but follow well collimated paths known as "jets" (e.g. Strugalski 1983 ). This phenomenon still requires further simulations to understand its effect.

Solving the composition of the cosmic ray beam and finding the correct high energy nuclear interaction laws are inter-dependent problems which make the study of the composition of high energy cosmic rays very difficult. A number of techniques have been developed which attempt to produce composition information independent of the nuclear interactions with varying degrees of success. The main aim has been to choose between two extreme compositions, either a continuation of low energy composition throughout the spectrum, or an enhancement of heavier primaries (usually iron) at about $10^{15}$ eV.

### 2.1 (b) (i) High Energy Muon Experiments

One method used to study composition is the examination of the high energy muons produced in the early stages of EAS. At the Tien Shan mountain observatory (at an atmospheric depth of 700 g $cm^{-2}$ ) workers have studied fluctuations in the ratio of muon density at a fixed core distance, to electron size. For a heavy primary this ratio should generally be larger. This is because the muon flux is relatively constant while the electron flux varies throughout the shower development and the usual earlier development of heavy primary showers will be reflected in a high muon to electron ratio. In the energy region of the knee, Tien Shan data is best fitted by a composition similar to that at lower energies (i.e. an iron component of about 15% ). The results do not support a scaling model but are otherwise model independent for a big class of hadron interaction models such as the CKP model. ( Stamenov et al. 1983 ).

elusive. Yodh et al. (1984) have examined some of the data that produces the conflicting results and have concluded that no consistent picture can emerge. They found that the data can be fitted by different composition assumptions and point out that muon observations, when grouped in terms of shower size rather than primary energy, lose much of the compositional information.

### 2.1 (b) (ii) Hadron Experiments

The arrival time distribution of hadrons in the cores of EAS is an area which has been extensively studied by the Maryland group. Goodman et al. ( 1982 ) had shown that the fraction of hadrons delayed by a particular time with respect to the shower front was a quantity sensitive to composition. Using both mountain and sea level experiments they were unable to reach a definite conclusion, but found that their data could be represented by two models. The first has a proton spectral index of -2.68 and an iron index of -2.39 in the range $10^{12}$ to $10^{15}$ eV. However this is discordant with low energy direct measurements as it produces too much iron at these energies. The other model has all nuclear components with a spectral index of -2.55 with them all steepening by 0.5 at a rigidity of $10^{14}$ V/c. ( Rigidity is a quantity which is used to characterise the path of a particle in a magnetic field. It is $P = pc/Ze$ , where p = momentum, c = speed of light, Ze = charge on species , expressed in volts. It is often given in the form of volts/c. Particles having the same rigidity follow identical tracks in magnetic fields, whereas particles with the same momentum or energy but different charges do not ). This second model is their preferred model and does have the advantage that it provides an explanation for the knee; this will be discussed further in section 2.2 (c). Both models produce a predominantly heavy cosmic ray beam at $10^{14}$ to $10^{15}$ eV.

Cowsik et al. (1981) provide further evidence for the compositions suggested by the Maryland group. These workers also investigated arrival times of hadrons and found, using Monte Carlo simulations, that their data supported a composition with an increasing proportion of heavy nuclei around the knee.

In contrast, Tonwar (1982) has surveyed high energy hadron data and concluded that a consistent interpretation in terms of a conventional nuclear physics model ( scaling with rising cross-sections ) with an increasing proportion of heavy cosmic ray primaries at $10^{14}$ to $10^{16}$ eV, cannot be found. In fact, Grieder (1984) has examined current high energy hadron spectral data from a number of sources and compared them with his theoretical calculations, and concluded that iron is not dominant around the knee region.

### 2.1 (b) (iii) Cerenkov Work

The observation of Cerenkov light is also employed in the study of cosmic ray composition. Cerenkov light is emitted from shower particles when they are travelling through a medium faster than the speed of light in that medium. It is analogous to a shock front and the light is emitted in a cone surrounding the particle. Cerenkov light is emitted throughout the life of the shower and consequently observations of the Cerenkov light flux can be related to shower development. Measurements of the Cerenkov pulse "full width at half maximum" (FWHM) lead to a value for the depth of maximum of a shower (Kalmykov et al. 1979). A number of workers ( e.g. Thornton and Clay 1980, Linsley and Watson 1981, Hillas 1981a , Dawson et al. 1985 ) find composition changes at the knee region from Cerenkov data.

These changes appear to be consistent with a shift from iron to protons as the dominant primaries over the range $10^{15}$ to $10^{17}$ eV, and the data supports conventional Feynman scaling models. However other Cerenkov work ( Alimov et al. 1983 , Aliev et al. 1985 ) does not agree with this interpretation. These results imply a constant composition from $10^{15}$ eV upwards.

### 2.1 (b) (iv) Other EAS Techniques

One technique which has had some success in the study of shower development, and consequently composition, is called the method of constant intensity cuts. The variation of shower size with zenith angle, at a constant shower intensity, is found. In the absence of fluctuations this is essentially equivalent to observing the same primary particle but at different depths in the atmosphere. Average shower development curves are drawn which show how the shower electron size varies with atmospheric depth. The data in the energy region of the knee matches well ( La Pointe et al. 1968, Antonov and Ivanenko 1975 ) with the theoretical development curve for iron as found by Gaisser et al. (1978) but not for their proton curve. Hence, this method supports a dominance of iron in the range $2\times10^{15}$ to $5\times10^{17}$ eV.

Another EAS technique employs the measurement of the density spectrum. This technique records the number of air showers which produce a given density in a certain area. This number is then plotted against the density. A power law index is found for these spectra which should reflect the size spectrum. An example of this technique is the work of Porter et al. (1981), where a slope change that could indicate the knee region was reported. Hillas (1981b) has analysed early density spectra experiments and concluded that with the assumption of no significant changes in nuclear interaction processes, primaries before and around the knee have a composition with =< 2% protons.

### 2.1 (b) (v) Very High Energy Composition

Primaries with energies in excess of $10^{16}$ eV produce large EAS and as the energy increases the steeply falling spectrum results in a very low event rate. Observations of the high energy spectrum are seen in Figure 1.3 and it can be seen that above the knee region the spectrum continues smoothly to $10^{19}$ eV ( the shin ?! ). After this energy some measurements show a flattening to form what is known as the "ankle". Giant EAS arrays, with enclosed areas of many square kilometres, are the only arrays capable of detecting events > $10^{18}$ eV. Examples are arrays at Haverah Park ( Bower et al. 1981 ), Yakutsk ( Krasilnikov et al. 1983 ), Volcano Ranch ( Cunningham et al. 1977 ), and Sydney ( Winn et al. 1986 ). All these arrays find an ankle in the spectrum to some extent except for Yakutsk which finds that the spectrum ends at $5 \times 10^{19}$ eV. Another array, employing a different technique to the existing large area arrays, is the University of Utah Fly's Eye detector (Baltrusaitis et al. 1985a). This array records the passage of high energy cosmic rays through the atmosphere via atmospheric fluorescence. The Fly's Eye group ( Baltrusaitis et al. 1985b ) has also recently reported an end to the cosmic ray spectrum in their data, at $7 \times 10^{19}$ eV, but they do observe a bump in the spectrum just before this cut-off.

The existence of the ankle could have important consequences in the debate on the origin of cosmic rays. If high energy primary cosmic rays originate outside our galaxy then their destruction by pion production induced by the photons of the $2.7^{\circ}$ background should result in no proton cosmic ray primaries above the energy of $5 \times 10^{19}$ eV. For iron primaries this cut-off should occur at higher energies ( $\sim 2 \times 10^{20}$ eV ) ( see Winn et al. 1986 for the relevant references ). However if high energy cosmic rays originate within or near our galaxy then, as the mean free path resulting from the destruction of cosmic rays by the 2.7° radiation is of galactic dimensions, no cut-off will be seen. Hence the evidence at present which tends to support the existence of an ankle at very high energies is also lending weight to a galactic origin for high energy cosmic rays, although the situation is far from resolved.

The limited amount of composition work at high energies tends to support a return to lower masses for the cosmic ray primaries. Andam et al. (1981) at Dugway, and Hammond et al. ( 1978 ) at Haverah Park, have found depth of maxima values to support this, as has Dyakonov et al. (1981) using Cerenkov lateral distributions. Overall most results imply a cosmic ray beam containing at least 65% protons. Similarly, Hillas (1984) points out that the large fluctuations observed in these high energy showers imply a high percentage of protons in the beam.

In conclusion, the various techniques which have been used to overcome the obvious difficulties involved in determining the high energy composition have been unable to produce a consistent picture. It is seen that a fair amount of disagreement exists between the results from muon work. The same can be said for the hadron experiments. Except for the Russian results the Cerenkov work appears the most consistent, favouring possible composition changes at the knee. However until considerably more agreement eventuates from all fields of research the high energy composition of cosmic rays can only be described as an uncertain quantity.

## 2.2 THE "KNEE" IN THE SPECTRUM

### 2.2 (a) The Shape of the Knee

Representations of the knee in the cosmic ray spectrum are seen in Figures 1.1 and 1.3. The fact that there is some feature at $\simeq 3\times10^{15}$ eV is beyond doubt, but the exact shape and cause of this feature are still unknown. The general consensus is that the mechanism that produces the knee will result in composition changes across the region. The knee appears as a sharp feature in Figure 1.3 but this is partly due to the compression of the intensity axis of the diagram. On the many decade plots in Figures 1.1 and 1.2 the knee appears as a very gradual slope change between $10^{15}$ and $10^{16}$ eV. The question arises as to the true shape of the knee. Is the knee a gradual change or is there is a sudden slope change which is consequently smeared out by observation procedures ? In addition, the Mt. Chacaltaya group have observed what has become known as a "kneecap". The upper dashed line in Figure 2.2 shows these results with a pronounced bump at the knee position. ( Kempa et al. 1974).

Hillas (1983) summarises work on the knee by considering two possible versions which follow from composition changes that have been observed.

(1) A "late knee" is produced when the proton flux falls away above $\simeq 3\times10^{15}$ eV, leaving a flux enriched in heavier nuclei and the iron component falling away at about $8\times10^{16}$ eV. Cloud chamber observations at Sydney (McCusker 1975) examining the structure of air shower cores, find steep cores associated with proton showers below the knee and flatter "heavier" cores at

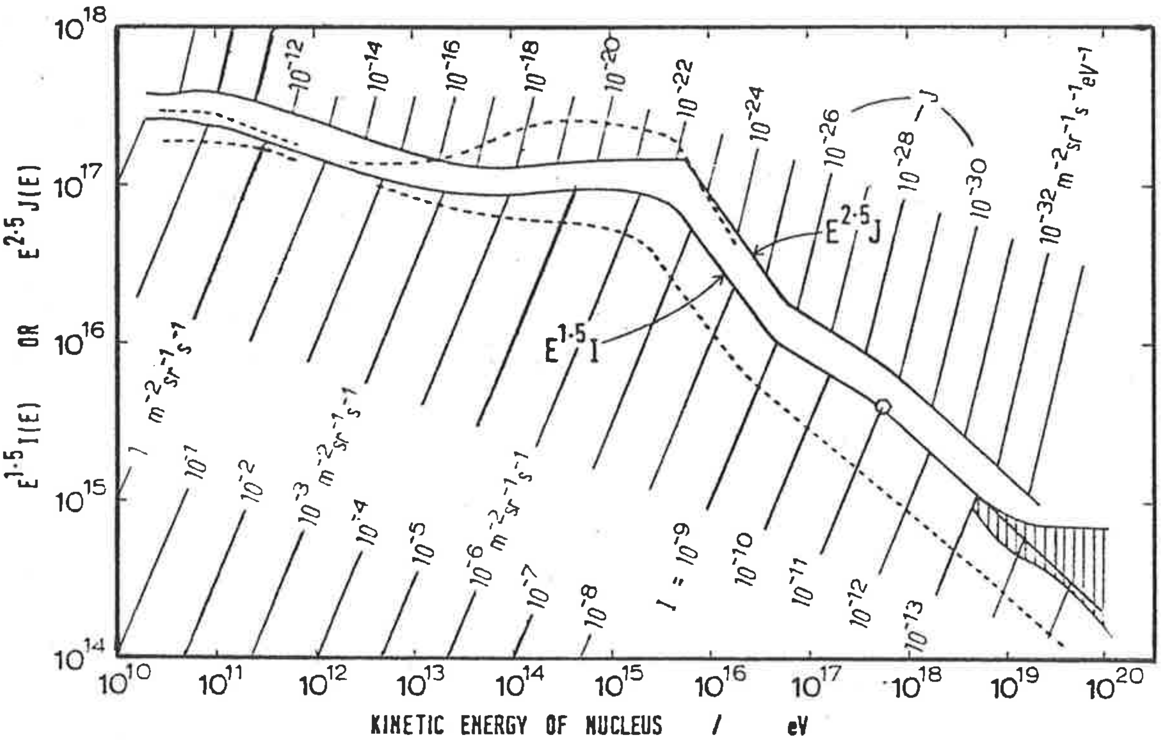

Figure 2.2 The energy spectrum of cosmic rays (from Hillas 1975) showing both the differential spectrum, J ( x $E^{2.5}$) and the integral spectrum, I ( x $E^{1.5}$). The dashed lines indicate the upper and lower extreme values of I, and the upper line from Kempa et al. (1974) indicates the possible "kneecap".

around $10^{16}$ eV. Hence they support a "late knee". Similar work performed at Leeds ( Hodson et al. 1983 ) supports this view.

(2) An "early knee" has the proton flux falling away at $\sim 10^{14}$ eV, with the iron component following at $3\times10^{15}$ eV. This form produces an iron dominance at the knee but requires an extra source of protons at higher energies. As already mentioned Cerenkov data supports this view as a dominance of iron at $\sim 10^{15}$ eV is found. This presumably implies that the proton component has fallen away well before this energy.

## 2.2 (b) Motivation for the Experiment

The author's work was undertaken to analyse the knee region, using the Buckland Park Air Shower Array. To do this the array was extended over the last three years to enable a superior analysis of the knee to be performed as well as improving the directional analysis. The original Buckland Park array had a sensitivity cut-off of $\sim 2\times10^{15}$ eV. ( By the relation expressed in Chapter One, at these energies this is $\sim 2\times10^{5}$ particles at sea level ). This had resulted in the region below the knee being inaccessible for an unbiassed study of the knee.

As mentioned in Chapter One, EAS of energies $10^{13}$ to $10^{14}$ eV are very difficult to observe as there are very few particles remaining at sea level in these small showers. Mountain altitudes are required and one of the few experiments performed in this region has been at Mt. Chacaltaya ( Morello et al. 1983). Similar, but not so extreme, difficulties are found in the region $10^{14}$ to $10^{15}$ eV ( $\sim 10^{4}$ to $10^{5}$ particles at sea level ). In this region a sea level site is suitable but the EAS are small in lateral extent and an array of closely spaced detectors is needed to analyse these events properly. Consequently many medium sized arrays find that the region below $10^{5}$ particles is outside their limits for a correct analysis. This has resulted in a relatively small amount of data in this region.

It was decided to "in-fill" the centre of the existing Buckland Park array to provide a region of closely spaced detectors able to analyse showers with sizes $< 10^5$ particles at sea level, with reliability close to 100% . ( See Chapter Three for a description of the Buckland Park Array and details of the extensions ). Additionally, accelerators are now attaining energies in the region of $10^{14}$ eV which will provide information on interaction processes, and so results should be less subject to some of the interpretive difficulties that plague higher energy work. These extensions to the array will enable the whole knee region ( up to the original array cut-off at $\approx 10^{17}$ eV ) to be analysed.

### 2.2 (c) The Origin of the "Knee"

Since the presence of a steepening of the energy spectrum at around $2 \times 10^{15}$ eV was first observed as early as 1958 in Moscow ( as reported by Vernov and Khristiansen (1967) ), a number of explanatory theories have been proposed. Suggestions have included:

(1) Changes or limitations in the acceleration mechanism at the source of the cosmic rays,

(2) A contribution from a different source of particles to produce a "bump" in the spectrum,

(3) The onset of an energy loss reaction, or most popularly

(4) A rigidity dependent escape mechanism.

### 2.2 (c) (i) Rigidity Dependent Escape Mechanisms

The rigidity dependent escape mechanism suggested by Peters (1961), and various modifications to it, have for many years been widely accepted as the cause for the knee. The mechanism allows particles to escape the magnetic fields of the local confinement region at a certain critical rigidity. Hence, assuming the confinement region to be the galaxy ( or our local part of it ) then protons which have the highest rigidity at a certain energy will escape first from the region. Iron nuclei which have the same rigidity at ~ 26 times this energy will remain contained to the higher energy and then begin to leak out from the region. Figure 2.3 shows a diagram of the knee region and the sketch on the top right illustrates the mechanism of Peters. It has been taken from an article by A. M. Hillas ( Hillas 1981a ) who has studied the data in the knee region extensively. He has produced a number of reviews which discuss the knee data and present the various models in diagrammatic form.

Employing the rigidity dependent escape mechanism results in the spectral bends of the other species falling somewhere between those for protons and iron. If the effects of all species are summed the result could be a gradual slope change over the knee region. A diagram indicating this concept is seen in Figure 2.4 taken from Hillas (1981a). The diagram is a representation of the Maryland composition which was discussed in the section on hadron measurements where all components have an index of -2.6 which steepens at a rigidity of $10^{14}$ V/c. It can be seen that the effect is a gradual slope change in the all-particle spectrum. The implied composition changes are also shown in the lower part of this figure.

However Hillas in a later paper (1983) points out a problem

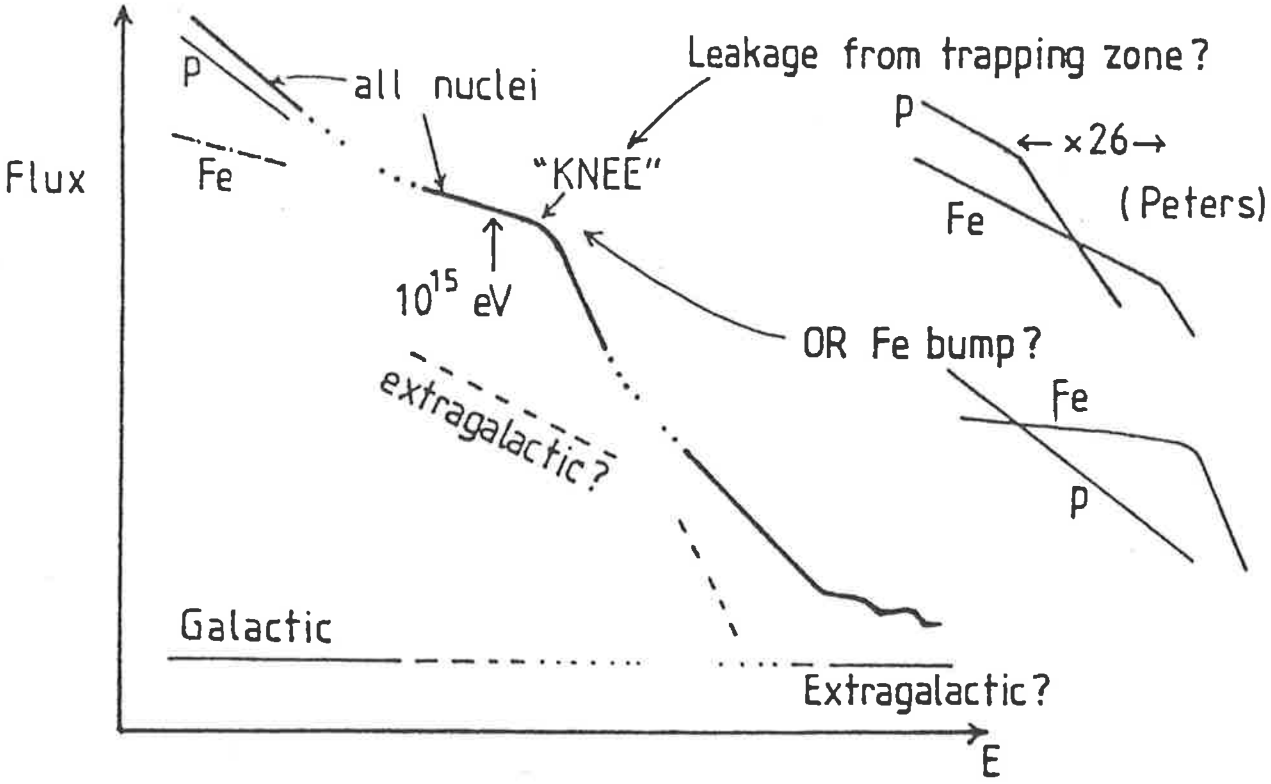

Figure 2.3 A "knee" diagram from Hillas (1981a) which shows two possible knee mechanisms.

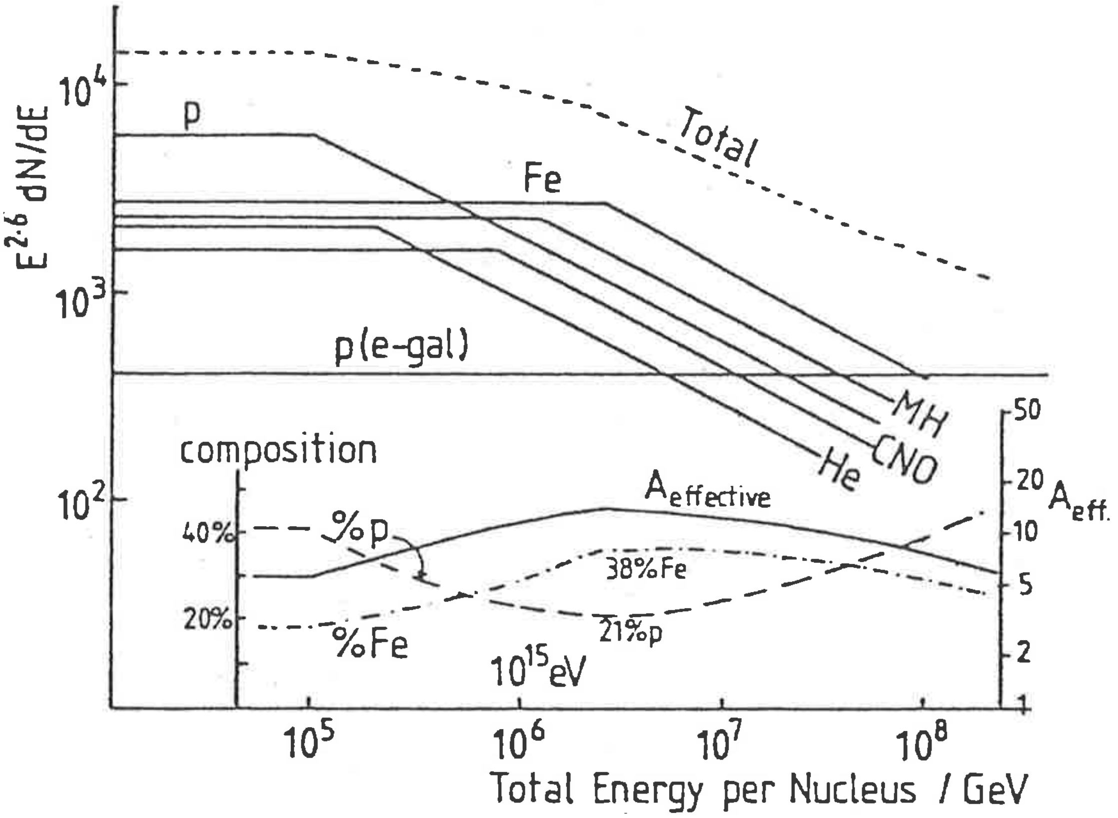

Figure 2.4 The spectrum produced by the "Maryland" (see text) composition, and the observed composition changes implied by this proposal. (from Hillas 1981a)

with this proposal. He finds that when the various components are summed a "transition region" is produced with a steep slope at the knee. Such a transition region is seen in the diagram of the Maryland composition in Figure 2.4 and is shown more clearly in Hillas's 1983 diagram given in Figure 2.5. Hillas points out that this transition region is not present in the observed cosmic ray spectrum ( also shown in Figure 2.5 ) using knee data from Proton-4 (Grigorov et al. 1971b) and Tien-Shan (Danilova et al. 1977). He states that variations in the slopes before and after the transition region or variations in the relative intensities of the component fluxes do not affect the slope of this region. The slope depends mainly on the position of the individual knees in the diagram which is determined by the nuclear charges. He concludes that the only way to prevent this transition region from occurring with this model is to assume a very different rigidity spectrum for just the proton component or not to employ the rigidity dependent escape mechanism at all.

Rigidity dependent escape mechanisms are often referred to as "leaky box" mechanisms. Our galaxy is the box and the associated magnetic fields induce the rigidity dependent leakage. One of the areas of contention in these models concerns the energy at which protons begin to leak out from the galaxy. Certain models propose an increasingly rapid loss of particles from the galaxy starting at rigidities as low as $10^{10}$ V/c. However Cowsik et al. ( 1981 ) point out that the flat source spectra at > $10^{12}$ eV predicted by these models are not observed. They prefer a model similar to that already mentioned as used by the Maryland group where all nuclei have indices of -2.6 and where rigidity dependent leakage occurs at ~ $10^{14}$ V/c. This is where the gyroradii of the cosmic ray particles becomes

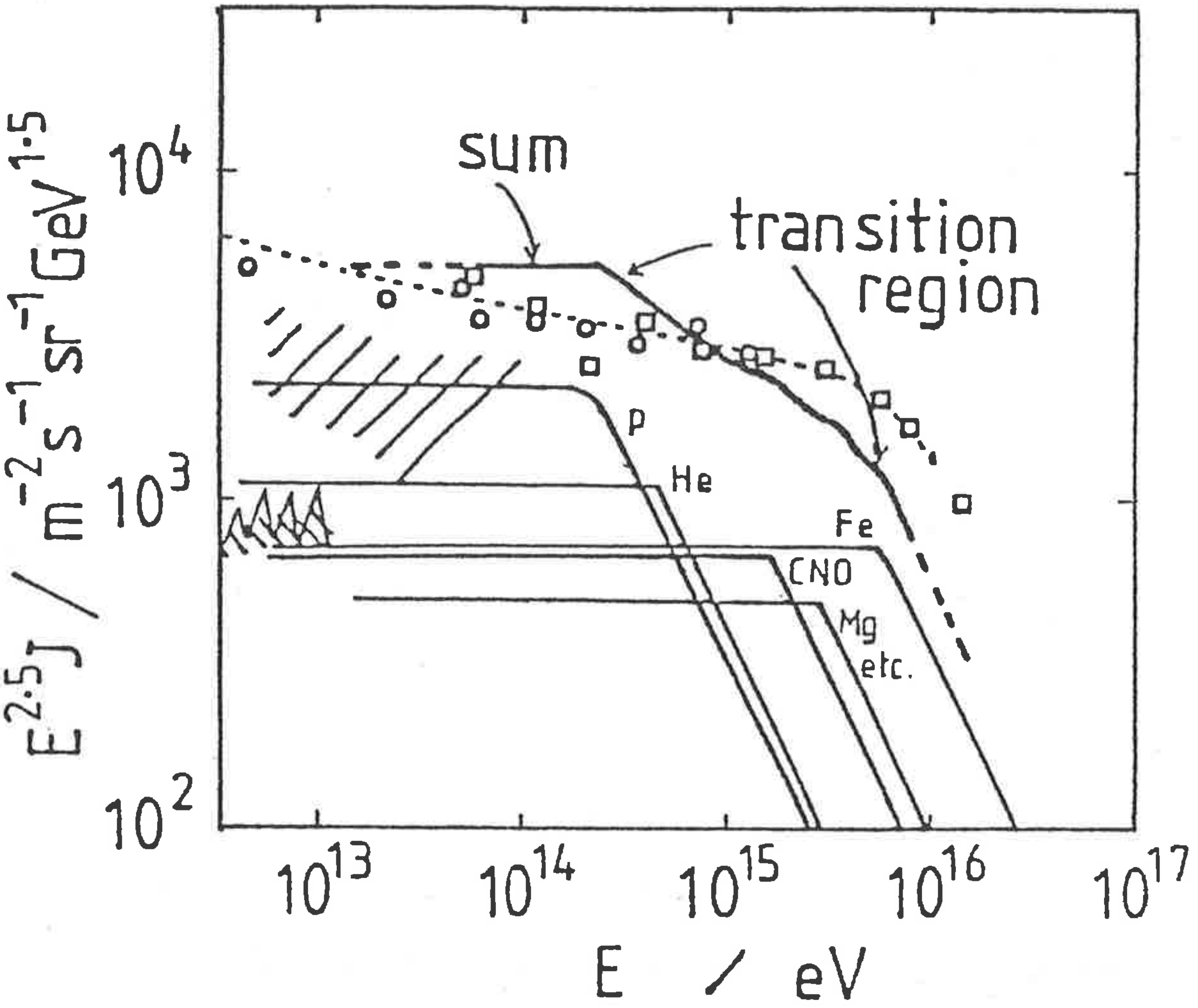

Figure 2.5 The spectrum produced by Hillas (1983). He sums several nuclear components with similar magnetic rigidity and contrasts them with the all-particle spectrum from Grigorov et al. (1971b) (circles) and Danilova et al. (1977) (squares).

comparable to the magnetic inhomogeneities in the interstellar medium.

Cowsik and Wilson (1973,1975) also suggest a model for the behaviour of the particles below the rigidity cut-off of at $10^{14}$V/c. They propose a "nested leaky box" and find that it explains the low energy spectral observations and the energy dependence of the relative intensities of cosmic ray nuclei. The cosmic rays are initially confined in a region near their source ( the inner box) and the leakage out from this region is rigidity dependent. Once the cosmic rays have escaped from the source region into the interstellar medium ( the outer box ) their subsequent leakage from this region is assumed to be independent of energy up to the $10^{14}$ V/c cut-off.

Other support for this model is given by Tang and Muller ( 1983 ) where they compare the spectra of cosmic ray primary electrons and nuclei. They use the nested leaky box model to produce an overall containment time of cosmic ray particles in the galaxy that is independent of energy. However, the amount of matter traversed by the cosmic ray is dependent on energy. This results from assuming dense inner box regions and much less dense outer box regions (where the solar system is located). They find their model adequately explains the observations that the containment of electrons in the galaxy is independent of energy as well as the energy dependence of cosmic ray nuclei path lengths.

The model proposed by Cowsik and Wilson (1975) should give a dominance of iron at the knee and hence is not favoured by workers who do not find such a dominance. For example Acharya et al. (1983) who find protons at knee energies favour different models. They prefer models which give an extra-galactic component of protons at energies above $10^{14}$ eV such as that by Cowsik (1968). This model had an protonic extra-galactic component taking over above the energy of $10^{14}$ eV which corresponded to the iron rigidity cut-off. Acharya et al. (1983) also suggest that their results support other models which do not rely on rigidity dependent escape.

Rigidity dependent escape mechanisms can possibly explain the knee feature observed in the spectrum but they need further additions to explain all of the available information. For example an explanation for the extension of the spectrum past $10^{17}$ eV is needed as rigidity dependent escape alone would give an end to the spectrum at about this energy. A popular suggestion is that a background of untrapped particles of extra-galactic origin underlies the galactic spectrum. However the flux of this extra-galactic component must be quite high to account for the intensity observed. Additionally, as mentioned in the section on high energy observations, if an ankle is present in the spectrum the extra-galactic component would need to originate from close to our galaxy to avoid destruction by the background radiation. A possible source is the Virgo cluster but there is some doubt as to whether it could provide the flux required (Hillas 1984).

An alternative hypothesis, instead of this additional extra-galactic component, employs very large magnetic fields which extend well outside the galactic disc. These magnetic fields induce a more gradual loss of particles from the galaxy and the large size of the magnetic fields enable particles with higher energy to be contained. (Hillas 1975)

Mechanisms that depend on a rigidity dependent escape for cosmic ray particles have been extensively studied as a possible cause for the knee. However the situation is still unclear and, as Hillas (1983, 1984) has pointed out, the simple leaky box model for the galaxy does not seem to apply. There is possibly an unknown factor causing the single step observed in the spectrum as opposed to the transition region he predicts. Similarly the direct observations of the iron flux, while not yet at the energy of the knee, do not seem to support an iron predominance in this region. Hence the situation is still unclear and alternative modulators for the spectrum must be considered.

### 2.2 (c) (ii) Alternative Causes for the Knee

Other proposed explanations of the knee consider effects that occur at the source which cause the changes in the spectrum. Very little is known about the source(s) of cosmic rays and how they are accelerated to such high energies. This has led to a speculative nature for alternative knee explanations which are based on source processes. Karakula, Osborne and Wdowczyk (1974) have suggested a "pulsar bump" theory where pulsars generate most of the cosmic ray flux, in the form of protons, at the knee region. Early pulsar theories ( Ostriker and Gunn 1969) suggested that pulsars should only produce particles up to an energy of $\approx 10^{16}$ eV. Similarly, at lower energies, $< 10^{14}$ eV, the pulsar spectrum is thought to be quite flat and hence will not give rise to features in the cosmic ray spectrum. Consequently, pulsars might produce an excess of particles between $\approx 10^{15}$ to $10^{16}$ eV, and so produce the knee. Figure 2.6 shows a "pulsar bump" model from Strong, Wdowczyk and Wolfendale (1974) where a galactic pulsar component overlies an extra-galactic flux. The exact height of the pulsar bump is not

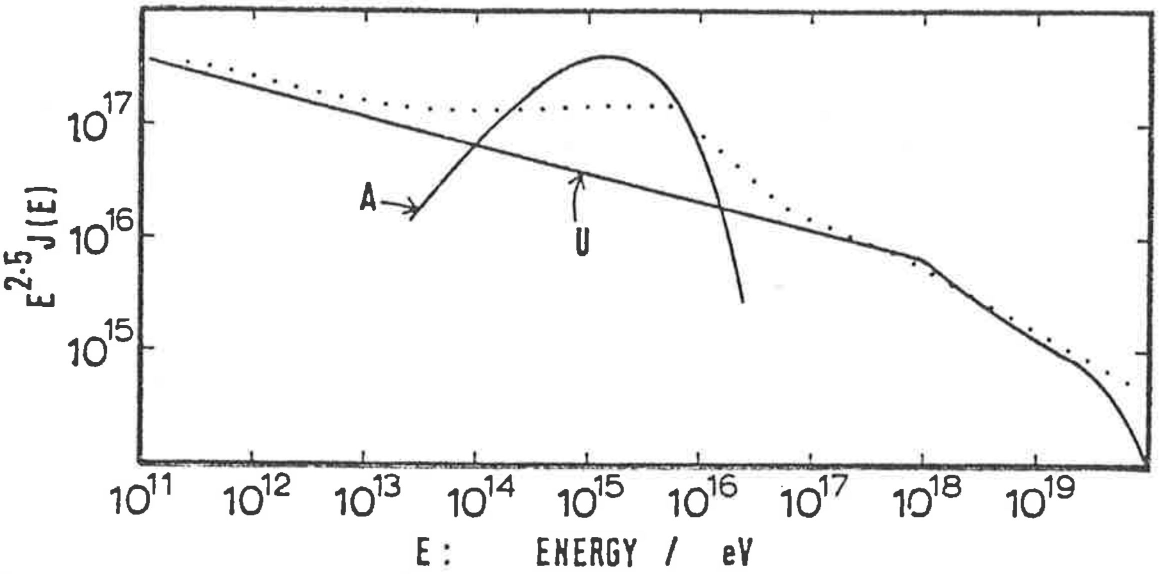

Figure 2.6 A suggested composite energy spectrum from Strong, Wdowczyk, and Wolfendale (1974) with a universal flux of protons, U, (with index = -2.75) superimposed on a galactic pulsar component, A. (from Hillas 1975)

determined and thus could provide a fit to the observed spectrum.

Another possible "bump" model is shown diagrammatically in Figure 2.3 on the lower right. This is a simple extension to low energy observations which indicate that the spectrum of iron could be considerably flatter than other components. If this flat spectrum continues to higher energies it would mean that iron would increase in predominance as the energy of the knee was approached. However the direct JACEE observation of the composition of the flux at their highest energies ( Ogato et al. 1981 ) indicated that, out of 21 observed interacting particles above $10^{13}$ eV, none appeared to be iron. This, along with more recent iron measurements ( e.g. that of Sood 1983 ) appears to rule out this model.

Other models, perhaps even more speculative in nature, involve energy loss processes. Bell et al. (1974) proposed the mechanism of diffusion of cosmic rays by "magnetised clouds" in the interstellar medium. Prior to the knee, these clouds deflect the cosmic rays, whereas above it this process becomes less effective. They suggest that the variation in scattering power of these clouds could affect the shape of the cosmic ray spectrum at the knee.

Another suggestion assumes that most cosmic rays are of distant extra-galactic origin which then undergo pair-production reactions with the microwave background radiation. These reactions could produce the observed knee ( Hillas 1968 ) but this approach is very speculative as it relies on information about the gas density and mass of the early universe.

Hillas (1979) has also considered another possibility. He cites evidence that spectra for different nuclei do not steepen at the same magnetic rigidity and that the steepening occurs at a higher rigidity for protons than for heavy nuclei. He suggests that the knee could arise from conditions near the source of the cosmic rays and may be the result of photo-disintegration due to the collisions between nuclei and photons. The heavy nuclei would experience this nuclear photo-disintegration at about $10^{14}$ eV whereas protons, for which this process does not occur, do not experience large energy losses until photo-pion production commences at $\simeq 10^{15}$ eV.

In conclusion, the origin of the knee is still a matter of debate. Doubts have been raised about the validity of traditional leaky box mechanisms but these are still preferred as no strong evidence in favour of the more speculative models has been found. Work on the composition of the region below and at the knee is required as is further information from areas such as the $10^{20}$ eV region, $\gamma$-ray work and anisotropies.

## 2.3 PREVIOUS WORK IN THE REGION < $10^{5}$ PARTICLES AT SEA LEVEL

As mentioned in section 2.2 (b) the shower size region below $10^{5}$ particles at sea level has received a comparatively limited amount of work. Very early work on this region was done using density spectrum measurements. This work ( e.g. Norman 1956, Prescott 1956, Reid et al. 1961 ) found that for densities < 500 particles $m^{-2}$ this spectrum followed a power law with exponent -2.5. Above this density the spectrum steepened. Further work found that the probable cause was a cut-off in the energy per nucleon of the primary particle.

Early EAS work ( other than density spectra ) done in the region below $10^{5}$ particles was performed at both Moscow State University ( e.g. Vernov and Khristiansen 1967 ) and Mt. Chacaltaya ( Bradt et al. 1965 ). The consensus from this work was that below $2\times10^5$ particles the differential number spectrum could be well represented by a power law with an exponent of $-2.51 \pm 0.09$. Beyond this the spectrum was steeper, with an exponent of $-3.2 \pm 0.12$. At the time the most accepted opinion was that this steepening resulted from the cosmic ray beam becoming enriched with heavy primary nuclei at a size of $\sim$ $2\times10^5$ particles, (e.g. McCusker 1967 ).

In 1970 Hillas examined and summarised current results on the size spectrum and concluded that below $2\times10^5$ particles, the best fit size spectrum obtained from EAS array techniques was given by: $J(N)\,dN = 47\,N^{-2.46}\,dN$. McCusker (1967) states a similar result as being well established, namely that the index of the differential size spectrum up to $2\times10^5$ particles was $-2.51 \pm 0.09$ . However, these apparently definitive results had only been based on the small amount of work that had been done up to that time. More recently, other workers have attempted to examine the spectrum and have not found confirmation of these early results.

Below is a list of results obtained by various groups. The earliest expression is essentially from Hillas's 1970 summary ( actually from Ashton et al. 1979a who employed and re-graphed Hillas's work). Hillas used low energy data from Moscow ( Vernov and Kristiansen 1967 ) and Mt. Chacaltaya ( Bradt et al. 1965) in his summary.

| <u>Work</u> | <u>Range</u> | <u>Differential Spectra</u> | <u>Error Information</u> |
|---|---|---|---|
| Hillas's summary of EAS data (1970) | $<7\times10^5$ | $J(N)\,dN = 47\,N^{-2.46}\,dN$ | error of $\pm$ .01 on integral slopes |
| | $>7\times10^5$ | $J(N)\,dN = 7\times10^4\,N^{-3}\,dN$ | |

| Work | Range | Differential Spectra | Error Information |
|---|---|---|---|
| Catz et al. (1975) | $<10^6$ | $J(N)\,dN = 270\,N^{-2.59}\,dN$ | error of ± .02 on integral slopes |
| (Verrieres le Buisson) | $>10^6$ | $J(N)\,dN = 1.6\times10^6\,N^{-3.19}\,dN$ | |
| Ashton et al. (1979a) from density spectra | $< 7\times10^5$ | $J(N)\,dN = 3.9\,N^{-2.9}\,dN$ | error of ± .01 on integral slopes |
| | $> 7\times10^5$ | agreed with Hillas (1970) | |
| Asakimori et al. (1981)<br>EAS work at Kobe | $5\times10^4$ to $10^6$ | integral spectrum<br>$I(N) = (5.4 \pm .4)\times10^3\,N^{(-1.85\pm\,.06)}$ | |
| (no knee observed) | | differential spectrum<br>$J(N)\,dN = 10^4\,N^{-2.85}\,dN$ | |
| Nagano et al. (1984) | $10^5$ to $10^6$ | $J(N)\,dN = (104 \pm 17)\,N^{(-2.49\,\pm\,.17)}\,dN$ | |
| EAS work at Akeno | $10^6$ to $10^8$ | $J(N)\,dN = (7.6\pm1.3)\times10^3\,N^{(-2.8\,\pm\,.12)}\,dN$ | |
| Sun Louri and Winn | $< 3\times10^5$ | $J(N)\,dN = 0.52\,N^{(-2.15\,\pm\,.04)}\,dN$ | |
| (1984) | $> 3\times10^5$ | $J(N)\,dN = 6920\,N^{(-2.91\,\pm\,.08)}\,dN$ | |
| Chan and Ng (1985)<br>(no knee observed) | $6\times10^3$ to $10^6$ | $J(N)\,dN = 2920\,N^{(-2.79\,\pm\,.11)}\,dN$ | |

These differential spectra are shown in Figures 2.7 (a) and (b). Most groups observe a knee in their data although its location varies from ~ $3 \times 10^5$ particles up to $10^6$ particles. Two groups, Asakimori et al. and Chan and Ng, find no evidence for a knee. Asakimori et al. find the highest values for the differential rates in the region below 5 x $10^5$ particles whereas Nagano et al. at Akeno find the highest rates above this size. Sun Louri and Winn's rates are the lowest over the whole size range.

Even though there is some disparity between the results of various groups, the overall results appear uniformly distributed and it is quite probable that the true spectrum is encompassed by this spread of results. Similarly, even though two groups find no knee in their data, the bulk of the work shows a knee feature and the probability that a knee is not present in the true spectrum must be quite small.

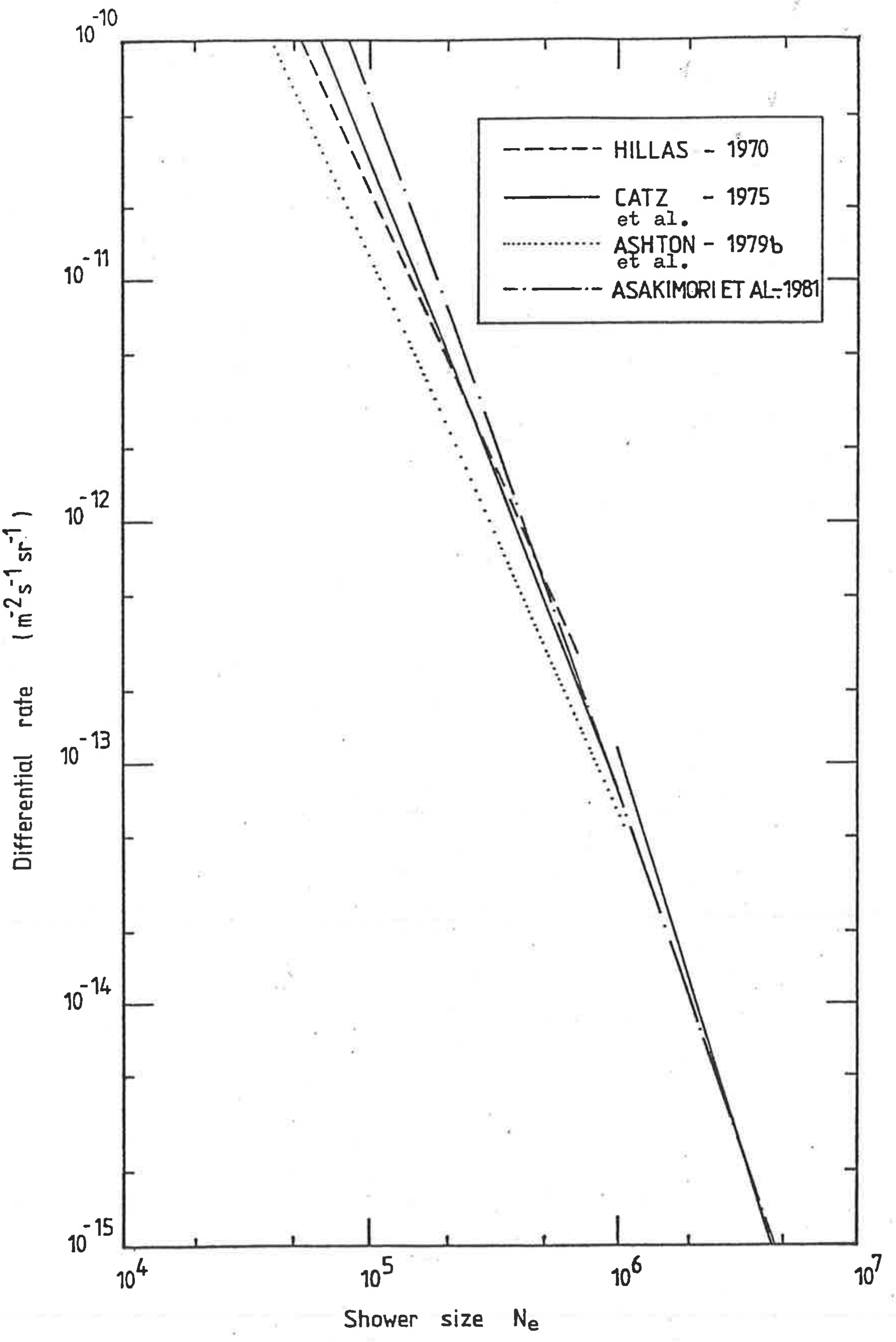

Figure 2.7(a) Differential spectra observed by various workers. (see text for details)

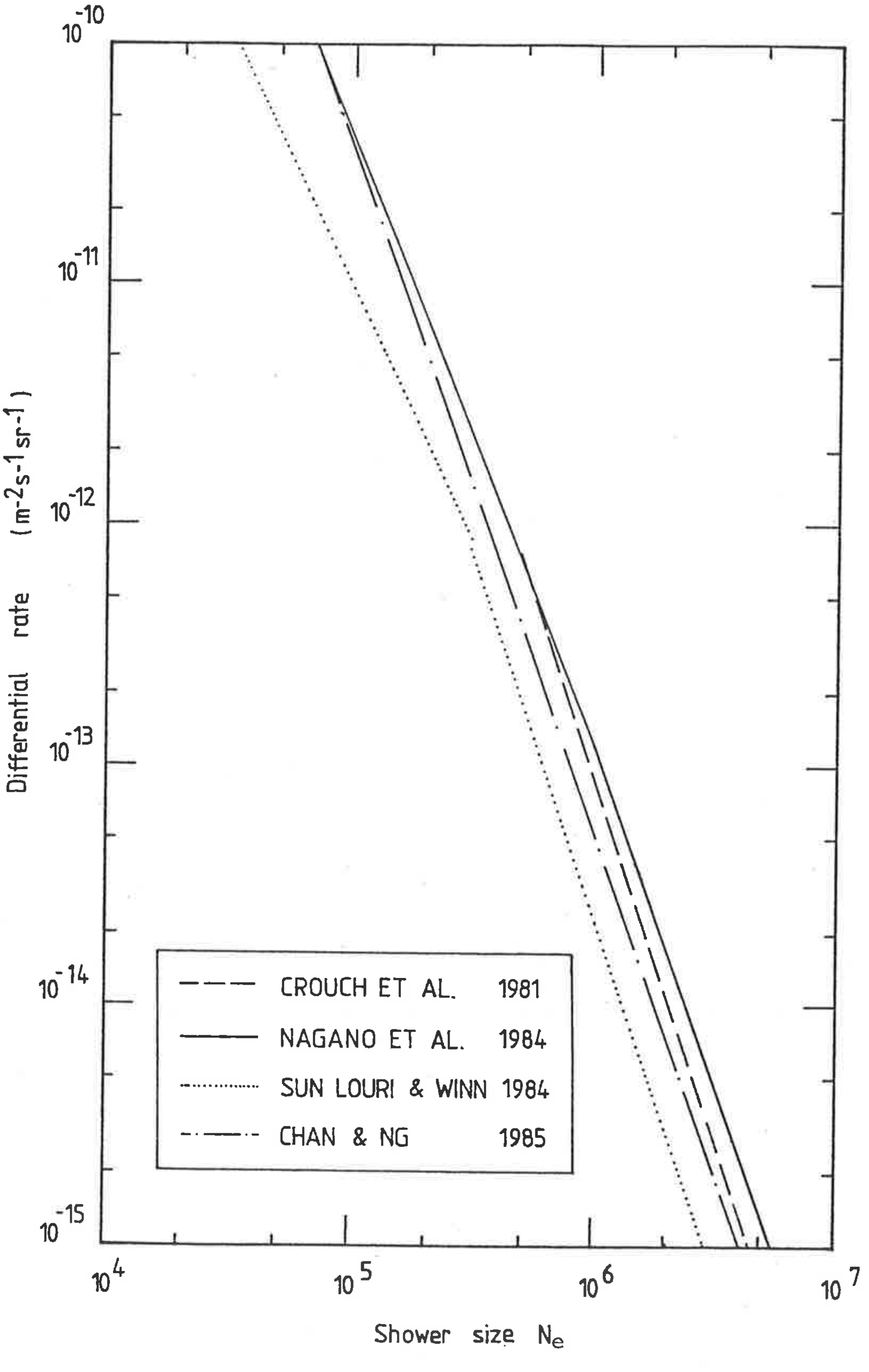

Figure 2.7(b) Differential spectra observed by various workers. (see text for details)

# CHAPTER THREE

# THE BUCKLAND PARK ARRAY

## 3.1 INTRODUCTION

The Physics department at the University of Adelaide has a field station at Buckland Park, approximately 40 km north of Adelaide. It is situated almost at sea level on a flat coastal plain near the mouth of the Gawler river with longitude of 138° 28′ East and latitude of 34° 38′ South. The location of Buckland Park is shown in Figure 3.1.

A cosmic ray EAS array has been in operation at Buckland Park since 1971. It has been used to study EAS at the sea level size range of $10^5$ to $10^7$ particles. Cerenkov and scintillation detectors have been employed in studies of size spectra ( e.g. Clay and Gerhardy 1982a), air shower development and composition using Cerenkov depth of maximum techniques ( e.g. Thornton and Clay 1981, Liebing et al. 1984, Dawson et al. 1985 ) and anisotropies ( e.g. Clay and Gerhardy 1982b ). The depth of maximum work has yielded useful information on primary cosmic ray composition in this size range. The results found are consistent with a change from mainly iron primaries at shower sizes of $10^5$ particles to mainly protons at $10^7$ particles. The anisotropy work showed a small Right Ascension anisotropy ($\sim$ 1%) and an upper limit for the Declination anisotropy of $\sim$ 3%.

In addition the work of the Adelaide group has expanded to include γ-ray astronomy. Existing data was examined by searching for periodicities from interesting sky areas ( e.g. in the vicinity of a binary X-ray source ) which led to the exciting discoveries of two γ-ray sources, Vela X-1 ( Protheroe et al.

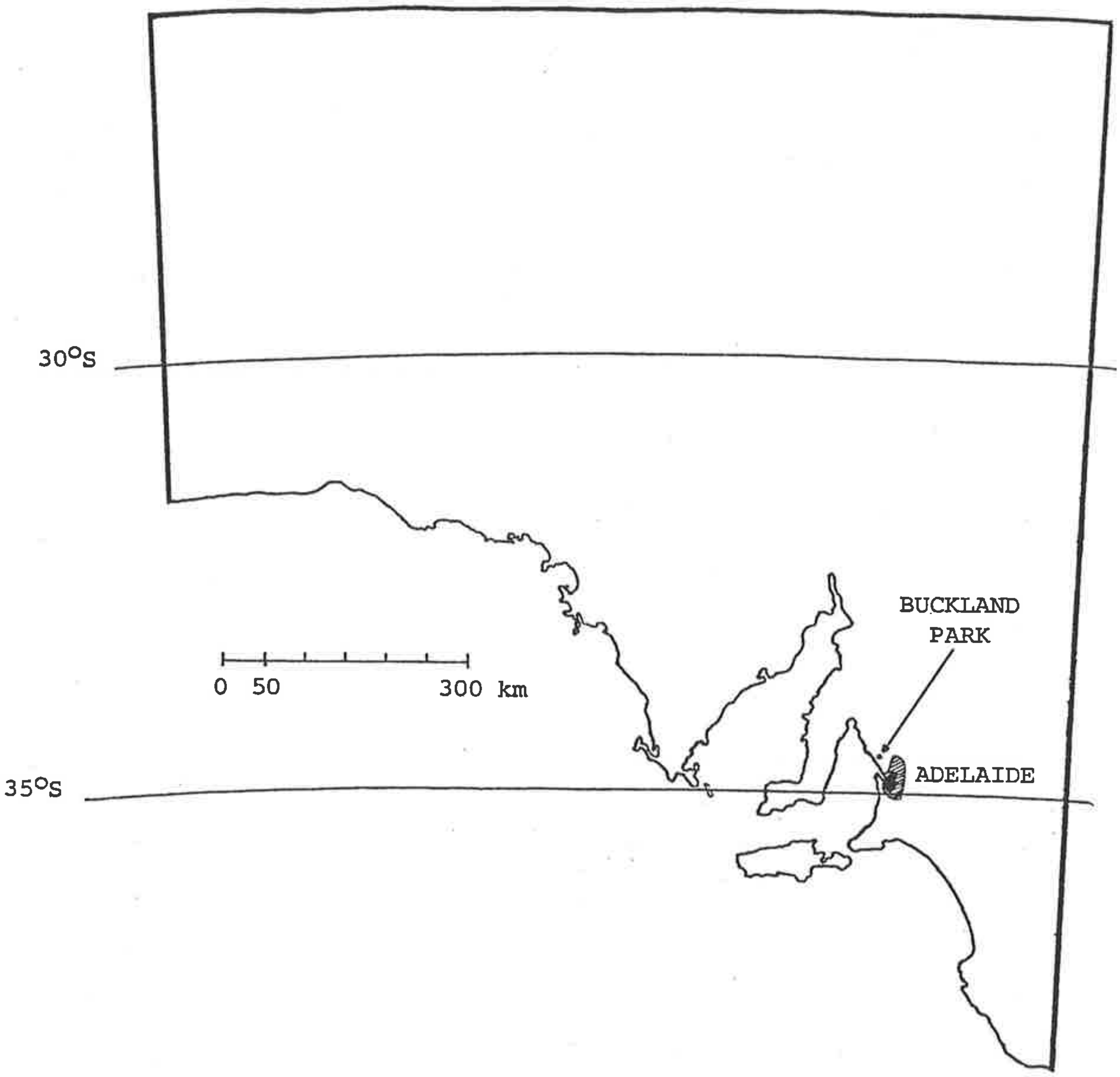

Figure 3.1 A map of South Australia showing the location of Buckland Park.

1984 ) and LMC X-4 ( Protheroe and Clay 1985 ). As the directional analysis system of the array is improved, the location of sources will be more accurate and this will facilitate $\gamma$-ray work in the future.

## 3.2 THE ORIGINAL ARRAY

The Buckland Park array of 1981 consisted of twelve Cerenkov detectors ( which are not discussed in this work ) and twelve 1 $m^2$ scintillation detectors. The total enclosed area of the array is $3\times10^4$ $m^2$. This array has been described in detail by Crouch et al. (1981) and a plan of it is shown in Figure 3.2. The 12 scintillation detectors performed particle density measurements with five of these also capable of timing measurements. Two of these five detectors were also the triggering detectors. These were detectors A ( which required >= 6 particles $m^{-2}$ ) and D ( which required >= 8 particles $m^{-2}$ ). The size spectrum produced by this array is shown in Figure 3.3. This is an integral spectrum where the intensity has been multiplied by (shower size)$^{1.5}$ to enhance the spectral features. ( This plotting technique for integral size spectra is analogous to the one shown in Figure 1.3 for the differential energy spectrum ). The size spectrum of the old array shows a slope change in the knee region, between $10^5$ and $10^6$ particles, corresponding to $\simeq$ $10^{15}$ to $10^{16}$ eV. There was a sensitivity cut-off below $\simeq$ 2 x $10^5$ particles which precluded more detailed study of the region below the knee. Consequently, there is only one point ( at $\simeq$ 3 x $10^5$ particles ) which shows the spectrum actually turning over. The rest of the points indicate a spectrum that is gradually increasing in slope, a feature which is not commonly observed. Extension of the lower limits of the

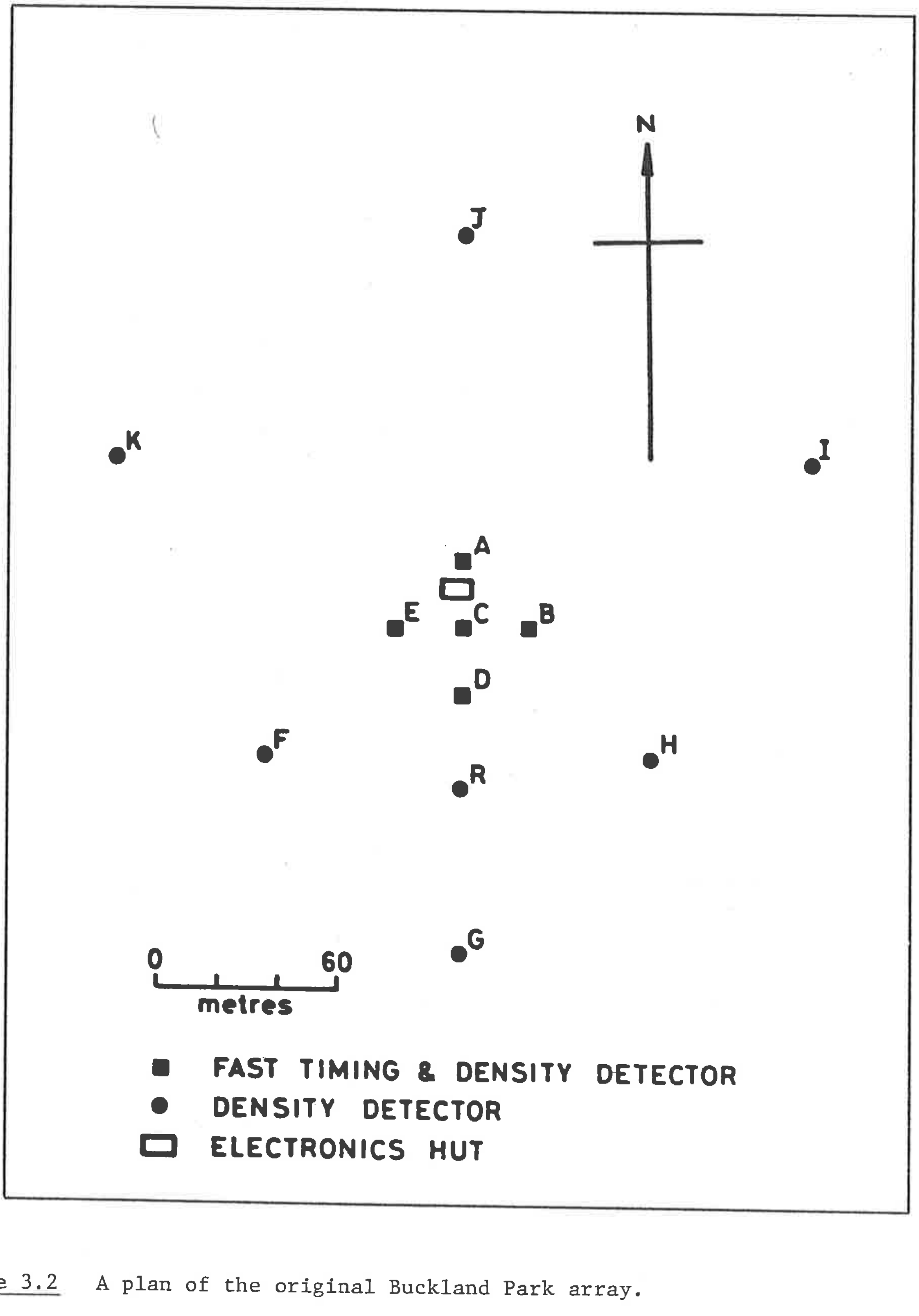

Figure 3.2 A plan of the original Buckland Park array.

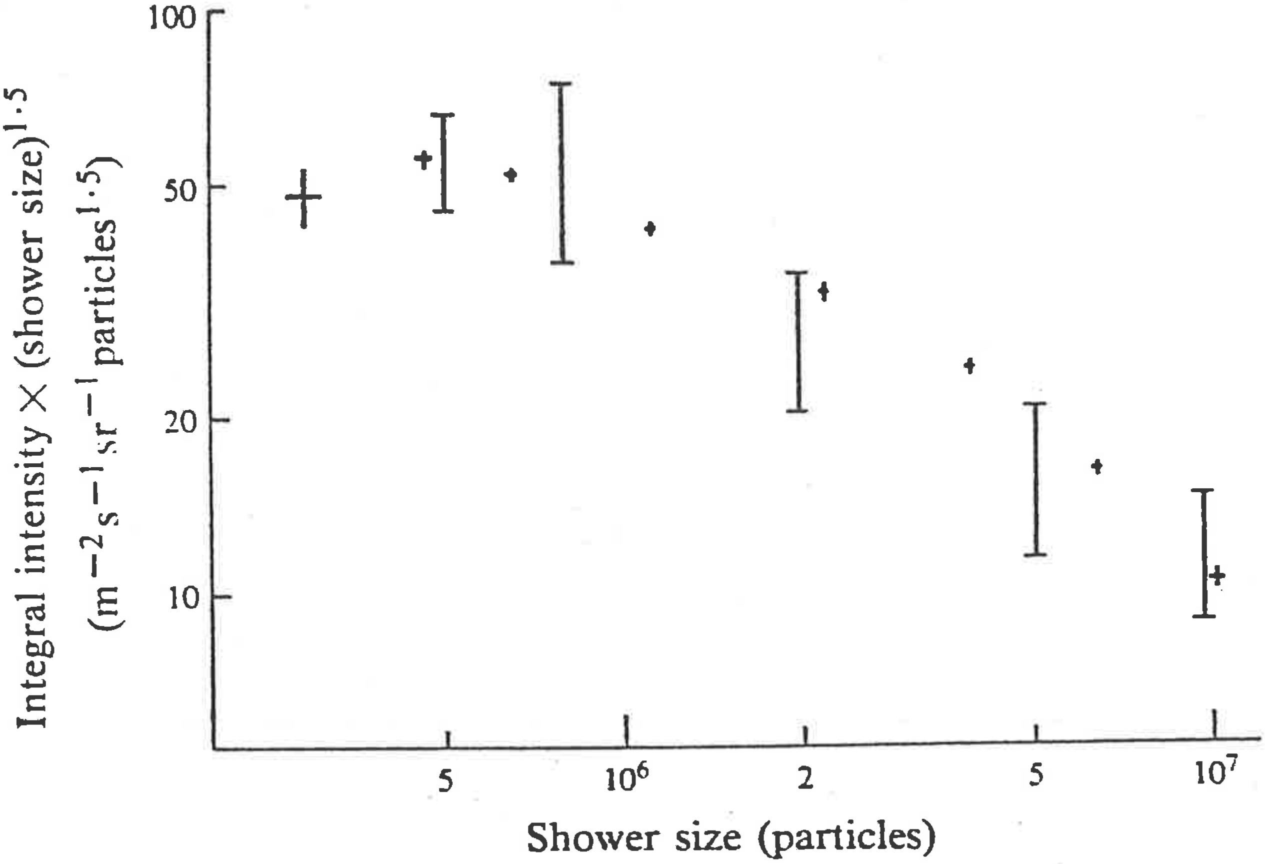

Figure 3.3 The sea level integral shower size spectrum of the original array derived for vertical showers. The crossed error bars are the Buckland Park data and the single error lines indicate the spread in a compilation by Hillas (1974) of such spectra. The intensity has been multiplied by (shower size)$^{1.5}$. (from Clay and Gerhardy 1982a)

array should enable further points below the knee to be added to this plot.

## 3.3 THE NEW ARRAY FOR SMALL SHOWERS

### 3.3 (a) Introduction

In 1983 extensions to the existing cosmic ray array were commenced to enable a more complete study of the knee region. The aim was to give the array the capability to analyse showers down to $\approx 2\times10^4$ particles at sea level by increasing the number of inner detectors. A central region of closely spaced detectors was created that was capable of effective analysis of small cosmic ray air showers.

The extended Buckland Park array is shown in Figure 3.4. The number of detectors was increased from 12 to 27 which included five new larger detectors near the centre of the array. All 27 detectors are capable of measuring particle densities, namely A1, B1, D1, E1, A through to N, and P to X (there is no O detector). Of these 27 detectors, 11 perform both timing and particle density measurements. These are A1, B1, D1, E1, A to E, S and T. Since this study was completed the timing array has undergone further improvements, resulting in 24 timing detectors. A table showing the co-ordinates of the 27 huts is given in Table 3.1.

The aim of the Buckland Park array is to correctly analyse the showers that impinge upon it. The required shower parameters to find are the direction, core co-ordinates, size and age. The direction is given by the zenith angle ( theta ) and the azimuth angle ( phi ) which indicate the origin of the shower in the sky. The core is the central point of the shower and the

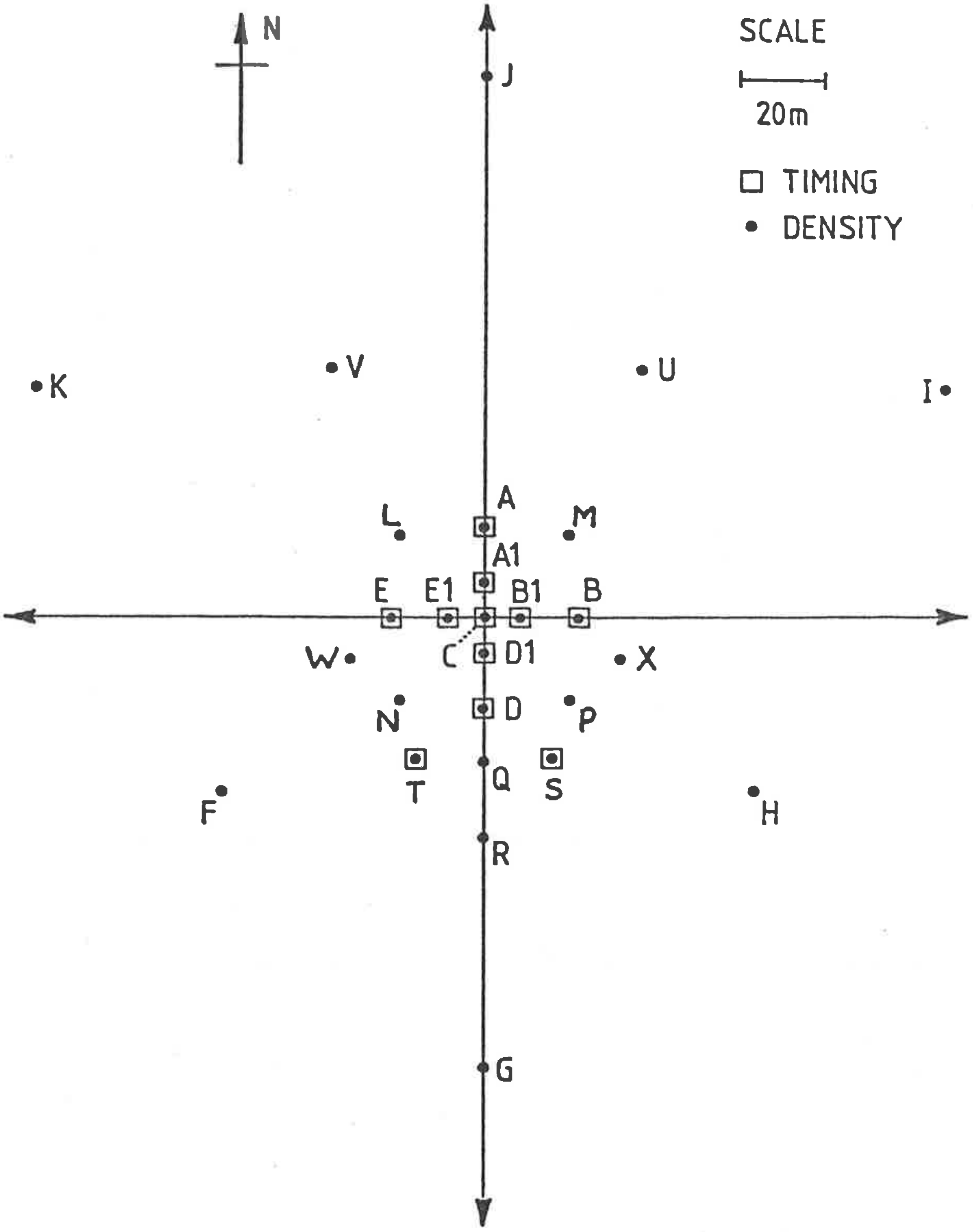

Figure 3.4 A plan of the extended Buckland Park array. The electronics hut is located between huts A and A1. The co-ordinates of the huts are given in Table 3.1.

# TABLE 3.1

| HUT | X CO-ORD (m) | Y CO-ORD (m) |
|---|---|---|
| A1 | 0.0 | 8.5 |
| B1 | 8.5 | 0.0 |
| D1 | 0.0 | -8.5 |
| E1 | -8.5 | 0.0 |
| A | 0.0 | 22.0 |
| B | 22.0 | 0.0 |
| C | 0.0 | 0.0 |
| D | 0.0 | -22.0 |
| E | -22.0 | 0.0 |
| F | -61.5 | -43.2 |
| G | 0.0 | -107.2 |
| H | 64.8 | -40.7 |
| I | 116.0 | 55.0 |
| J | 0.0 | 130.0 |
| K | -114.0 | 56.5 |
| L | -20.0 | 20.0 |
| M | 20.0 | 20.0 |
| N | -20.0 | -20.0 |
| P | 20.0 | -20.0 |
| Q | 0.0 | -34.6 |
| R | 0.0 | -53.0 |
| S | 16.0 | -34.0 |
| T | -16.0 | -34.0 |
| U | 37.6 | 59.6 |
| V | -35.1 | 60.0 |
| W | -31.3 | -9.6 |
| X | -32.0 | -9.8 |

size is the number of particles at sea level. Additionally a value for the age parameter, as explained in section 1.4 (e) (on the NKG function ) can be found for every event.

The chain of events from when a shower strikes the array to when the data has been recorded will now be considered. Initially the shower particles encounter the detectors. The information from these goes to the recording system, then is tested to see if the array has been "triggered", and if so is transferred to the array computer. This computer controls the array and records the raw data ready for calibration and further analysis. Sections 3.4 and 3.5 discuss the calibration and the data analysis to produce the final results. These procedures are performed on a VAX computer at the University of Adelaide.

### 3.3 (b) The Detectors

The essential design considerations of the detectors used at Buckland Park have been described by Clay and Gregory (1978). The 27 detectors are pyramidal in shape and are basically a slab of scintillator material viewed by a photomultiplier. An energetic particle ( such as an electron or muon ) traversing the scintillator will excite atoms in the material. The optical photons produced from de-excitation are detected by a photomultiplier placed at a distance from the slab of scintillator. As the shower front passes through the scintillator the particles induce a burst of photons and the pulse from the photomultiplier is approximately proportional to the number of traversing particles per unit area.

The detectors at Buckland Park house rectangular slabs of 50 mm thick NE102 ( or equivalent ) scintillator material. These slabs as well as the inside walls of the detector have been painted with white MgO reflector paint to improve light collection and uniformity. There are two types of detectors. Firstly, there are the "particle" detectors which measure particle numbers and contain particle ( or "slow" ) photomultipliers. The pulse heights from these tubes have small amplitude fluctuations for a given input. Secondly, there are the "particle and timing" detectors which perform timing measurements and particle counting. These house both timing ( or "fast" ) photomultipliers and slow photomultipliers. A diagram of a particle and timing detector is shown in Figure 3.5(a).

The fast tubes are Philips model XP2040 which have fast ( $\simeq$ 2ns ) and consistent rise times and produce narrow, accurately timed pulses. The slow tubes are RCA-8055 which produce pulse heights that are accurately proportional to the observed light. Five of the 11 particle and timing detectors are each 2.25 $m^2$ in area ( A1,B1,C,D1 and E1 ) and are designed to improve the particle counting statistics for small showers. The other six timing detectors ( as well as the remaining detectors in the array ) are 1 $m^2$ in area and have the superior timing resolution.

### 3.3 (c) The Response Uniformity of the Detectors

The larger particle and timing detectors, though useful for the extension of the lower shower size threshhold, posed response problems for the slow photomultipliers. The ideal requirement was to have uniformly responsive detectors, i.e. irrespective of where a particle traversed the detector (e.g. the centre as opposed to the edge ) the same output should be produced by the slow photomultiplier.

For the 2.25 $m^2$ detectors the minimum height from the base

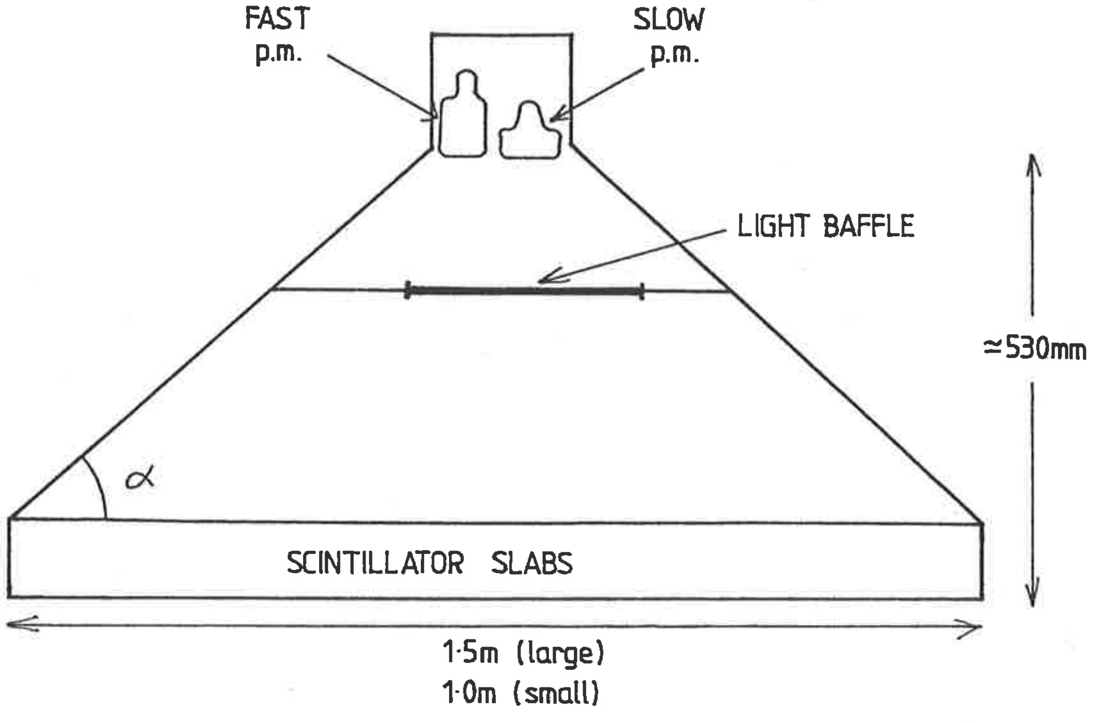

$\alpha$ = 38° for large detectors

$\alpha$ = 54° for small detectors

Figure 3.5(a) A cross-sectional view through a timing and particle detector. (The light baffles are only in the five large detectors).

to the apex of the pyramid would need to be 900mm to maintain acceptable uniformity of response. This height would have made the detectors unwieldy and expensive to house. The height chosen was 600 mm ( the same height as the 1m$^2$ detectors ) and it was decided to use a light baffle to improve the response. Such a procedure had been described by Clay and Gregory (1978). These authors concluded that the deterioration in uniformity as the distance between photomultiplier and scintillator decreased, was mainly due to the direct light from the scintillator to the photomultiplier. They stated that: "...a compact detector can be designed to have good uniformity if the direct light is blocked." Hence the purpose of the light baffle is to block the direct light from the region of the detector below the photomultiplier as the large signals from this region ( as compared to the small signals from the edges and corners ) cause the uniformity problems.

The tests for uniformity were made by examining the output pulse height spectra from the detector using a multi-channel analyser. This was gated with the output from a small 120mm diameter detector placed at various positions beneath the large detector. Single muon peaks were resolved both with and without the gating detector. As seen in Figure 3.5(a) the slow photomultiplier is offset from the apex of the pyramid and hence requires a similarly offset light baffle, or one that is asymmetrical in design. A solid square test baffle ( 38 x 38cm ) was made. When placed in the detector 30cm below the photomultiplier, in a symmetrical position, it was found to be unsatisfactory. Additions, each 10 cm wide, were added to two of the baffle sides to give the baffle the required asymmetry. However this was found to make the baffle too large as the intensity was reduced to a point where a gated single particle peak could not be resolved.

It was decided to modify the test baffle by punching a distribution of holes in the solid plate to gradually increase the light intensity seen by the photomultiplier outwards from the centre. Small holes were punched through the central region grading to larger holes at the perimeter of the baffle. A number of test baffles were required to find the optimal sizes and arrangement of the holes. A diagram of the final baffle is shown in Figure 3.5(b). This distribution was found to give a final uniformity of approximately ± 25% variation across the face of the scintillator. Figure 3.6 shows the results of the gating experiment with the single particle peak channel numbers ( indicating the intensity in a region ) shown for different regions over the detector face. These numbers should be compared with the average ungated single particle peak at channel 100, to show a variation of up to ± 25%. The original response showed a deviation from uniformity of about ± 50% . The improvement to ± 25% was considered adequate when compared to the Poisson fluctuations in the numbers of shower particles traversing the scintillator.

### 3.3 (d) The Recording System

The aim of the recording system is to record all details of showers that strike the array and then to select those showers which are suitable for a reliable and accurate analysis. To perform this task the recording system must receive the signals from the photomultipliers and initially find two sets of numbers. Firstly, the system must find how many particles were present in each detector. Secondly, it must find relative time

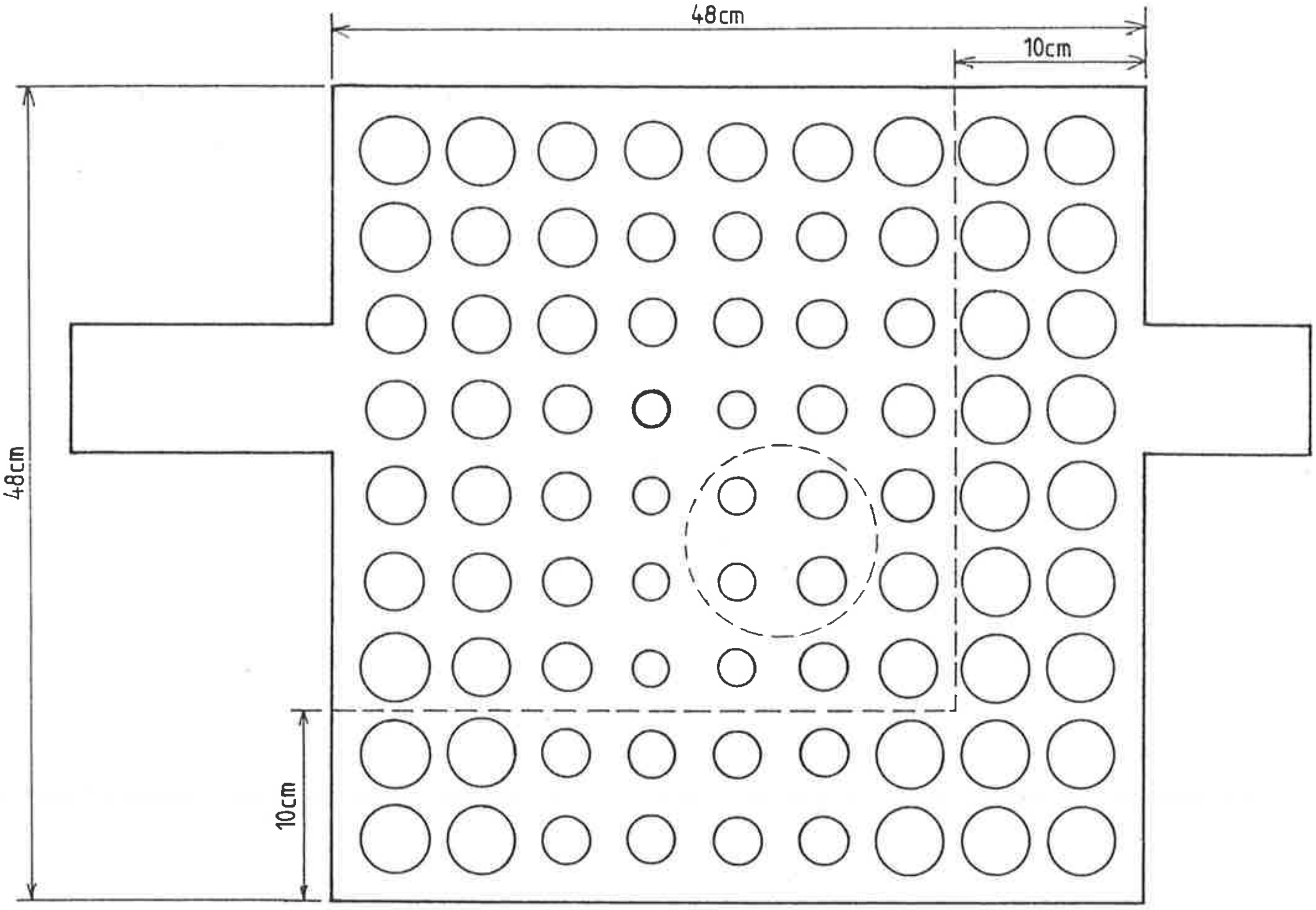

Figure 3.5(b) A plan view of a light baffle which are contained in the large detectors. They are made of galvanised mild steel, punched with holes, and painted with scintillator grade paint. The heavier outlined hole indicates the point directly below the centre of the detector. The dotted circle represents the projection of the particle p.m. onto the baffle and the dashed lines indicate the asymmetrical extension to the baffle. (see text)

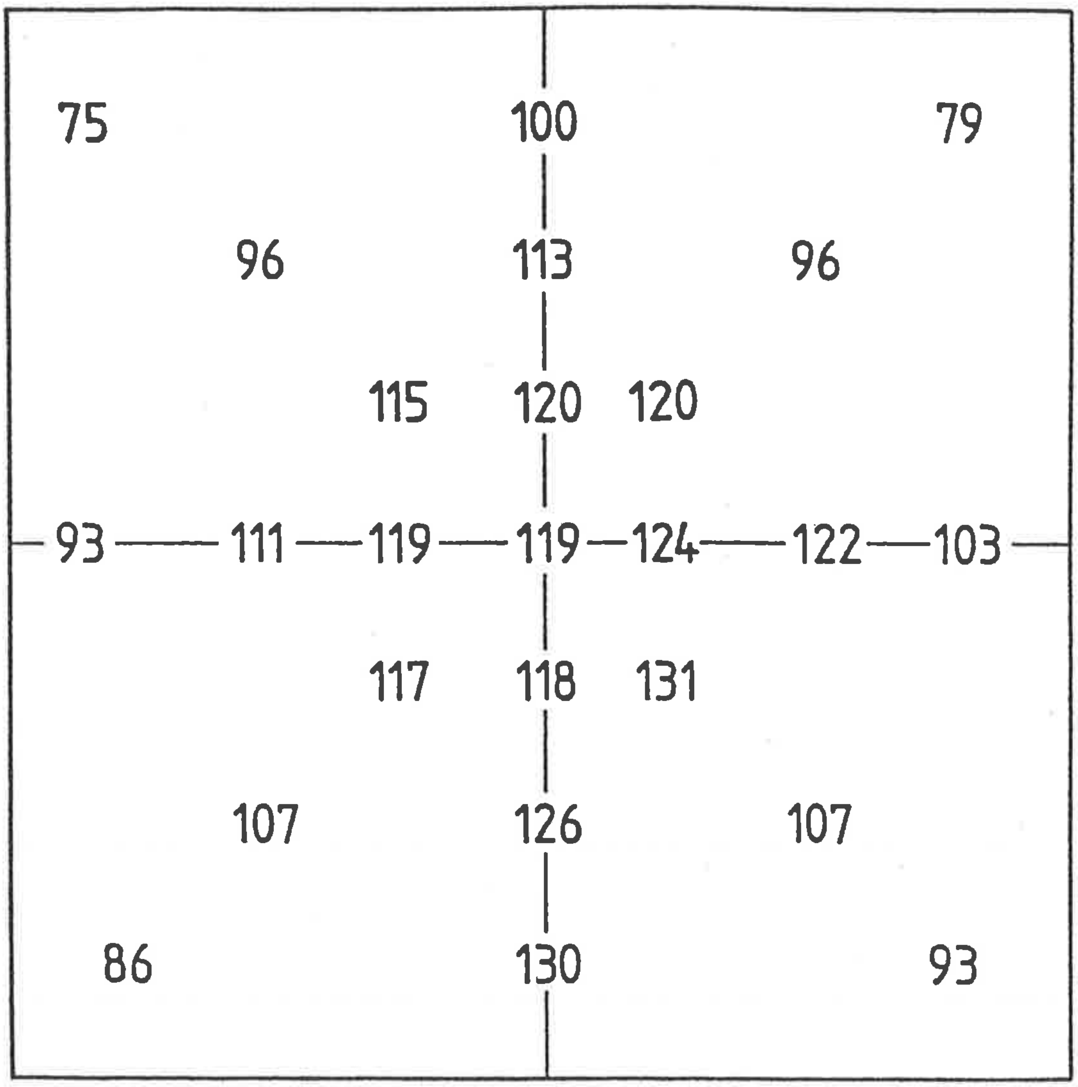

Figure 3.6 The uniformity response of a 2.25 $m^2$ detector. The values are the gated single particle peak channel numbers relative to the average ungated SPP channel number of 100.

values for each timing detector to indicate when the plane of the shower passed through that detector. As the shower plane is moving almost at the speed of light these time values must be precise to a few nanoseconds. This technique of finding a direction from a set of relative times is known as "fast timing."

The recording system is housed in a transportable ATCO hut, located between huts A1 and A. When an air shower passes through the array both the fast and slow photomultipliers may produce signals. For small showers only a few tubes may fire, whereas all 27 detectors can produce signals for the largest showers. The signals from the fast photomultipliers are transmitted directly to the recording hut along wide band RG 8A/U coaxial cable. The slow signals are put through a pre-amplifier and then transmitted via RG 58 cable.

The slow signals at the hut, in the form of positive voltage pulses, go to line receivers, attenuators and inverters. These devices shape and amplify the pulses into a form that is acceptable for the next stage. The signals are then fed separately to discriminators which ensure that the pulses are of sufficient magnitude. Simultaneously, the pulses are fed into the CAMAC ( Computer Automated Measurement And Control ) based recording system. This system consists of a "crate" which houses various modules as well as an interface to the Data General Nova 4S minicomputer which controls the experiment and handles the data. The slow system pulses go to peak sensing Analog to Digital Converters (ADC's - LeCroy 2259A) which digitize the pulse heights. The fast pulses goes to Time to Digital Converters (TDC's - LeCroy 2228A ). These TDC's start when triggered by a coincidence circuit for the timing huts where coincidence occurs if at least two of the 11 timing huts have fired. The TDC's measure relative times using stop pulses generated for each of the timing huts. Hence, the TDC's contain the timing information for each hut, while the ADC's contain the required information about particle numbers. If triggering conditions are met ( see next section ), the Nova receives "Look At Me" (LAM) pulses from the ADC and TDC modules and then records their contents.

### 3.3 (e) The Triggering System

The array must have a recording system that detects useful events and rejects signals from small or out-lying showers ( which may be impossible to analyse ), as well as rejecting spurious signals not associated with air showers. This is done by a "triggering" mechanism which involves both the slow and fast systems. However, due to the nature of the triggering requirements the array as a whole is essentially triggered by just the slow system.

To trigger the slow array at least two of the inner 19 slow detectors must have recorded a minimum number of particles as determined by the discriminator levels. Excluding the outer huts reduces the number of showers that are accepted which have cores lying outside the array. These levels are set so that this trigger is extremely unlikely to occur in the absence of an EAS. The slow system triggers at a rate of approximately 0.1Hz. The fast array also has triggering requirements: namely that at least two of the 11 timing detectors must fire. However this requirement is met much more frequently, at approximately 100Hz.

An "event" occurs when the array experiences both a fast and slow trigger in coincidence. The recording system then examines both the ADC and TDC contents. A fast array trigger alone will start the TDC's which then record the times for each hut. If there is no corresponding slow trigger these TDC values are not fed to the computer and are cleared with the next fast array trigger. The requirement of a fast and slow trigger in coincidence to trigger the whole array is employed as it ensures that there are always some times for directional analysis.

## 3.4 CALIBRATION OF THE RAW DATA

The information contained in the ADC and TDC modules is not directly useable. The ADC number is a digitised value representing a pulse height. This number contains information on the number of actual particles which have traversed the detector and this needs to be extracted from the raw ADC number. This process is known as "calibration". Similarly the raw TDC numbers, when considered relative to each other, contain information about the direction of the shower, but calculations are required to extract this information.

### 3.4 (a) Density Calibration

Primary particles from outer space strike the earth continuously, most of this flux being of very low energy nuclei. They produce very small showers at high altitudes which dissipate early, leaving only remnant energetic muons. By the time these muons reach sea level they are not associated with any air shower and constitute a general flux of single, omni-directional muons.

When the ungated pulse height spectrum from any one scintillator is examined with a multi-channel analyser (MCA), a peak is seen as shown in Figure 3.7. This peak ( or mode, i.e. most likely pulse height) is caused by the uncorrelated

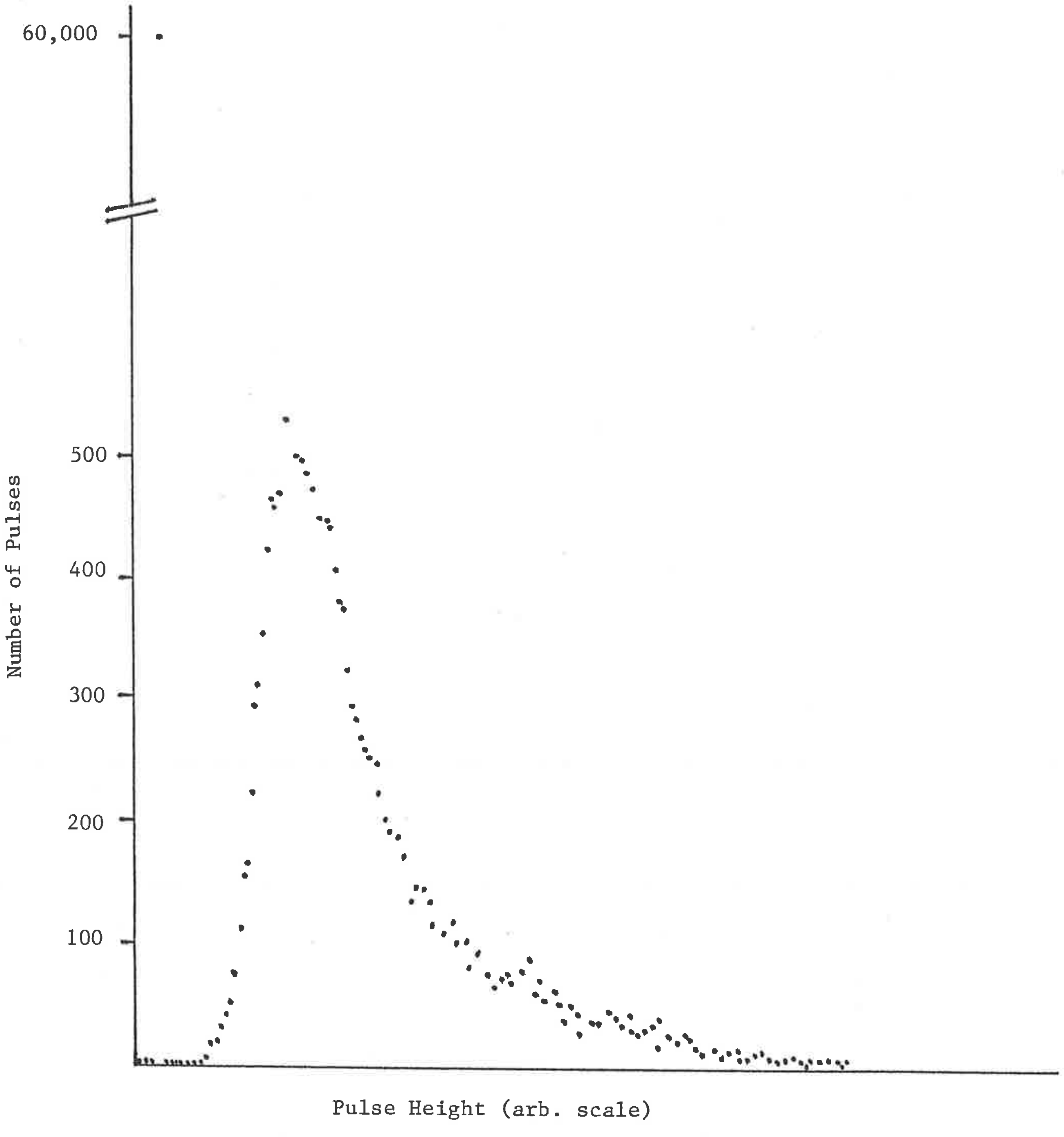

Fig 3.7 A sample pulse height spectrum, for the gated 50 mm thick detector.

omni-directional single muon flux and is known as a "single particle peak" (SPP). The distribution is of Landau form and is superimposed upon a low energy photomultiplier noise spike seen to the left of the main peak.

To perform the density calibrations the *mean* pulse height of the *vertical* single muon flux is required. To find this quantity the pulse height spectrum of the scintillator is examined. The SPP of the omni-directional single muon pulse height spectrum is a good approximation to the mean pulse height for the vertical single muon flux. This is due to the fortunate coincidence that the mean to mode ratio of any pulse height spectrum is 1.3, and that any pulse height observed for omni-directional muons is 1.3 times greater than that for vertical muons. Hence the pulse height of the peak observed in the omni-directional muon flux is used as the mean pulse height for an "equivalent single vertical muon".

To find the number of particles in any detector, the ratio is obtained of the voltage observed in that detector, to the voltage which would be produced by one particle (i.e. the voltage corresponding to the SPP). This was done using a tail pulse generator ( Berkeley Nucleonics Corp., model BH1) and a MCA ( an LRS 3001 or Tracor Northern 1705). The voltage observed in any detector was expressed in terms of an equivalent BNC voltage. That is, the ADC reading is converted to the voltage that the BNC pulse generator would require to produce that ADC reading. Similarly, an equivalent BNC voltage reading for the SPP is found. This gives the following:

$$\text{No. of particles} = \frac{\text{BNC value of density reading}}{\text{BNC value of SPP}}$$

Firstly, to obtain the BNC value of density, a series of inputs from the BNC pulse generator are fed into the ADC's and the outputs are then recorded. This allows a plot of "BNC" versus "ADC" to be produced. These plots are found for each ADC channel as there are slight variations between them. These relations are not quite linear, the best fits being power laws of the form:

$$\text{BNC value of density} = A \,.\, (\text{ADC value} - \text{Ped})^{B}$$

where Ped is the pedestal or "zero" value for each ADC,
and A and B are the fitted parameters.

Secondly, to obtain the BNC value of the SPP (i.e. BNC(SPP)) the relation between the MCA channel number and the BNC reading is obtained. The BNC pulses are fed to the MCA and a straight line relation is found of the form:

$$\text{MCA(channel number)} = \text{slope} \,.\, (\text{BNC value}) + \text{intercept}$$

Hence at the channel number corresponding to the SPP:

$$\text{MCA(SPP)} = \text{slope} \,.\, \text{BNC(SPP)} + \text{intercept}$$

$$\Rightarrow \quad \text{BNC(SPP)} = \frac{\text{MCA(SPP)} - \text{intercept}}{\text{slope}}$$

These two expressions are substituted into the expression for the number of particles, viz:

$$\text{No. of particles} = \frac{A \,.\, (\text{ADC} - \text{Ped})^{B} \,.\, \text{slope}}{\text{MCA(SPP)} - \text{intercept}}$$

For the case of the 1m$^2$ detectors these "number of particles" values are the actual particle densities. However, for the $2.25m^2$ detectors, the value for the number of particles must be divided by 2.25 to find the particle density.

The values A, B, slope, MCA(SPP) and intercept are all regularly checked as electronic drift can cause changes to these quantities. Additionally raw ADC values that are larger than 1000 are excluded ( i.e. their weight is set to zero ) as these are close to saturation. This corresponds to about 400 particles and such a value is very rare. For a detector to be saturated a shower of size $\approx 2 \times 10^6$ particles must land closer than 5 metres to that detector. The precision for each detector is governed by the particle to bit ratio and is $\approx$ 0.1 particles.

### 3.4 (b) Timing Calibration

The timing calibrations involve extracting the direction of the shower from the numbers stored in the TDC's. The shower direction is expressed using two angles, theta and phi. Theta is the zenith angle, whereas phi is the azimuth angle, and both are defined in Figure 3.8.

Due to the various delays from the huts to the recording station, the absolute values of the numbers in the TDC's have no meaning. It is only the differences between the numbers which are used to extract the direction. The delays are due to the cable lengths as well as electronic delays, and their sum total has not been accurately measured. Instead a more accurate technique is employed where the total delays are calculated with a computer program which analyses many events. In this technique the average time differences between all the huts are found (e.g. $\overline{A-C}$ , $\overline{B-D}$ etc ). These averages represent the time difference that would be observed for that pair of huts if a vertically directed shower were to fall on the array. This is

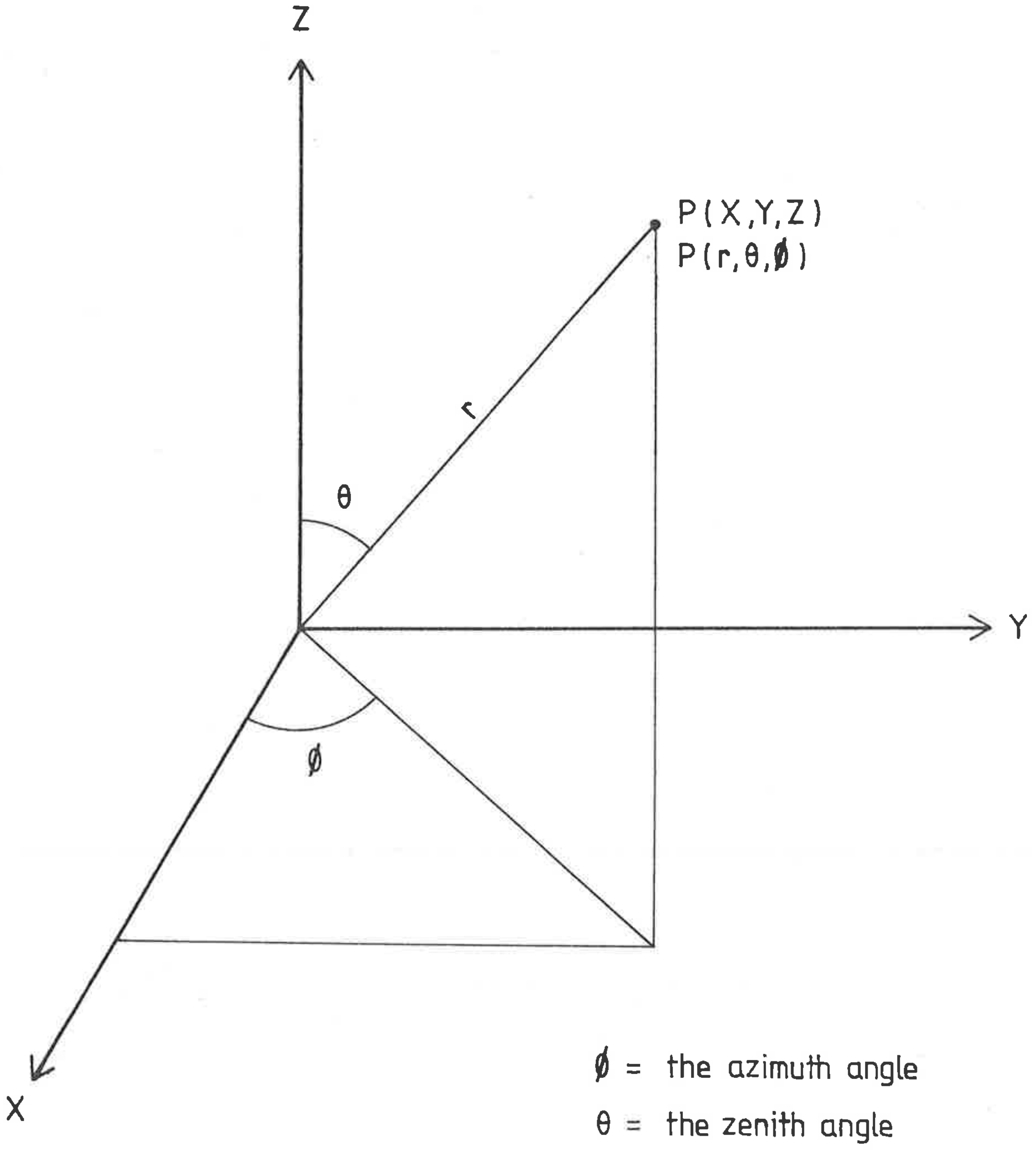

Figure 3.8 The definition of phi, the azimuth angle and theta, the zenith angle.

because showers come from all directions and when an average is taken over many events ( e.g 30,000 ) the average shower direction will be vertical. These average time differences are put into a large array ( 11x11, for 11 timing huts ) called DIFFS(11,11). Each element of DIFFS, $A_{i,j}$, represents the ith minus jth time difference, e.g $\overline{A-C}$ is element (1,3).

To use the elements of the DIFFS array each TDC number must initially be converted to a number of nanoseconds. This is performed using another set of calibration data which is also regularly checked in case of electronic drift. The calibration involves splitting a pulse from a generator and sending it directly to a TDC channel as well as through a known delay to the TDC channel. The direct pulse then starts the TDC and the delayed pulse stops it. For each TDC channel this produces a relation between the observed TDC number and the delay (in nanoseconds). Division of the TDC number by the slope of this relation converts it to a number in nanoseconds. The result is that, while the absolute value of the time in nanoseconds is not useful, the useful time differences will be in units of nanoseconds.

After the TDC numbers have been converted to nanoseconds, time differences between all huts are found. Subtracted from these time differences are the average time differences that are stored in the DIFFS array (e.g. $A-C - \overline{A-C}$ ). The result is a residual in nanoseconds which contains the directional information.

### 3.4 (c) Finding The Shower Direction

When a shower occurs a reference timing hut is chosen ( the "index" hut ). This is the hut with the largest number of particles and is given co-ordinates $(x_{in},y_{in})$. The axis of the shower can be expressed as a direction vector, as follows:

$$\bar{e} = -( l\bar{i} + m\bar{j} + n\bar{k} )$$

( the negative sign results from the convention which states that a negative direction vector points downward to the earth )

Here the $\bar{i}$, $\bar{j}$ and $\bar{k}$ vectors are unit vectors in the x, y and z directions, respectively. The $l, m$ and $n$ values are the direction cosines and each have a value between 0 and 1.

Additionally, the location of any hut $(x_i,y_i)$ with respect to the index hut $(x_{in},y_{in})$ is given by the vector:

$$\bar{r}_i = (x_i - x_{in})\,\bar{i} + (y_i - y_{in})\,\bar{j} + (z_i - z_{in})\,\bar{k}$$

The variations in the z-plane, $z_i - z_{in}$, are small and so can be ignored. Consequently, assuming a planar shower front we have:

$$\begin{aligned} \bar{e} \cdot \bar{r}_i &= \text{projection of } \bar{r}_i \text{ onto } \bar{e} \\ &= c\,(t_i - t_{in}) \end{aligned}$$

so that
$$\begin{aligned} c(t_i - t_{in}) &= -((x_i - x_{in})\bar{i} + (y_i - y_{in})\bar{j}) \cdot (l\bar{i} + m\bar{j}) \\ &= -((x_i - x_{in})l + (y_i - y_{in})m) \end{aligned}$$

The direction cosines $l$ and $m$ are found by minimising (with respect to $l$ and $m$) the least squares fit parameter (S):

$$\begin{aligned} S &= \sum_i ((ct_i - ct_{in}) - ( -l(x_i - x_{in}) - m(y_i - y_{in}))^2 \\ &= \sum_i ( c(t_i - t_{in}) + l(x_i - x_{in}) + m(y_i - y_{in}) )^2 \end{aligned}$$

The matrix algebra used to perform this minimisation can be found in Appendix 1, and the results are shown below:

$$l = -c\,\frac{\left( \sum_i y'^2_i \sum_i t'_i x'_i \; - \; \sum_i x'_i y'_i \sum_i t'_i y'_i \right)}{\left( \sum_i x'^2_i \sum_i y'^2_i \; - \; \left( \sum_i x'_i y'_i \right)^2 \right)}$$

$$m = -c\,\frac{\left( \sum_i x'^2_i \sum_i t'_i y'_i \; - \; \sum_i x'_i y'_i \sum_i t'_i x'_i \right)}{\left( \sum_i x'^2_i \sum_i y'^2_i \; - \; \left( \sum_i x'_i y'_i \right)^2 \right)}$$

where $x'_i = (x_i - x_{im})$,

$y'_i = (y_i - y_{im})$,

and $t'_i = (t_i - t_{im})$.

The value of $n$ can now be found from $l$ and $m$ as follows:

$$n = \left( 1 - l^2 - m^2 \right)^{1/2}$$

From the direction cosines, theta ($\Theta$) and phi ($\phi$) are found:

$$\Theta = \arccos(n)$$

$$\phi = 90 - \arctan(l/m)$$

The two approximations made in this analysis, namely a planar shower front and no z co-ordinate variation are both good approximations provided the shower cores do not fall in the out-lying regions of the array. The radius of curvature of a shower is of the order of a kilometre and the z variation is of the order of one metre ( $\simeq$ 3ns ).

The errors in phi and theta were conservatively estimated for the old array at 2.5 sec($\Theta$), that is, a 2.5° angular resolution for vertical showers ( Gerhardy 1983 ). A later examination of the angular response of this system ( Protheroe & Clay 1984 ) gave an angular resolution function with an angular uncertainty parameter of 1.25° for vertical showers. For the new array there are 11 timing detectors as opposed to five and, if all tubes trigger, then a further improvement to the angular resolution is envisaged by a factor of $(11/5)^{1/2}$ ( i.e. ≈ 1.5 ).

To test the quality of fit for the theta and phi values of each event, a statistical variable ( sigma - related to $\chi^2$ ) is calculated. Sigma contains the number of times in its denominator and hence is independent of the number of times used in the fit. Sigma is essentially the difference between the original recorded times and the times which have been calculated using the values of $l$, $m$ and $n$. Smaller values of sigma indicate better fits for theta and phi. Sigma squared is defined as follows:

$$(\sigma)^2 = \frac{\sum_i (t_{obs\,i} - t_{cal\,i})^2}{ntimes - 3}$$

where $t_{obs\,i}$ = observed time difference of one hut with respect to the reference hut $(x_{in}, y_{in})$,

where $t_{cal\,i} = \dfrac{-[\,l(x_i - x_{in}) + m(y_i - y_{in})\,]}{c}$

and ntimes is the total number of recorded times.

For any event from the old array data, a value of sigma of ≈ 6 indicted that the angular resolution for that event was of the order of 2°. A sigma of that magnitude for the new array would indicate a superior angular resolution and events having sigma > 10 ( of which there are comparitively few ) are now discarded.

## 3.5 ANALYSIS OF THE CALIBRATED DATA

The use of both the density calibration and timing calibration techniques described in section 3.4 comprises one part of the overall analysis of the raw data. After these processes have been performed, to produce values for phi, theta, sigma and the particle numbers, analysis of the shower parameters can commence. This analysis finds the core ($x_o$,$y_o$), the sea level size (Ne) for both Moscow and NKG lateral density distributions fits, and an age value (s) for the NKG fit.

### 3.5 (a) Data Handling

During most of the author's candidature the standard method of data handling involved the raw TDC and ADC outputs being written onto magnetic tape. These tapes were collected regularly from Buckland Park and taken to the University of Adelaide for analysis using a Cyber 173 computer.

Since the end of 1985 two major changes have been made to the data handling process. Firstly, the Nova computer at Buckland Park has been re-programmed so that a directional analysis is performed in "real time" as the events occur. The theta, phi and sigma values are then placed on tape along with the 27 raw ADC numbers. Secondly, the University has changed computers from the Cyber to a VAX 785 (along with the rest of the world). As a consequence, though a few changes to the analysis programs were required, essentially the same process is used to analyse the data. However as disc space is more limited on the VAX it may be necessary to change the analysis methods in the future.

The process of analysis of the raw ADC data is now discussed. Both the ADC and TDC data are transferred from the tapes to the computer and two main analysis programs are run. To perform the analysis the statistic chi-squared is used, as defined in the section below.

### 3.5 (b) Definition Of Chi-squared

In order to perform a shower analysis the value of the goodness of fit statistic, chi-squared ( $\chi^2$ ), is found. For this application, the statistic is a measure of the difference between the observed particle density values and the calculated density values. Hence if $\chi^2$ is minimised the best possible choices for the densities at each hut are found. This minimisation process is discussed further in section 3.5 (c).

For this work a "reduced" $\chi^2$ is used, this being the normal $\chi^2$ divided by the number of degrees of freedom. The number of degrees of freedom for a fit to a function with n coefficients plus one constant term is the number of data points minus the number of fitted parameters minus one ( Bevington 1969 ). The reduced $\chi^2$ is defined as follows:

$$\chi^2 (x_o, y_o, Ne) = \frac{\sum_i \frac{(\rho_{oi} - \rho_{ci})^2}{\rho_{oi}}}{ndf}$$

where $(x_o, y_o)$ are the co-ordinates of the core

Ne is the shower size

$\rho_{oi}$ are the observed densities

$\rho_{ci}$ are the calculated densities ndf is the number of degrees of freedom

(i.e. ndf = N − n − 1

where N = the number of detectors used
and n = the number of parameters being fitted (e.g. for NKG fit, where x, y and s are fitted, n = 3 ) )

### 3.5 (c) Data Analysis Programs

This work used two main programs for analysis:

DIRCALB − The direction and calibration program. This calculates phi, theta and sigma as described in sections 3.4 (b) and 3.4 (c). The program also performs the density calibrations (as discussed in section 3.4(a)) which gives the number of particles for each hut.

MINUIT − This is the James and Roos (1975) minimisation package produced at CERN. This program finds the necessary shower parameters by a reduced $\chi^2$ minimisation.

### 3.5 (c) (i) MINUIT

MINUIT is a powerful package designed to find the global minimum in a user-defined function, even if the function is very complex. It was purchased by the Cosmic Ray Group subsequent to difficulties encountered by the original gradient-search program, SHOWERS, which was used to analyse the array data with the Moscow-MIT function. SHOWERS had a failure rate of ≃ 3% when the program became trapped in local minima of chi-squared. MINUIT, which gives the user considerable choice in the minimisation method, improved this figure to about 1% for analysis of the old array data. MINUIT is also designed to fit up to 15 free parameters and hence the NKG function ( which has three parameters ) could to be solved and ages found for the events.

MINUIT gives the user three different minimisation options. These are a Monte Carlo search, the simplex method and the variable metric method. The Monte Carlo technique is not really applicable for $\chi^2$ minimisation as it does not converge to a minimum but finds the best value parameters by random choice. The other two methods were used in this work and can be invoked with one command: MINIMISE. This command first performs a simplex minimisation and then uses the variable metric method to further converge on the minimum ( James and Roos 1975 ). MINUIT also has numerous other available options. The ones used most often in this work are the IMPROVE command which will attempt to find a another minimum, the MINOS command which performs an error analysis, and the CONTOUR command which produces a plot of the contours of the minimised function.

To use MINUIT the subroutine FCN must be written by the user to define the function to be minimised. For the Buckland Park shower analysis the FCN initially reads in the phi, theta and sigma values as well as the 27 particle numbers ( converted to densities when required ). These particle numbers are then sorted and huts with zero particles are excluded from the analysis. The exclusion of zero densities is not necessarily an ideal technique but it was found for this work to give the best results. MINUIT takes several seconds to analyse an event, and therefore when up to 60,000 events per tape are analysed, this is very time consuming. As many of the showers which now trigger the array are small and only produce particles in a few detectors, one way of reducing the total analysis time is to remove huts with zero particles.

In addition to supplying the subroutine FCN, the user of MINUIT supplies a series of commands to the program. These are known as command "cards" and their role is to inform MINUIT of the variables involved in the fitting procedure, including their starting, limiting, and step-size values. These cards also inform MINUIT of the desired minimisation technique(s) and any other special requests.

In FCN the next step in the analysis is to define the function which MINUIT is to minimise. In this case the function is the reduced $\chi^2$ already given in section 3.5 (b) Values of this function are found for each possible core position (x,y) when the Moscow fitting function is used. Similarly, values of $\chi^2$ are found for each x,y and age when the NKG function is used. These fitting functions are used to find the values of the calculated densities, needed for $\chi^2$. As well as this a value for the shower size is needed. The shower size is not a fitted parameter as it is a dependent variable (and hence can be calculated from the other parameters). The technique for finding the shower size from the core, the density values, and age ( for NKG ) is shown in Appendix 2.

MINUIT, via the subroutine FCN, calculates the values of the expected densities at each hut for the starting values of x, y and age. It then calculates a shower size and finds a value of $\chi^2$. The minimising routines contained in MINUIT are then used as the program steps off by the chosen step size to find the direction in which $\chi^2$ is minimised. When $\chi^2$ is a minimum then the calculated densities are the best obtainable fit to the observed densities. Hence the corresponding values of $x_o$, $y_o$ and s ( and the Ne that is calculated from these ) are the best fit parameters for the shower.

### 3.5 (c) (ii) "QUIKFIT"

In this investigation the minimisation of the $\chi^2$ function by MINUIT is very time consuming. This is partly due to the complex $\chi^2$ surface but also results from the MINUIT package not being designed for repeated minimisations of the same function over many thousands of events. The most common use for MINUIT is the minimisation of a very complex function on a "one off" basis for which it is well suited.

One aim of this work was to find a way of overcoming the problem of time consuming analyses. Initially it was desired to produce a program which would find a direction and a "quick" core for each shower, i.e. an approximate location for the core to within 10 to 15 metres. Such a program was planned to operate in real time by the computer at Buckland Park. For this, the program QUIKFIT was written. However it was found that the Nova memory was almost full and there was insufficient room to store and run the program. Hence it has not been used for analysis up to the date of writing. Future plans for the array involve the acquisition of a another computer for use with the existing Nova and then the program QUIKFIT or its descendant can be used.

The section of the program which finds the shower direction uses the same techniques as those already described, as this method is time efficient. After the direction has been found a grid search technique is used to select the best possible core and size. At present this program has only been developed using a Moscow lateral distribution, as the aim was to search for a quick core. It may be possible to extend this program to cope with the NKG function, or alternatively a combination of the two programs QUIKFIT and MINUIT could be used. QUIKFIT could, in real time, produce an estimate of the core and MINUIT could then be used later with the NKG function to improve this core location and fit an age value to each shower.

The grid search technique is described below:

(1) Select the hut of highest density and call the co-ordinates ($x_m, y_m$).

(2) Make $x_m, y_m$ the centre of a square grid of certain size as determined by the location of $x_m, y_m$.

(3) If $x_m, y_m$, is:

(a) near the centre of the array ( i.e. less than 42 metres from (0,0) ) the lengths of the grid sides are defined as 42 metres.

(b) in the region between the central and out-lying regions of the array ( i.e. between 42 and 98 metres from (0,0) ) the grid sides are 56 metres in length.

(c) in the out-lying region of the array ( i.e. greater than 98 metres from (0,0) ) the lengths of the grid sides are 98 metres.

The numbers 42, 56 and 98 are variable and were chosen by experimentation.

(4) After the centre and length of the grid square have been chosen, the program examines a grid of points in the square. These points are separated by a set distance which can be varied. For each grid point a Moscow shower size, based on the core location and

density data, is calculated and then a value for $\chi^2$ is found. The best possible core is that which has the minimum $\chi^2$ value.

This method is only suitable as a rough estimate of the core position and given a variable point spacing of d, the approximate worst error for the core position ( excluding the effects of statistical fluctuations ) is given by d ( 0.5 )$^{1/2}$. The method has the advantage of being approximately 10 times faster than the use of MINUIT, taking ~ 0.3 s/event.

### 3.5 (c) (iii) ZXMWD

An alternative to MINUIT for the minimisation of $\chi^2$ is the package on the Vax IMSL library, namely ZXMWD. This package is designed to find the global minimum, with constraints, of a function with N variables. Hence it is similar in purpose to MINUIT but the mathematical methods it uses are not accesible to the public. In using ZXMWD the user supplies a subroutine FCN which calculates the function to be minimised. The user also supplies the constraints on the allowed parameter values and makes various requests on the manner of the search. As the package is more recent than MINUIT a logical conclusion would be that the package is superior. For this investigation, however, this was not the case as will be explained in the next chapter. Also, somewhat surprisingly, ZXMWD took about four times as long as MINUIT to find solutions.

The data analysis programs DIRCALB and MINUIT discussed here have been the two that have been mainly used in this work. The package MINUIT has been utilised with a number of analysis methods and results from all methods examined are presented in

Chapter Five, following a discussion of the simulation results and statistical considerations in Chapter Four.

# CHAPTER FOUR

# SIMULATIONS AND STATISTICAL CONSIDERATIONS

## 4.1 SIMULATED PERFORMANCE OF THE NEW ARRAY

### 4.1 (a) Introduction

The new array has been running since early 1985. However this has not been a smooth and continuous data collection due to power failures and adjustments to the detectors which have caused gaps in the data. Similarly, data analysis is yet to be performed on the bulk of the data as a final analysis method has not been chosen. The new VAX 785 computer at the University of Adelaide is suitable for all work involved in the analysis. However, the computer has many other users and it may be unable to handle the quantity of computing that will be necessary when the array is running at peak efficiency. Hence the use of the VAX computer for analysis could lead to a backlog of raw data and a computer which performs the analysis at Buckland Park in real time may be required.

Prior to the completion of the array, simulations were conducted to test its performance and examine possible selection biases. These simulations calculate the triggering probability of the array as a function of position, size and age. Hence the calculations of the 100% triggering contours, the relation of triggering area to shower size and the relation of triggering probability to age were performed.

### 4.1 (b) Contours of 100% Triggering

The purpose of this simulation is to gain an understanding of the performance of the array over its entire area with consideration to the shower size. For all shower sizes it is necessary to know whether a shower has landed in a region of the array which will always cause it to trigger.

To perform this simulation a computer program was written which simulated vertical showers landing at various core positions over the array. Both the Moscow function and the NKG function were used to simulate the particle lateral distributions. A value for the mean number of particles at each detector is found which is then fluctuated according to a Poisson distribution to simulate real fluctuations. These particle numbers are then compared with the triggering requirements of the array to test whether the simulated shower has triggered the array. This process is performed a number of times and a triggering percentage is found for all points considered across the array. As expected, it is found that small showers of size around $3 \times 10^4$ particles only consistently trigger in a small central region. As the size of the shower increases the size of the 100% triggering area also increases, as seen in Figure 4.1. ( Prescott et al. 1983 )

These triggering area calculations are useful in the design stages of an array. They are helpful in choosing the location of the detectors, and indicate whether the array is capable of accepting showers of the desired sizes. However, once the array is running, an analysis of the observed core locations in various size ranges must be performed. This produces the true 100% collecting areas for the array which are needed for accurate production of spectra. Additionally, these contours were

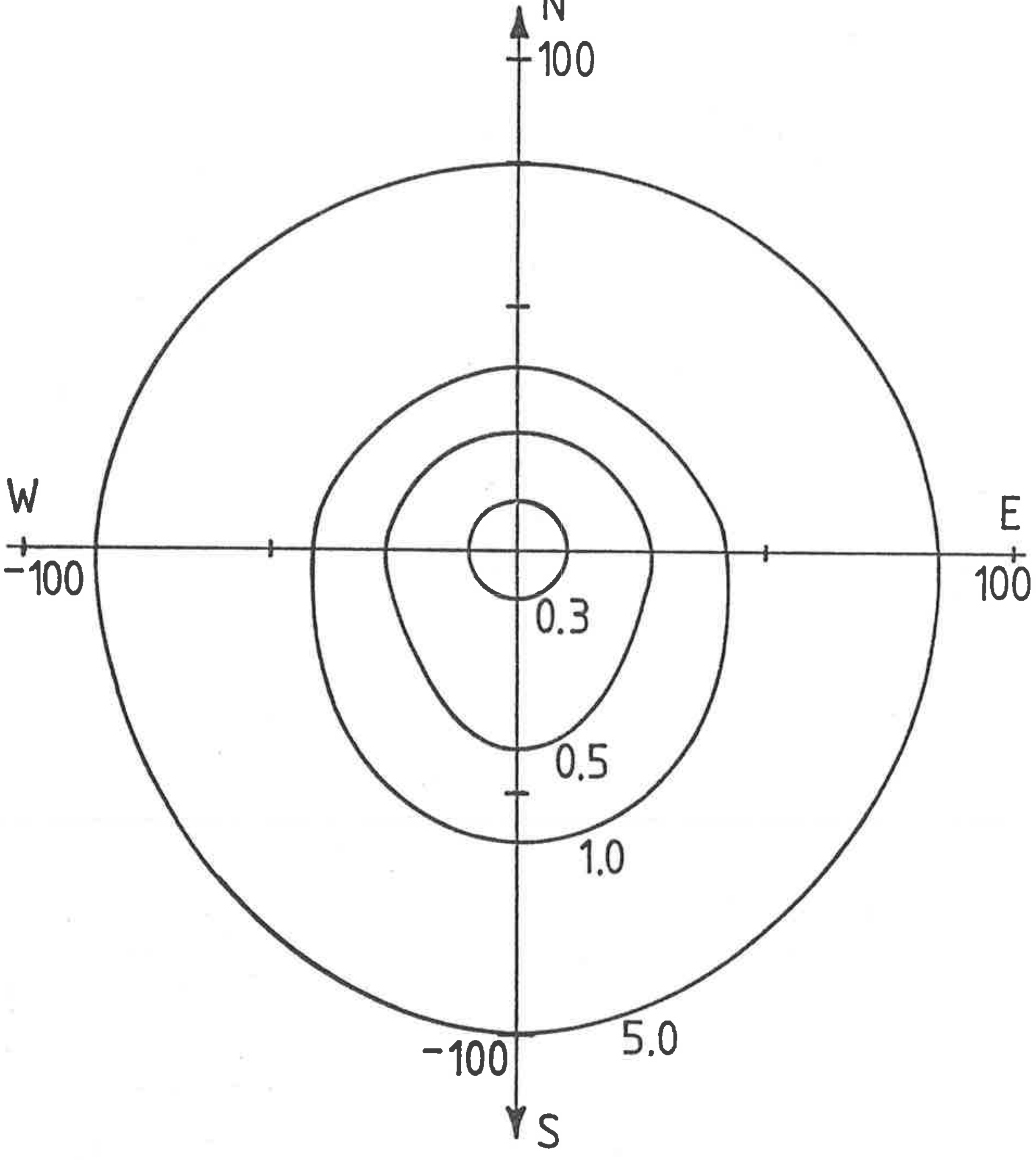

Figure 4.1 The contours of 100% triggering, from simulation. The lines represent sizes (x $10^5$) and the distances are in metres.

calculated based on the original triggering scheme which was slightly modified in the later stages of the array development. This has an effect on the 100% triggering contours and further simulations by future workers will be required to account for this.

### 4.1 (c) The Relation of Triggering Area to Shower Size

A further simulation for the array involved finding various relations between triggering area and shower size. A number of these curves are shown in Figure 4.2. These curves are found as an extension to the program described in the preceding section. After a 100% triggering area region has been found for a particular size range, the area of this region can be calculated. Similarly, the effective collection areas from the remainder of the array with less than 100% triggering can be evaluated and added to the original 100% triggering areas to produce a total triggering area. This is symbolised as $\iint P(x,y,N)\,dx\,dy$, where $P(x,y,N)$ is the triggering probability function. This is plotted against shower size for various triggering conditions.

In Figure 4.2 curves for both arrays can be seen with the relation for the old array on the right for its preferred triggering scheme ( namely densities in detectors A >= 6 particles $m^{-2}$ and D >= 8 particles $m^{-2}$ ). The three relations given for the new array show the effect of reducing the triggering thresholds for the array.

There is a definite improvement in the amount of triggering area for the smaller showers if the triggering detector thresholds are set at 4 particles per $m^2$ as compared with a threshold of 8 particles per $m^2$. Hence it seems that this should

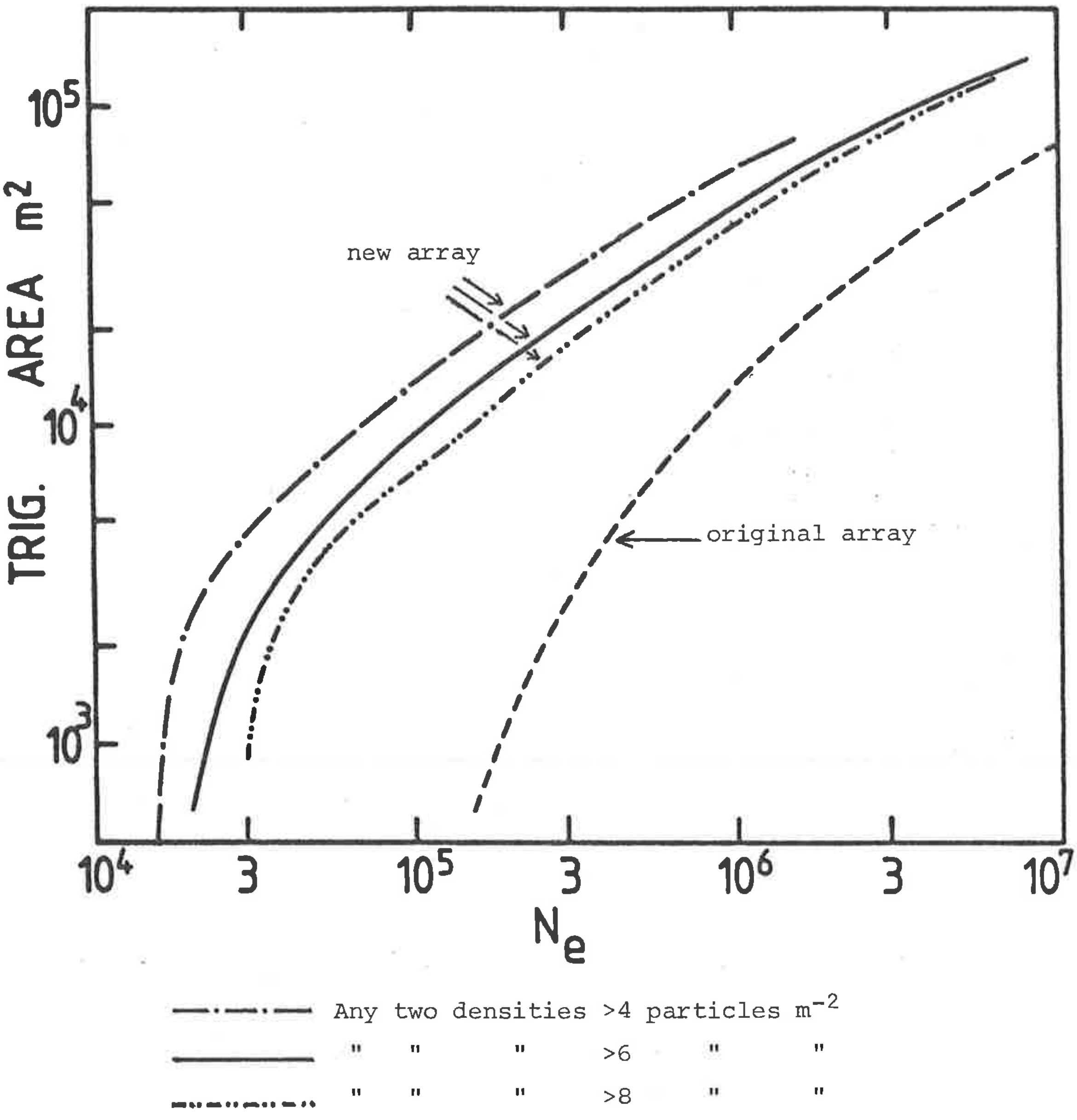

Figure 4.2 Triggering areas as a function of shower size, from simulation, for various triggering conditions.

be the choice for the triggering requirements. However what this relation does not show is that when the triggering level is reduced, while increasing the overall triggering area, the 100% triggering region decreases significantly. This is undesirable as the aim is to arrange the array so that there is a large plateau of 100% triggering probability that falls off rapidly to small probabilities at the plateau edges. The result is that the triggering thresholds cannot be set too low. Similarly they should not be set too high as, while this sharpens the 100% plateau, it also loses too many small events. It was found that a triggering detector threshold of 4 particles per $m^2$ was too low and 8 was unacceptably high. Hence the level of 6 particles per $m^2$ was chosen as the optimal value.

### 4.1 (d) The Relation of Triggering Probability to Age

A further simulation performed was an examination of the bias that inevitably occurs at the lower shower size limits of the array. The array is unable to detect small showers of large age, and the simulations of this trend are shown in Figure 4.3. Young showers ( i.e. $s < 1.0$ ) have a steep lateral distribution and the detectors near the core have high densities. As the shower size decreases there are normally still enough particles in the core detectors to ensure that the array triggers. However an older shower has a flatter lateral distribution and so the same total number of particles is spread over a larger area. This means that triggering the array becomes more difficult as there are fewer particles in individual detectors. Hence for small showers as the age increases the triggering probability for such showers decreases. This selection bias is unavoidable with the set triggering conditions and could only be removed with much

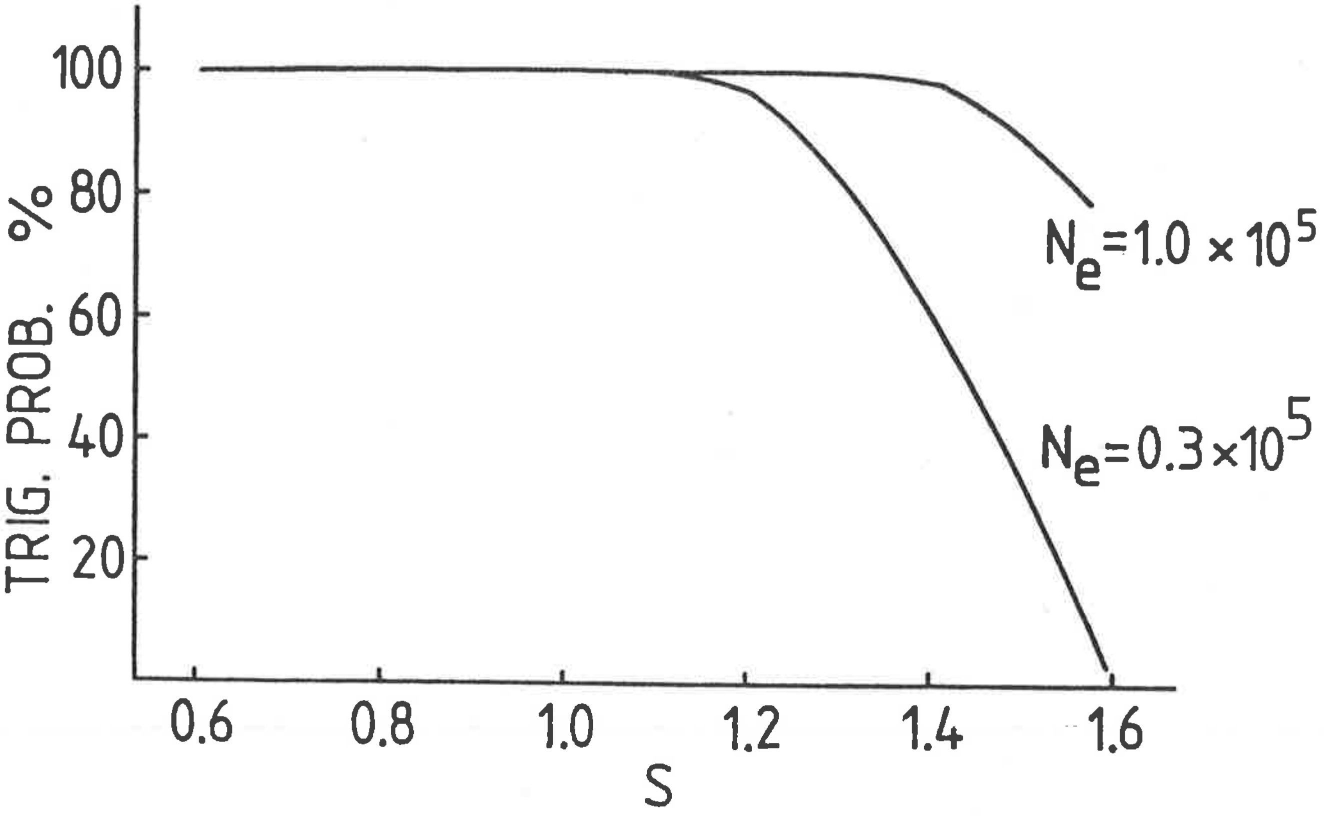

Figure 4.3 Array acceptance as a function of age for two values of shower size, from simulation.

lower triggering thresholds. However this introduces the effects discussed in the previous section as well as merely shifting the bias down to lower sizes.

### 4.1 (e) MINUIT Simulation

A further simulation as a check on the minimisation program MINUIT was also performed. This involved the simulation of some showers with a given core, size and age. These parameters were substituted into the NKG function to find the densities that would be produced at hut locations. These density values were then fluctuated according to Poisson statistics and MINUIT was used to find the shower parameters. Initially, when no fluctuations were considered and when the standard form of $\chi^2$ was used ( see the next section ), the program found the shower parameters very effectively, finding ( at worst ) the core to within 0.4 of a metre, the size to within 4% and the age to within 0.07.

When the Poisson fluctuations were applied an increase in $\chi^2$ was observed and ( at worst ) the core was found to within 2 metres, the size to within 18% and the age to within 0.15. The contours of $\chi^2$ of these fits were examined and the troughs had a circular symmetry and hence it was considered that the fitting procedure was working acceptably.

## 4.2 STATISTICAL CONSIDERATIONS

### 4.2 (a) Chi-squared

The definition of $\chi^2$ as used in this study has been given in Section 3.5 (b). This statistic has been the main one used for the analyses. A descriptive form of the $\chi^2$ test statistic is as follows:

$$\text{Sum} \; \frac{(\text{observed} - \text{theoretical frequency})^2}{\text{theoretical frequency}}$$

The properties of this sum were first studied by Pearson in 1900. He calculated its distribution for different samples and found that it approximated a $\chi^2$ distribution ( a well known normal related distribution which is a special case of the Gamma distribution ). Hence the name used for the goodness of fit test based on this statistic has become known as a $\chi^2$ test.

In general the formulation of the goodness of fit test, $\chi^2$, is:

$$\chi^2 = \sum_i \left[ \frac{[y_i - y(x_i)]^2}{\sigma_i^2} \right]$$

where $y_i$'s are the observed data points,

$y(x_i)$'s are the estimated values,

and $\sigma_i$'s are the standard deviations on the individual observed data points.

The denominator of the expression contains the standard deviations which must be found. Hence the spread of the original parent population distribution from which the observations are made must be found. As the number of particles measured in a detector follow a Poisson distribution this allows the well known statistical features of this distribution to be utilised.

If an infinite number of observations of the same event were taken it would be seen that the observations were spread according to a Poisson distribution and a mean value for the number of particles in that detector ($\mu$) could be found. Then the standard deviation of the Poisson distributon is equal to the square root of that mean.

$$\text{i.e.} \qquad \sigma = (\mu)^{1/2}$$

However, rather than an infinite number of observations of the number of particles in a detector per event, this value is observed once only. This means that the value could, in theory, fall anywhere fron 0 to infinity. However Poisson distributions for high particle numbers approach a normal distribution where the most probable value is equal to the mean. As the particle number decreases, this approximation becomes less valid but for most cases it is still reasonable. Hence the values of the standard deviations for each individual measurement can be estimated by:

$$\sigma_i = (y_i)^{1/2}$$

There is another approach to the determination of the standard deviation of the parent Poisson distribution based on the ideas presented above. Allowing that the value of the square root of the *observed* density can be used as an estimate of the standard deviation, then it is plausible to consider that the value of the *calculated* ( or predicted ) density can also be used. This follows as the calculated value should be close to the observed value for a good fit. Additionally in the evaluation of the calculated density at any hut, the values of the densities at the other huts have been considered. This means that the value of the calculated density could be a closer approximation to the true mean of the parent Poisson distribution. This method can also be useful when considering observed densities of zero. The calculated density values at these points are unlikely to be exactly zero and so the above expression is less likely to go to infinity.

The two possible forms of $\chi^2$ are given below:

$$\chi^2 = \sum_{i=1}^{N} \left( \frac{1}{y(x_i)} [y_i - y(x_i)]^2 \right) \qquad \text{..... Form A}$$

This has been termed the "standard" or usual "minimum $\chi^2$ method" ( e.g. Eadie et al. 1971 )

$$\chi^2 = \sum_{i=1}^{N} \left( \frac{1}{y_i} [y_i - y(x_i)]^2 \right) \qquad \text{..... Form B}$$

Eadie et al. term this form as the "modified minimum $\chi^2$ method". However Awaya (1979) describes this as the usual form for counting experiments which follow the Poisson distribution.

In fact there is no general agreement as to which is the appropriate form of the standard deviation to be used in the case of counting experiments such as this one. Awaya (1979) points outs that for his experiment, where pulse height spectra are fitted, neither of these alternatives give the best answer. He finds that when Form B is used the values for $y(x_i)$ are consistently under-estimated leading to the area under the fitting function being too little by a value equal to the minimum value of $\chi^2$. Similarly when Awaya uses Form A he finds that the values are over-estimated with the result that the area under the fitting function is too large by a factor of half the minimum value of $\chi^2$.

For the Buckland Park analysis it was found that the superior fits to the data were not obtained from either Form A or

B. By a process best described as educated guesswork the most reliable fits were found to come from a "hybrid" version of the two. This is given below:

$$\chi^2 = \sum_{i}^{N} \left[ \frac{(y_i - y(x_i))^2}{(y_i . y(x_i))^{1/2}} \right]$$

As can be seen the denominator contains the geometric mean of the two possible values of standard deviation, namely the observed and the calculated values for the density.

Also relevant to this work are the values of the frequencies in the data bins. Basic texts on statistics (e.g. Ehrenberg 1975) state that the theoretical frequency in any one grouping interval should be equal to or greater than five. If this condition is not satisfied then the use of $\chi^2$ as a goodness of fit test is somewhat doubtful. For the analysis of array data it is quite common that huts have less than five particles in them and so, theoretically, these huts should be excluded from the analysis. However if they are excluded the resultant fits are worse, rather than better. Hence, while it is possible that this is the cause of the analysis problems, it is by no means definite.

One attempt to overcome the problem of $\chi^2$ not being applicable for low frequencies was to change the whole technique of solution. The technique of maximum likelihood can be used in instances of low frequencies and so it was applied to the air shower data. This method allows for a more correct treatment of density fluctuations when the particle densities are small and the asymmetry of the Poisson distribution becomes important. This work was performed by a vacation scholar, David Bird. Awaya (1979) found this method gave improved answers for his pulse height spectra as opposed to the use of $\chi^2$. A further discussion on the comparison between the minimum $\chi^2$ method or the maximum likelihood method is given in Lai and MacKeown (1981).

### 4.2 (b) Maximum Likelihood

An alternative method for finding the best solution for the shower parameters is to use the method of maximum likelihood. This method makes use of the sample likelihood function which is a function of the unknown parameters. The maximum likelihood estimator of the parameters is the value of those parameters which causes the likelihood function to be a maximum. As the densities increase the maximum likelihood method approaches the $\chi^2$ method.

The following discussion is derived from Benjamin and Cornell (1970). In general terms where there are r parameters in vector form, $\boldsymbol{\theta} = \{\theta_1,\theta_2,\ldots,\theta_r\}$, then to use the method of maximum likelihood, estimators of those parameters are chosen, $\bar{\boldsymbol{\theta}} = \{\bar{\theta}_1,\bar{\theta}_2,\ldots,\bar{\theta}_r\}$. These estimators are used to maximise the likelihood, L:

$$L(\boldsymbol{\theta} \mid x_1,x_2,\ldots,x_n) = \prod_{i=1}^{n} f(x_i \mid \boldsymbol{\theta})$$

or equivalently, the log likelihood (as is appropriate for this work ):

$$\log\ (L(\boldsymbol{\theta}|x_1,x_2,\ldots,x_n)) = \log\ (\prod_{i=1}^{n} f(x_i|\boldsymbol{\theta})) = \sum_{i=1}^{n} \log\ (f(x_i|\boldsymbol{\theta})).$$

When these general equations are applied to the reduction of air shower data with the particle densities fluctuated with Poisson statistics, then the function to be maximised is the probability function. The probability of observing y events in a given time interval (where $\mu$ is the mean of the distribution) is given by:

$$P = \frac{\mu^{y}}{y!} e^{-\mu}$$

Using the same arguments as before, the value for the mean of the distribution can be replaced in this function. Hence if y(x) is the fitting function and the means for each data bin are $\mu_i = y(x_i)$, then the complete function to be maximised is as follows:

$$P = \prod_{i=1}^{n} \{ \frac{(y(x_i))^{y_i}}{y_i!} e^{-y(x_i)} \}$$

The simplest way to solve this problem is to use logarithms. The logarithm of the probability is maximised, as follows, where the notation has been changed to suit this actual problem. The $y_i$'s have been replaced with observed densities, $\rho_{oi}$, and the $y(x_i)$'s have been replaced with the calculated densities, $\rho_{ci}$.

$$\ln P = \sum_{i=1}^{n} ( \rho_{oi} \ln \rho_{ci} ) - \sum_{i=1}^{n} ( \rho_{ci} - \log \rho_{oi}! )$$

The value for $\log \rho_{oi}!$ can be found analytically or Stirling's approximation for large values of $\rho_{oi}$ can be used. The method of maximum likelihood should be suited to the solution of shower data and has been successfully used by other workers ( e.g. Sun Louri and Winn 1984 ). However, a substitution for the value of the standard deviation for a Poisson distribution is still required and so the method has not solved this difficulty. In this case it was still found to produce imperfect results.

# CHAPTER FIVE

# RESULTS

## 5.1 INTRODUCTION

Even though final results have yet to be found from the array a considerable amount of work has been done and will be presented. Both the theta and phi distributions of the array have been found and are acceptable. Using the best available method of analysis, a differential rate spectrum has been produced. In addition other methods of analysis were studied. The age distribution for various size bins have been examined and compared with other results.

At the time of writing further improvements had been made to the directional abilities of the array by the addition of more timing detectors. Also a superior timing analysis program was written which removed some of the approximations made in this and previous work to improve the angular resolution, ( Ciampa and Clay 1986 ). The present situation involving the core and size analysis for the array is that there are still some unknown systematic effects which are affecting the results. However, it appears that while cores are not being accurately located, the core errors are not excessively large ( generally less than 15 m) if the "hybrid" version of $\chi^2$ is used (to be further explained ). The fitted shower sizes are not critically dependent on the core locations and hence these sizes may still be close to the true sizes. When the hybrid version of $X^2$ is used and individual events are examined, most particle density values at the detectors are normally well fitted, especially huts with high densities; the huts with low densities being more poorly fitted.

The result of this method ( as well as others ) is that shower cores are artificially forced to land on hut locations. This problem is seen when attempts are made to find the actual triggering areas for various size ranges. To do this the overall distribution of cores is examined and the "hut-seeking" tendency is then observed. The results of this work are discussed in section 5.4.

## 5.2 THE ZENITH ANGLE DISTRIBUTION

An examination of the zenith angle (theta) distribution of the array is important as it enables a check to be made on the directional analysis that is being made. This is because the theta distribution depends on two simple functions. The first is that as theta increases, the solid angle subtended by an element of theta, $\Delta\Theta$, increases as $2\pi\sin\Theta\,\Delta\Theta$. Hence the number of showers originating from a theta range increases as theta increases. Secondly, and in opposition to the first effect, as theta increases, the attenuation from the atmosphere also increases resulting in less showers reaching ground level from larger thetas. Consequently there is a peak in the theta distribution. The approximate value of this peak can be found from the following brief analysis.

The solid angle ( $\Omega$ ) variation with theta is as follows:

$$\frac{d\Omega}{d\Theta} = 2\pi\sin\Theta$$

The atmospheric attenuation effect seen by the array must now be considered. The zenith angle distribution from this effect has been examined previously by Ashton et al. (1979b). Their results show that there is a zenith angle variation approximately proportional to $\cos^8\theta$ in the size range $5 \times 10^4$ to $1.4 \times 10^6$ particles, as also used by Protheroe and Clay (1984). Hence the variation of array efficiency ( $\varepsilon$ ) with zenith angle, can be expressed as follows:

$$\varepsilon \propto \cos^8\theta$$

For sizes less than $5 \times 10^5$ particles, the value of the exponent is less ( Ashton et al. (1979b) find a value of $\simeq 5$ ) but its exact value is not critical to this result. The $\cos^8\theta$ dependency is multiplied by the $d\Omega/d\theta$ expression to obtain a function, F, which describes both the solid angle and the atmospheric attenuation effects, that is:

$$F = \text{constant} \; ( 2 \pi \sin\theta \cos^8\theta \, d\theta).$$

This function is then solved for the most probable theta,

$$\text{i.e.} \qquad \frac{d}{d\theta} \, 2 \pi \sin\theta \cos^8\theta = 0$$

$$\Rightarrow \qquad \cos\theta \cos^8\theta - 8 \cos^7\theta \sin\theta \sin\theta = 0$$

$$\Rightarrow \qquad \tan^2 \theta = 1/8$$

$$\Rightarrow \qquad \theta = 19.5^\circ$$

A theta distribution for the array is shown in Figure 5.1. The most probable theta observed by the array is $\simeq 20^\circ$ and this is in agreement with the calculations above. The average theta is slightly greater at $22.5^\circ$ due to the effect of the tail of the

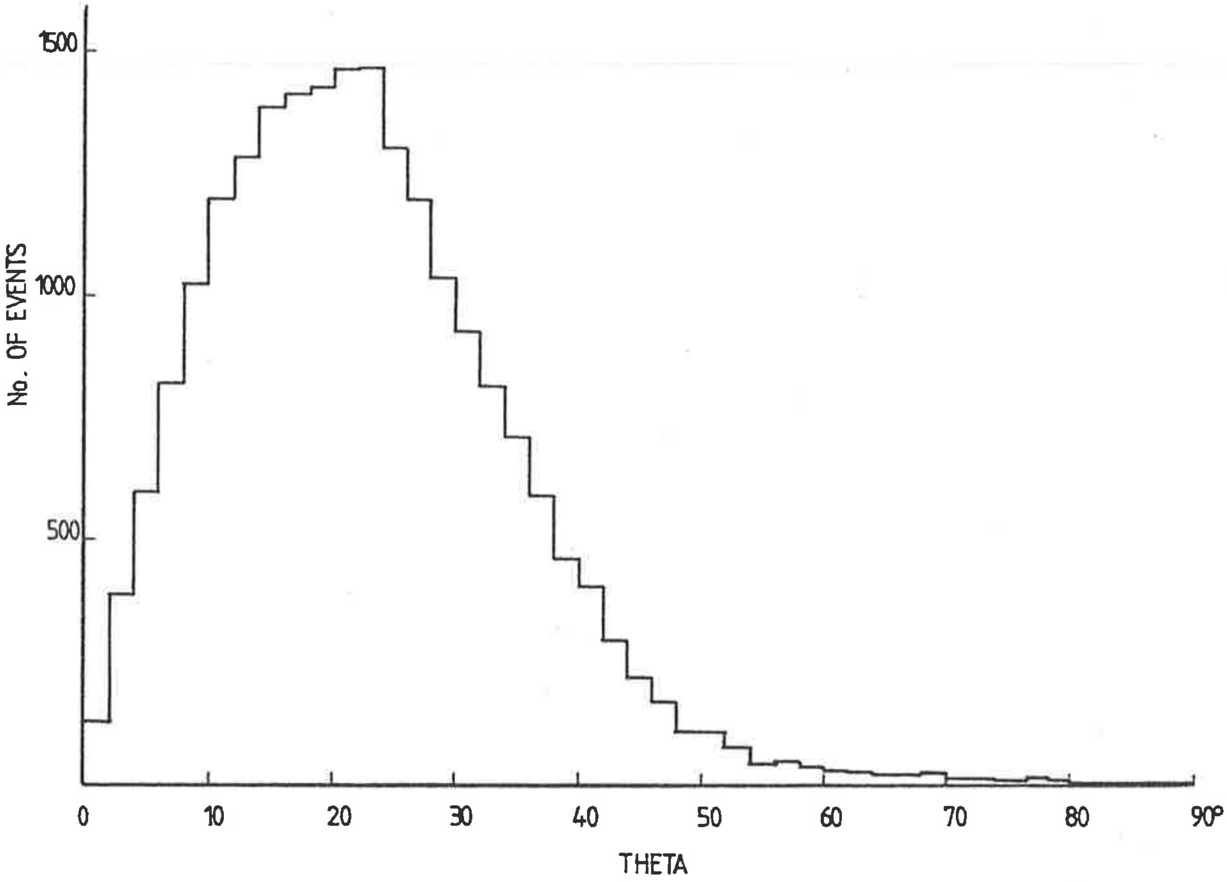

Figure 5.1 The theta distribution of the array from ≃ 23,000 events. The mean theta is 22.5°.

theta distribution.

## 5.3 THE AZIMUTHAL ANGLE DISTRIBUTION

The azimuth angle (phi) distribution is shown in Figure 5.2. This distribution should be uniform except for statistical fluctuations as the array is essentially symmetrical and should observe showers arriving uniformly from all azimuthal directions. It can be seen that the azimuthal distribution of the array is relatively flat as expected.

In the past, with fewer array detectors, there have been variations to this uniform phi distribution due to projection effects. Gerhardy (1983) notes the Buckland Park array as having an azimuthal angle distribution modulated by a large second harmonic. This is explained by the two main triggering detectors, A and D, having a reduced separation to inclined showers from northern or southern directions, as compared to western or eastern. For the array at present, the different triggering conditions ( namely any two of the inner 19 detectors firing) remove this asymmetry of triggering and any small modulation effect is now due to the asymmetrical arrangement of the detectors.

## 5.4 CORE LOCATIONS AND SHOWER SIZE DETERMINATIONS

The basic principles for finding the core and size of a shower were discussed in Chapter Three. Also some of the statistical methods used in this work have been described in section 4.2. In addition to these methods, a number of other alternatives have been tried. All methods of analysis will now be discussed with their results.

The core location results are displayed in the form of core

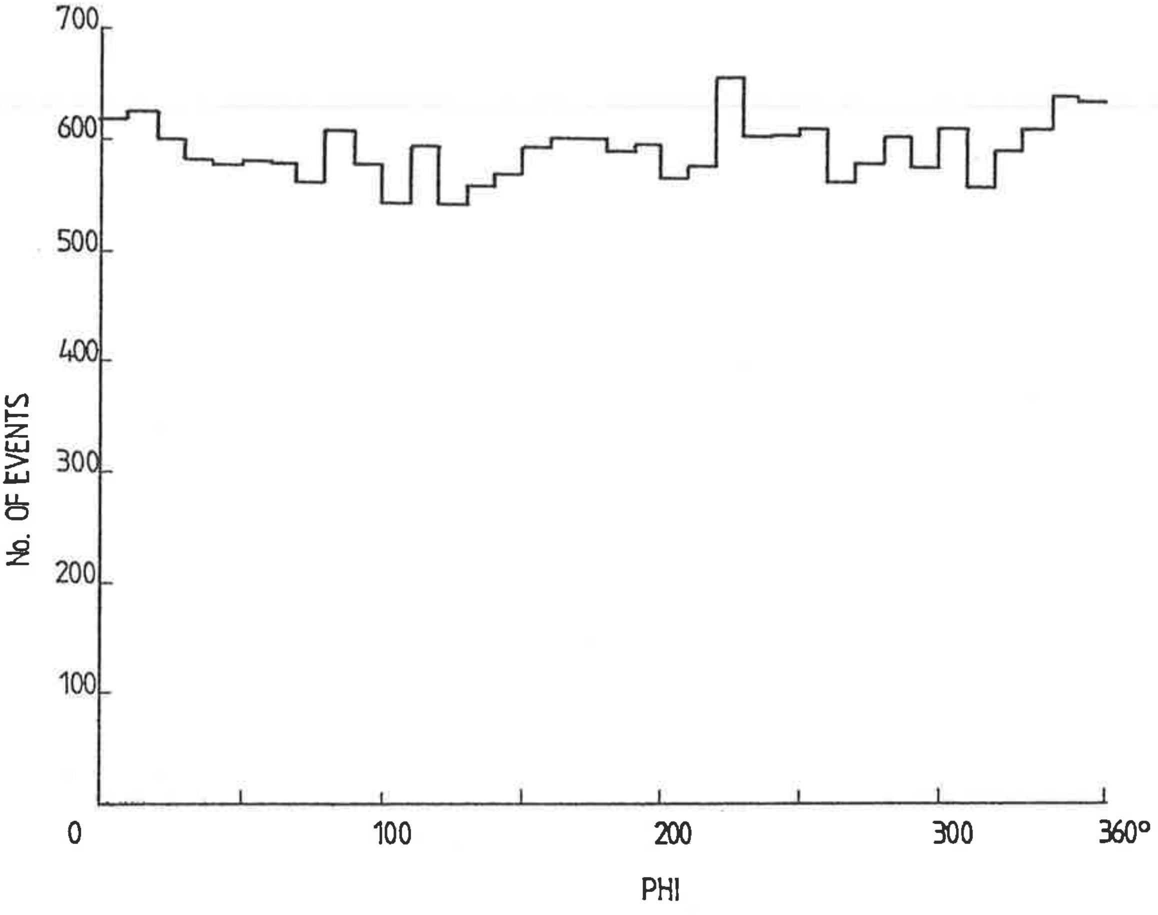

Figure 5.2 The phi distribution for the array from ≃ 23,000 events.

density plots seen in Figures 5.3 to 5.10. Over the entire area of the array, 5m x 5m square elements are considered. A sample of data ( one of a number ) is analysed using one of the possible analysis methods and the core locations are binned in the 5m x 5m squares. These are then represented in diagrammatic form using a program written by L. Campbell. On the diagrams the centre of each 5m x 5m bin is represented by a rectangle which has a size that is proportional to the value in that bin. The largest bin value produces the largest rectangle which is adjusted so as to just not overlap any other rectangles. If the value in a bin is sufficiently small then a only a point is drawn. In this way the groupings of the cores can be seen.

The examples are shown with two separate core plots with each set consisting of between 3000 and 6000 events. The top plot of each set is for those with shower cores with sizes < $10^5$ particles whereas the lower plot is for those with sizes >= $10^5$, to show the effect that shower size has on the results. The size value of $10^5$ was also approximately the lower threshold of the old array and so the plots with sizes > $10^5$ also indicate the showers the old array would have detected. There is also a $\chi^2$ cut so that poorly fitted events which have a $\chi^2$ of > 10 are not included in the core plots.

Initially the standard form of $\chi^2$ ( Form A in section 4.2 (a) ) was used in conjunction with MINUIT and a NKG fitting function. This $\chi^2$ is given below, where N is the number of huts with non-zero densities, D(I) are the observed densities and CD(I) are the calculated densities:

$$\chi^2 = \sum_{i=1}^{N} \frac{(D(I) - CD(I))^2}{CD(I)} \qquad \text{( see Figure 5.3 )}$$

This form of $\chi^2$ produced core plots as shown in Figures 5.3 (a) and (b). The total number of events considered was 5885 and from these only 4 were excluded due to $\chi^2 > 10$. The number of events $< 10^5$ particles was 2982 and the number $>= 10^5$ was 2899. Hence this method found $10^5$ to be close to the median size. As can be seen if the overlay ( in back flap ) of the array is placed on the core plot there is no smooth plateau of cores as was expected. The vast majority of events are being placed on or near huts. The mean NKG age found considering all 5881 events was 1.61. This is rather high and results from the large core errors for the showers. If for some reason the fitting procedure cannot locate the true core of the shower then the best fit found will generally be a flat distribution as this reduces the value of $\chi^2$. This corresponds to a large age.

The so called modified form of $\chi^2$ ( Form B, section 4.2 (a)) was then tried ( as below ) with its results shown in Figures 5.4 (a) and (b).

$$\chi^2 = \sum_{i=1}^{N} \frac{(D(I) - CD(I))^2}{D(I)} \qquad \text{( see Figure 5.4 )}$$

This form did not produce the "hut seeking" tendency that the standard form of $\chi^2$ produced but it did produce a response that was just as unsatifactory. Out of the 5885 total events considered, 5768 had $\chi^2$ values $< 10$ and of these 5113 are found in the plot with sizes $< 10^5$ particles. Hence almost all of the showers were fitted with a very small size. Upon further examination this problem was found to be quite extreme as $\approx$ 750 of these events were assigned sizes $<< 10^3$ particles with cores on (0,0). Many of these were given sizes of just a few particles

( and even fractions of particles! ) as a result of the distorted fitting procedure. This procedure would take a small flat shower with, for example, 1-10 particles observed in 15 huts, and assign all huts a calculated density of zero except for hut C which would have a few particles. However due to the large number of huts in the fit, the value of $\chi^2$ was still < 10. This explains the central feature seen in Figure 5.4 (a) and the (0,0) bin was found to contain ≃ 680 events ( i.e. more events than were found with sizes > $10^5$ particles! ) The mean age found from the 5768 events was 1.03 which is low and is a result of the large number of small steep showers that were fitted.

To compare with these two more usual forms of $\chi^2$, other variations were attempted. As it is only the denominator that has changed in these cases, only this will be shown.

(1) $$\frac{1}{(D(I).CD(I))^{1/2}}$$ ( see Figure 5.5 )

This hybrid version of $\chi^2$ was tried as a compromise to the standard and modified forms and produced the core plots shown in Figures 5.5 (a) and (b). Out of 5885 events, 5848 had $\chi^2$ < 10, with 4051 having sizes < $10^5$ and 1797 sizes >= $10^5$. This method uses the geometric mean of the calculated and observed densities and still produces the tendency for cores to land on huts, in particular huts W,X and A, especially for the showers < $10^5$ in size. However, when the individual fits were examined, the correspondence between the observed and calculated densities was reasonable, in particular for the large observed densities. The mean age was 1.3.

(2) $$\frac{1}{(D(I)+CD(I))/2}$$ ( see Figure 5.6 )

This form of $\chi^2$ is similar in principle to the hybrid version of (1) as it is a compromise. It is the arithmetic mean of D(I) and CD(I) and could be considered to be a possible conclusion of the work of Awaya (1979) as mentioned in section 4.2 (a). Out of a total of 3615 events considered, 3574 had $\chi^2$'s < 10 and of these 3574 were fitted with sizes < $10^5$ particles and 2409 with sizes >= $10^5$. The mean age produced by these 3574 events was 1.33 but it can be seen from Figures 5.6 (a) and (b) that the method still results is too many cores on hut locations.

(3) To test if the fitting problems were caused by limitations in the MINUIT package it was decided to use the standard form of $\chi^2$ with a NKG fitting function and utilise the IMSL minimisation routine (called ZXMWD). The results are shown in core plots Figures 5.7 (a) and (b). From 5885 events only nine were excluded with the $\chi^2$ cut. 3623 events were assigned sizes < $10^5$, 2253 events were assigned sizes >= $10^5$ and a mean age of 1.4 was found. However a strong tendency for the huts to be singled out as core locations is seen. This implies that the effect noted in the standard $\chi^2$ fit is not changed with the use of a newer minimisation routine. Also ( as mentioned earlier ) the ZXMWD package took about four times as long as MINUIT to find solutions.

(4) To test the effect of the fitting function, the Moscow lateral distribution function ( with the standard form of $\chi^2$ using MINUIT ) was attempted. The results are seen in core plots

Figures 5.8 (a),(b). However, in general the fits were considerably poorer, even allowing for the increase in $\chi^2$ that eventuates as the number of fitted parameters is decreased ( as there is no age parameter ). From 5885 events, 1254 were rejected with the $\chi^2$ cut to leave 4631 events. Most of these rejected $\chi^2$'s were very large ( > 50 ) and so would not be included even if the $\chi^2$ acceptance was made more generous. 3343 showers were assigned sizes < $10^5$ and 1288 were >= $10^5$. There is no apparent tendency for cores to be placed on huts but there was a tendency for unrealistic sizes of < $10^3$ particles to be assigned to the showers ( which explains plot 5.8 (a) ). Additionally, on plot 5.8 (b) there appears a "hole" in the core densities on the south west side of the array. This may be genuine but may be a statistical effect.

(5) The maximum likelihood method as described in section 4.2 (b) using the NKG function and MINUIT was also used. The core plots are seen in Figures 5.9 (a) and (b). The data set for this method is larger being 26129 events with 17708 being given sizes < $10^5$ particles and 8421 with sizes >= $10^5$. The mean age found for this work was 1.42. As can be seen in the plots, the trend still exists for cores to be placed on huts. However this tendency is not as marked as for the standard form of $\chi^2$ and hence the use of the maximum likelihood method seems preferable to this. There are still some fitting problems associated with this method as was seen when an examination of the ages was made. When larger sized events were examined ( > 5 x $10^5$ particles ) many events were not fitted correctly as they were assigned age values of 2 (the upper limit of the age parameter and the upper

limit given to MINUIT ). This implies that these larger showers have significant core errors as their lateral distributions have been flattened to produce the best fit. This explains the relatively high mean age that was found for the ≈ 26000 events.

(6) The core distributions obtained from the QUIKFIT program were examined to test the results of an alternative fitting routine which was designed simply to find a rough estimate of the core. These are seen in Figures 5.10 (a) and (b). 5885 events were used and of these 5817 had $\chi^2$ 's < 10. Sizes of < $10^5$ were assigned to 4314 of these events and 1503 had sizes >= $10^5$. The main effect is seen in (a) where the core distributions follow a square pattern, presumably as a result of the square grid technique used to search for the cores. Other than this the core distributions appear acceptable, although the statistics are fairly poor in the size range >= $10^5$.

The core plots that have been presented in Figures 5.3 to 5.10 represent the main analysis methods that have been examined. However other alternatives were tried, as presented below:

$$\frac{1}{(0.1 + (CD(I).D(I))^{1/2} + 0.01.CD(I).D(I))}$$

This is a version of the hybrid $\chi^2$ which was used to consider the effect of noise, represented by the first term, and electronic sampling errors, represented by the third term. This form of the standard deviation was suggested by Lai and MacKeown (1981). However, it produced a very similar result to the hybrid version in (1) and did not resolve the core location problems.

$1/D(I)$ for $D(I) < 25$ particles $m^{-2}$

$\dfrac{1}{(0.2.D(I))^2}$ for $D(I) >= 25$ particles $m^{-2}$

This is a version of the modified $\chi^2$ which attempts to reduce the contribution of the large observed densities in the fits. It is possible that the large densities may be contributing too heavily to $\chi^2$ and hence causing the cores to be placed on these detectors. This method reduces the value of the denominator of $\chi^2$ for densities > 25 particles $m^{-2}$ as it sets the standard deviation to 20% of the observed density, corresponding to the measurement errors. However no improvement appeared in the core plots. A large number of small events were still fitted very poorly at (0,0) with sizes << $10^3$ and the core plots appeared similar to that presented in Figure 5.4.

As an extension to this, when < 25 particles were present in the detector, the denominator of $\chi^2$ was changed to the hybrid version as given in (3). This removed the unrealistic size assignment but introduced the hut seeking tendency again and hence was not considered an improvement.

Another variation involved, as a test case, the removal of the denominator of $\chi^2$ completely (i.e. replacement of the denominator with one ). This is equivalent to the setting of the standard deviation for all events equal to one and hence is very unrealistic. The set of solutions produced by this method however was well distributed in core, size and age. Even though $\chi^2$ varied from 0.1 up to 2000 ( the numerical meaning of $\chi^2$ as a measure of fit in this instance would be different to the standard form but a value for a good cut-off is not known ) the shower cores were well spread over the array in a manner that looked reasonable. Also, most sizes produced were acceptable, except that too many showers appeared between $10^3$ and $10^4$ in size. However there were undoubtedly many poor fits as the ages had hit the limits ( i.e. 0.5 or 2.0 ). Nevertheless the method indicated that if a good percentage of possible solutions could be found with merely the numerator of $\chi^2$, there should be hope that a method using a more correct form could be found in the future.

A variation of the above method, namely that given below, was also tried. This was an attempt to give more weight to the densities < 5 particles $m^{-2}$ so that they would contribute more to the $\chi^2$ sum. However this did not work as the tendency for cores to land on huts re-appeared.

$$1/1 \qquad \text{for } D(I) =< 5 \text{ particles } m^{-2}$$

$$\frac{1}{(D(I).CD(I))^{1/2}} \qquad \text{for } D(I) > 5 \text{ particles } m^{-2}$$

Methods which varied the minimum distance that a shower core could approach a hut in the $\chi^2$ search were also used. For all the $\chi^2$ methods mentioned so far, this minimum distance was arbitrarily set to 0.1 m and hence many cores would be placed 0.1 m from a hut location. This minimum distance was changed to $10^{-6}$ m and the hybrid form of $\chi^2$ was used. However little effect was seen in the results except that cores would now land exactly on a hut as opposed to 0.1 m from one. This lead to the conclusion that this was not the problem. Also attempted was the inclusion of all densities, including the huts with zero particles, in the fits. Theoretically there is support for including zero densities as they are observed values and should

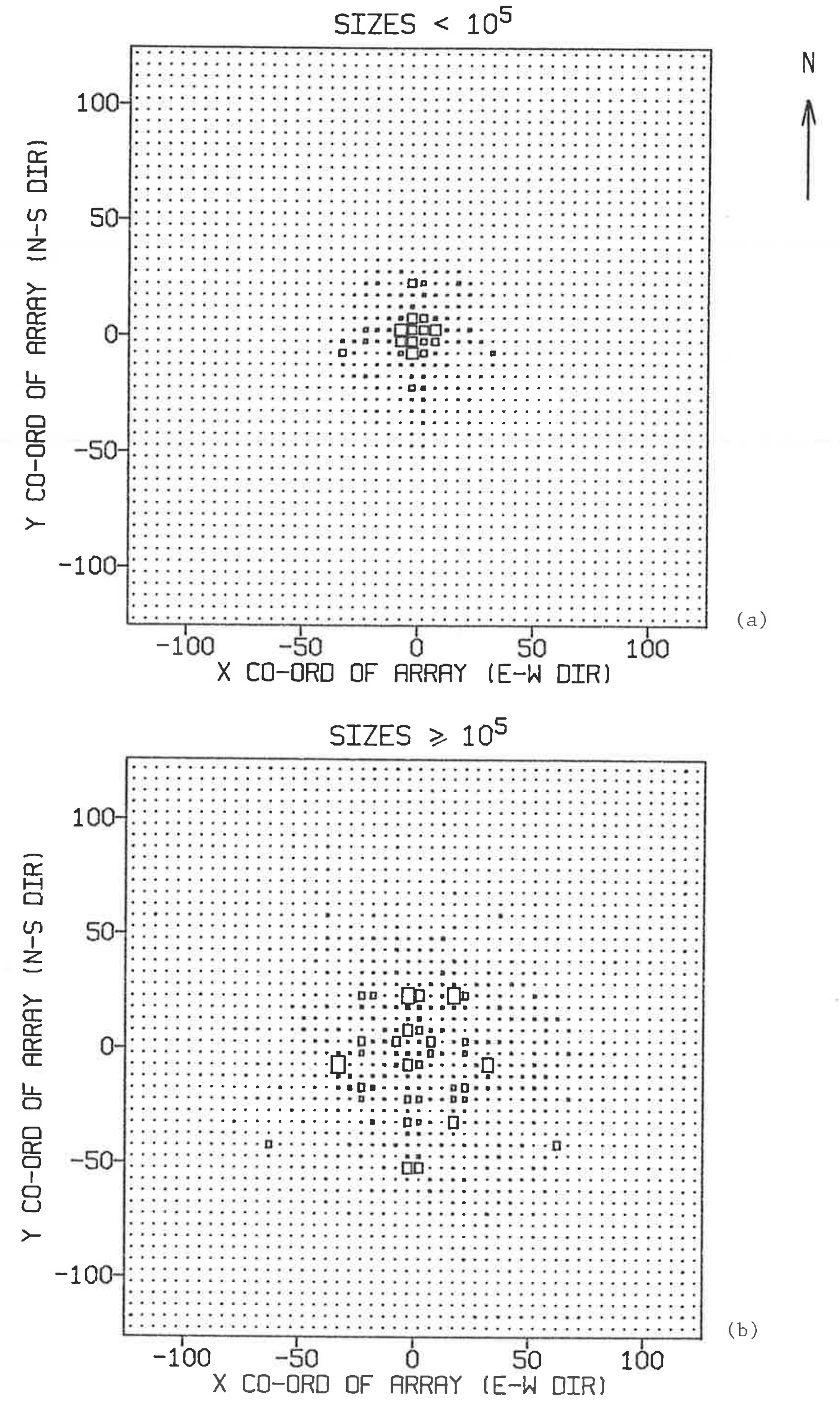

Figure 5.3 Core distributions using the standard $\chi^2$ (Form A, see text).

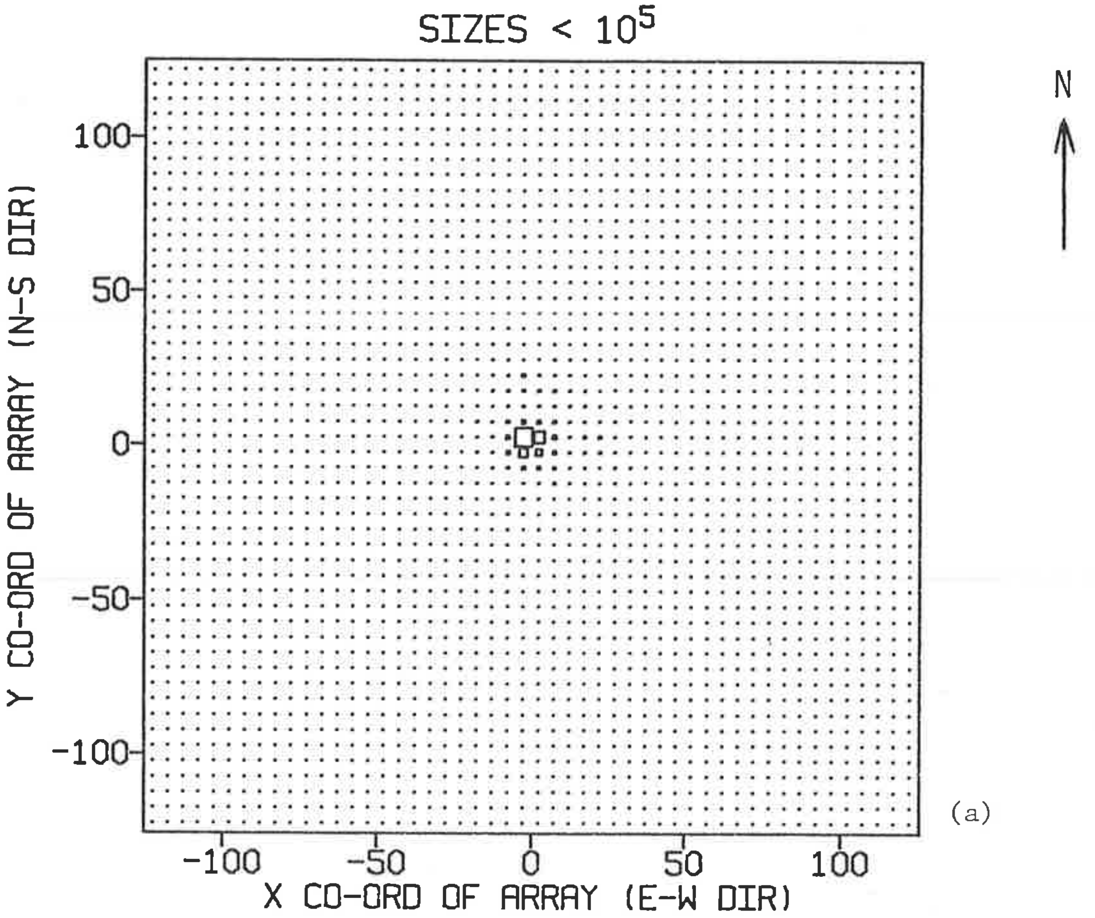

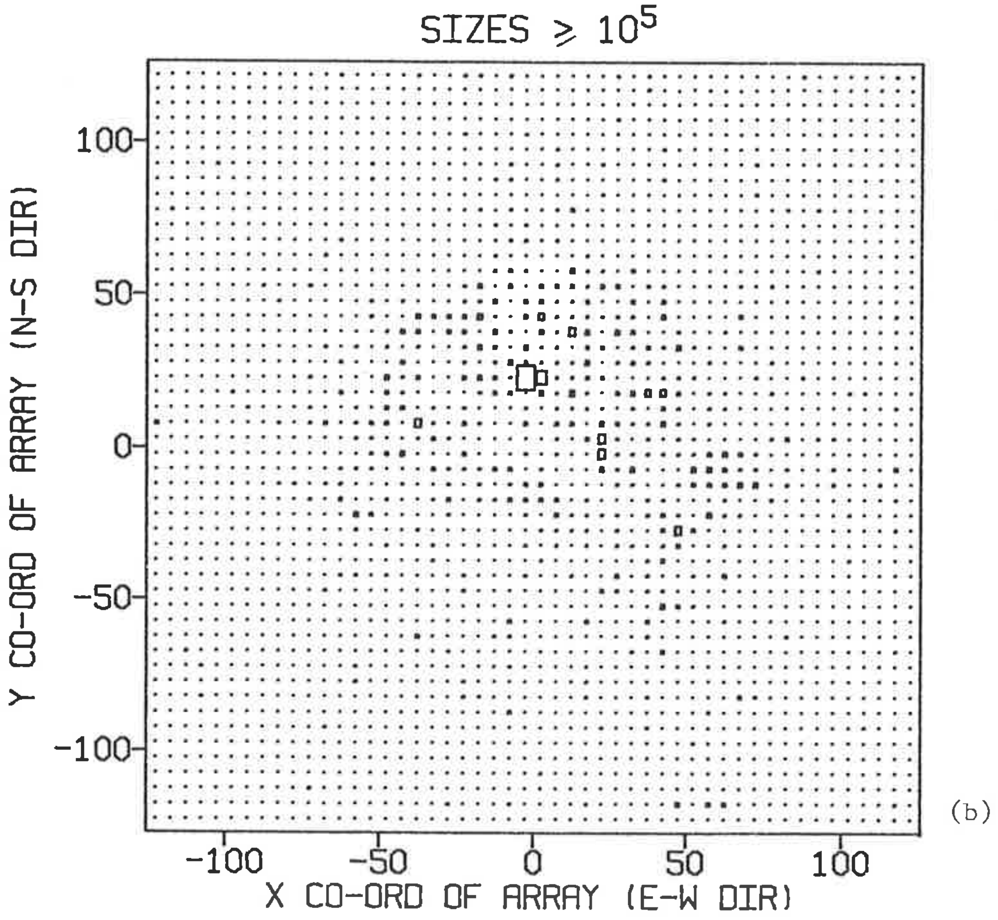

Figure 5.4 Core distributions using the modified $\chi^2$ (Form B, see text).

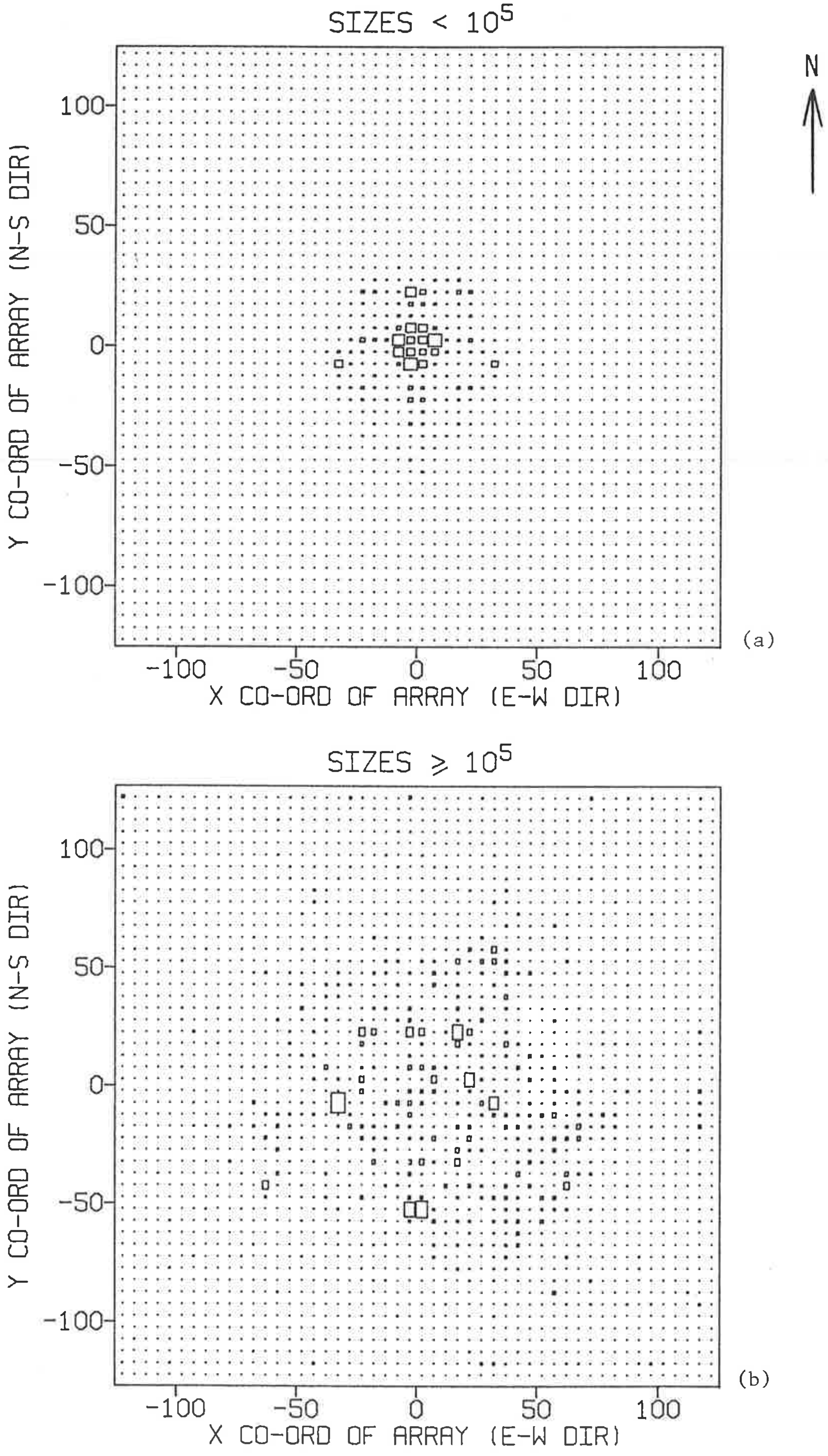

Figure 5.5 Core distributions using the "hybrid" geometric mean form of $\chi^2$ (as in (1), see text).

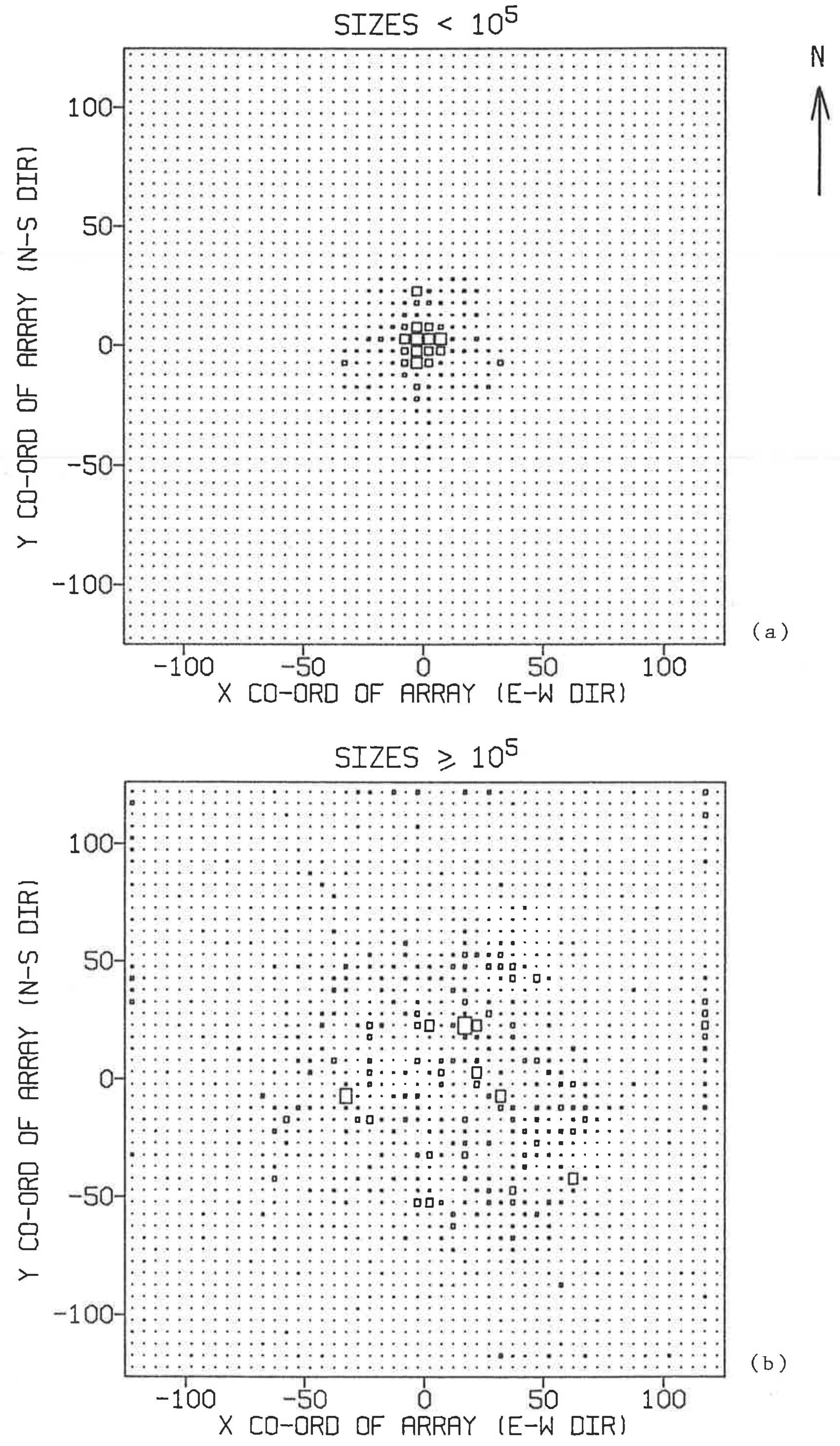

Figure 5.6 Core distributions using the arithmetic mean form of $\chi^2$ (as in (2), see text).

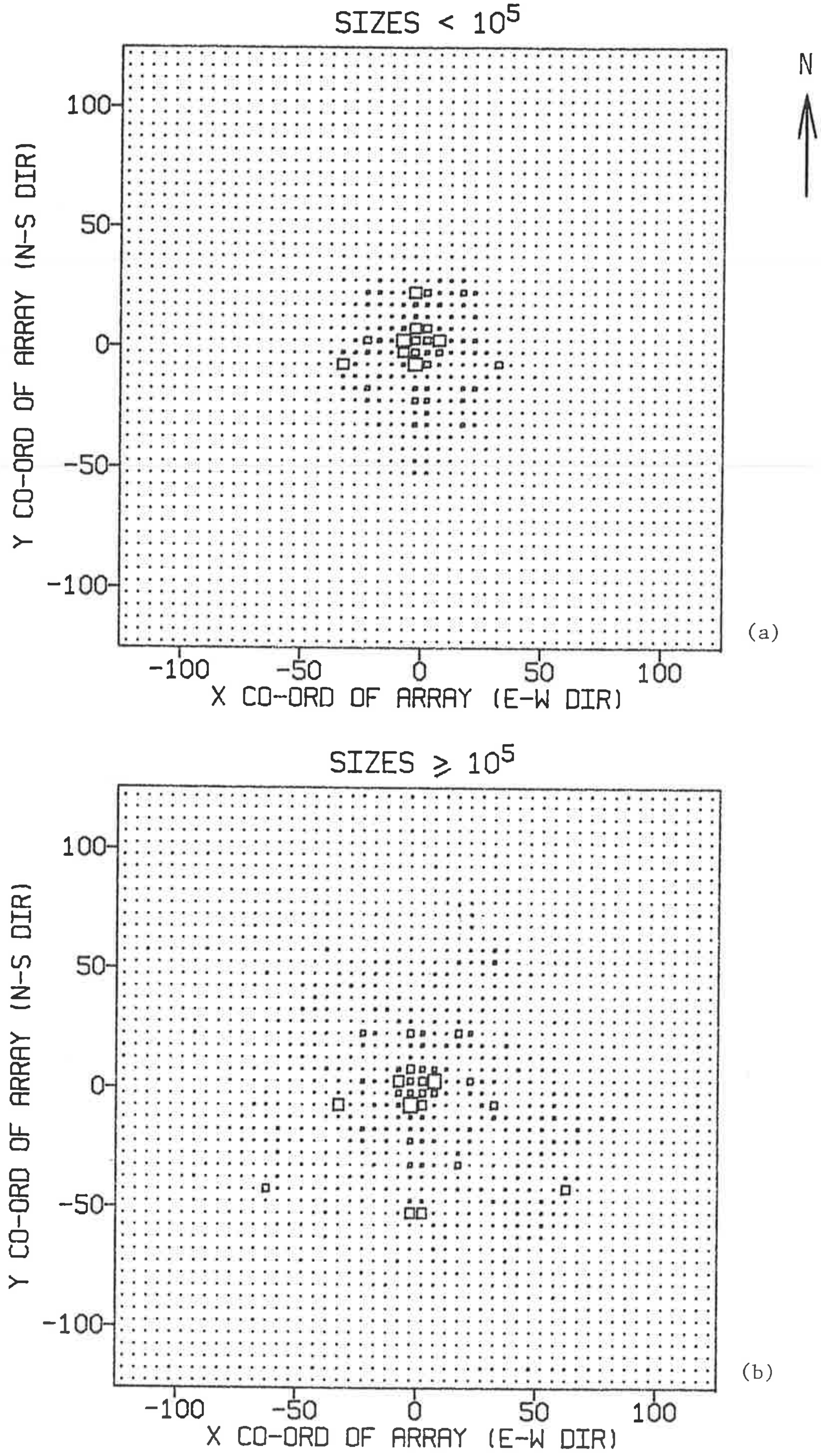

Figure 5.7 Core distributions using the ZXMWD (IMSL package) minimisation routine (as in (3), see text).

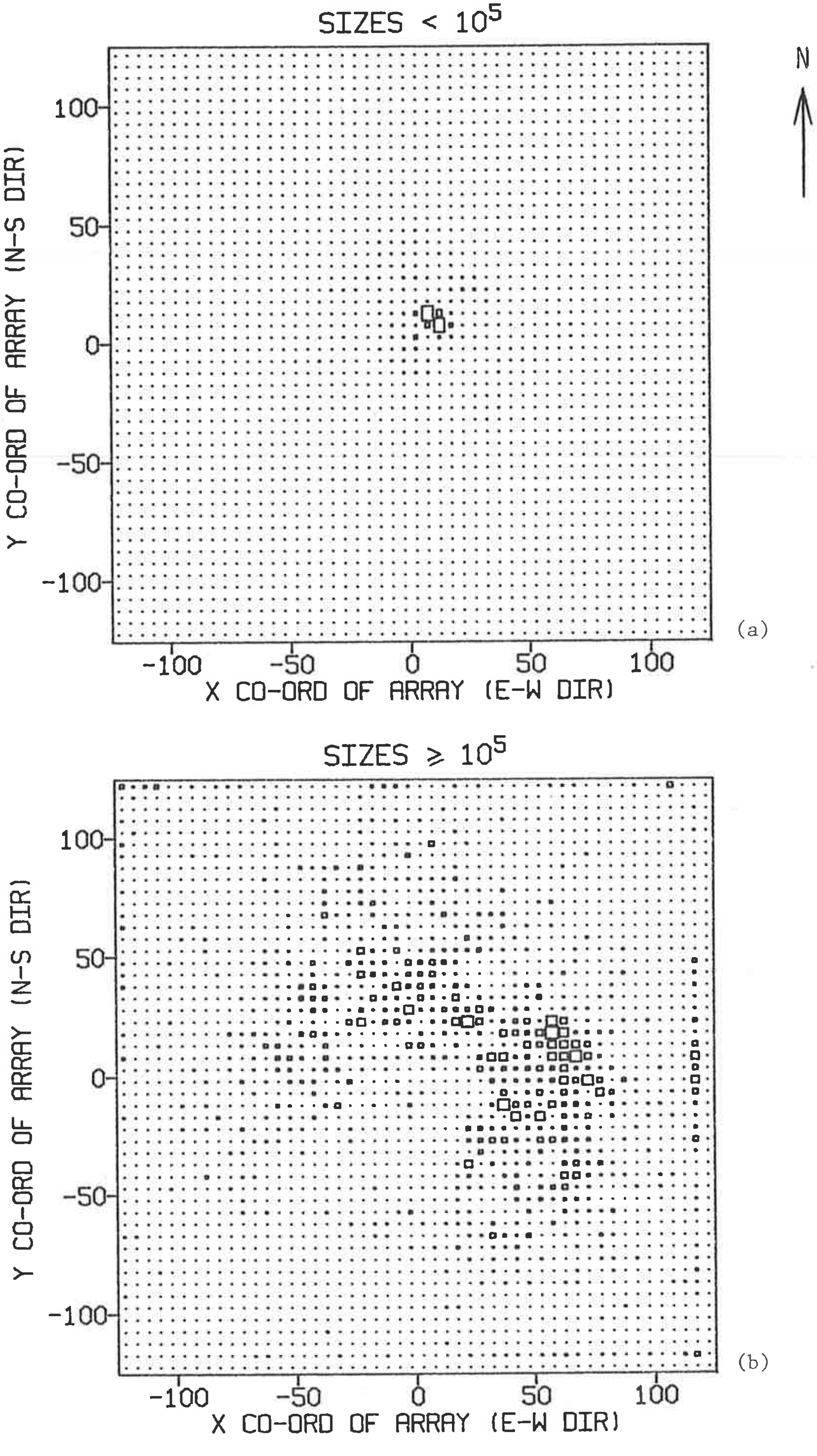

(a)

(b)

Figure 5.8 Core distributions using the Moscow-MIT fitting function (as in (4), see text).

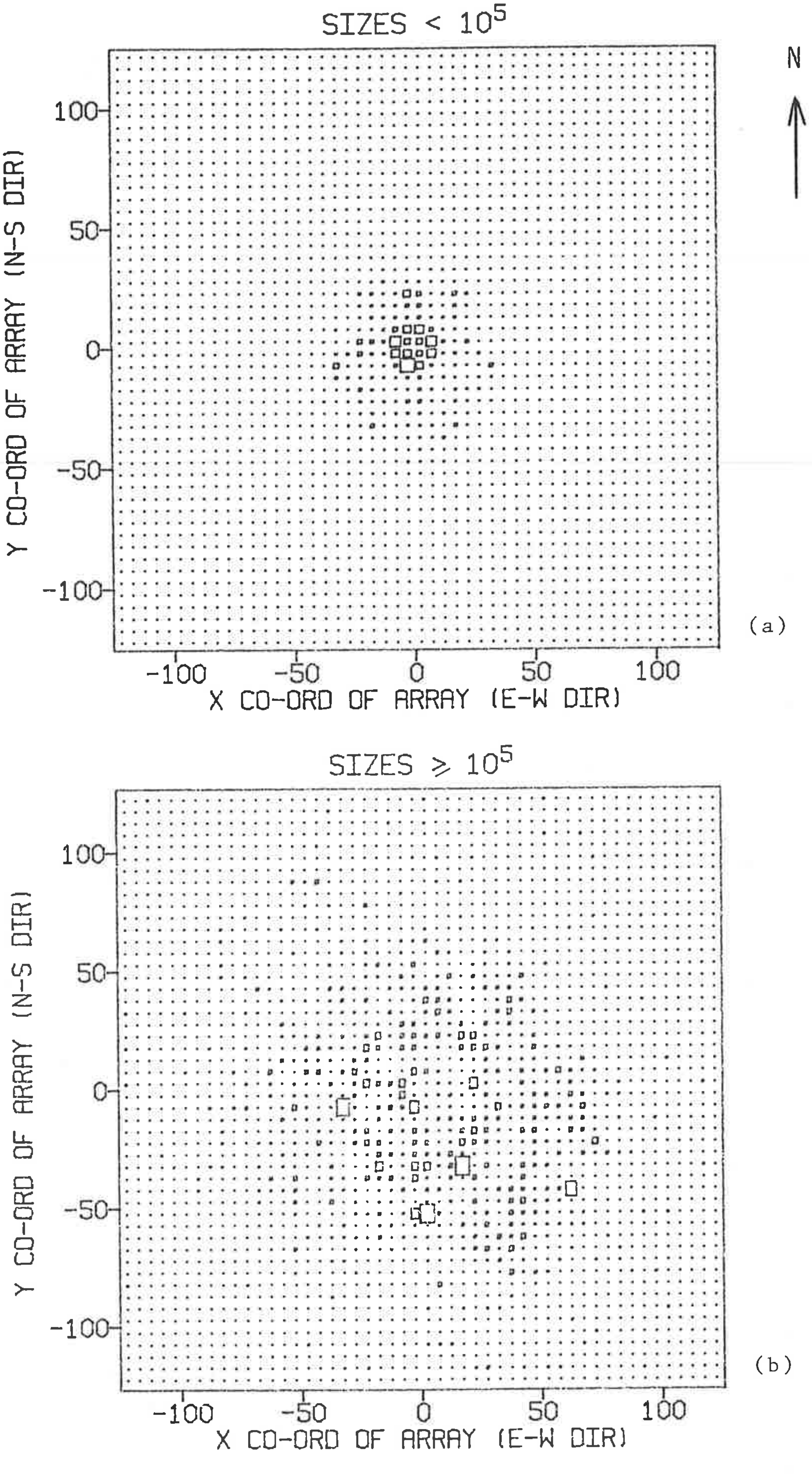

Figure 5.9 Core distributions using the maximum likelihood method (as in (5), see text).

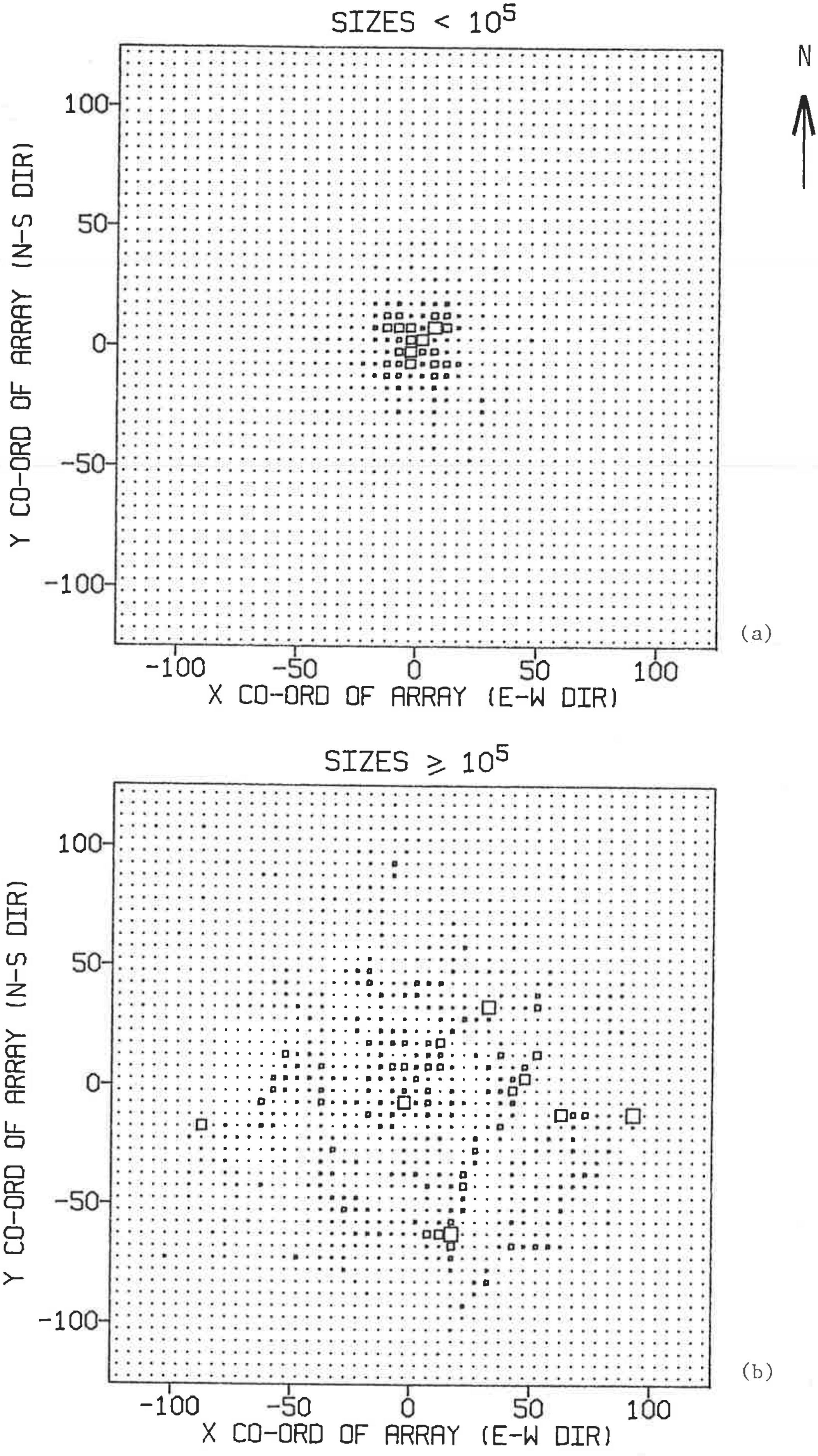

Figure 5.10 Core distributions using the QUIKFIT program (as in (6), see text).

be considered. However, in reality, no improvement was observed and a large number of very poor fits ( to otherwise moderately well fitted events ) were obtained. Additionally, the inclusion of all 27 density values ( especially for small showers where only the central detectors have fired ) increased the analysis time considerably.

## 5.5 CONTOURS OF CHI-SQUARED

One method that was used to assess the various problems that arose with the analysis was the examination of the $\chi^2$ contours that were produced. MINUIT has an optional command which allows the user to examine the contours of the minimised function around the minimum. The user can request the number of contours required and also the spacing between the contours. However the user has no other control over the region of the minimised surface that will be presented and so often, very small or very large regions are drawn. If MINUIT finds the user's requests too demanding ( e.g. it takes too many iterations to find the next point or that the contours extend beyond the allowed region ) then that contour will not be printed.

In this work the contours of $\chi^2$ were plotted on the x-y surface but they did not prove very helpful. Often none or only one of the requested contours were drawn. This may suggest that the $\chi^2$ was very flat and so the contours could not be found. This situation could apply for a shower that has an incorrect core fitted with a large s and hence a flat distribution. This flat distribution should mean that large movements in the core location would result in very small changes in the value of $\chi^2$. However, it is not certain that this is the case and the contours examined for such situations did not clarify the problem.

Just as confusing were the contours produced for a number of solutions which landed on huts. Often flat or very complicated surfaces would be apparent but also quite often a deep, circular well of $\chi^2$, would be seen implying a very good solution. Similarly, contours of events that appeared to be good solutions ( i.e. not near a hut with a low value of $\chi^2$ ) would show all types of contours. Hence the use of the CONTOUR command as a tool for problem solving in this particular instance was not very useful. However as only small samples of events were used it is possible that more work in this area could be fruitful.

As an example of the type of contours produced by MINUIT, three have been presented. Figure 5.11 shows an example of a contour of an event that has landed on a hut and therefore is a suspect solution. The contours are very symmetrical and are the type of contours that would be seen in an simulated unfluctuated event. Figure 5.12 shows an event that also has a solution on a hut but which produces a much more complex $\chi^2$ surface. Similarly Figure 5.13 indicates an event which was placed well away from hut locations but also produced a complex $\chi^2$ surface.

## 5.6 THE AGE RESULTS

Using MINUIT and the NKG function an examination of the ages produced by two methods was made. These methods were the hybrid form of $\chi^2$ and the maximum likelihood method as described in sections 5.4 (1) and (5). Only vertical showers ( $\theta < 20^\circ$ ) were considered. Histograms of the age distributions are shown in Figures 5.14 and 5.15.

Using the hybrid $\chi^2$, the shower parameters, including the age, were found for 5638 vertical showers ( all with $\chi^2 < 10$ )

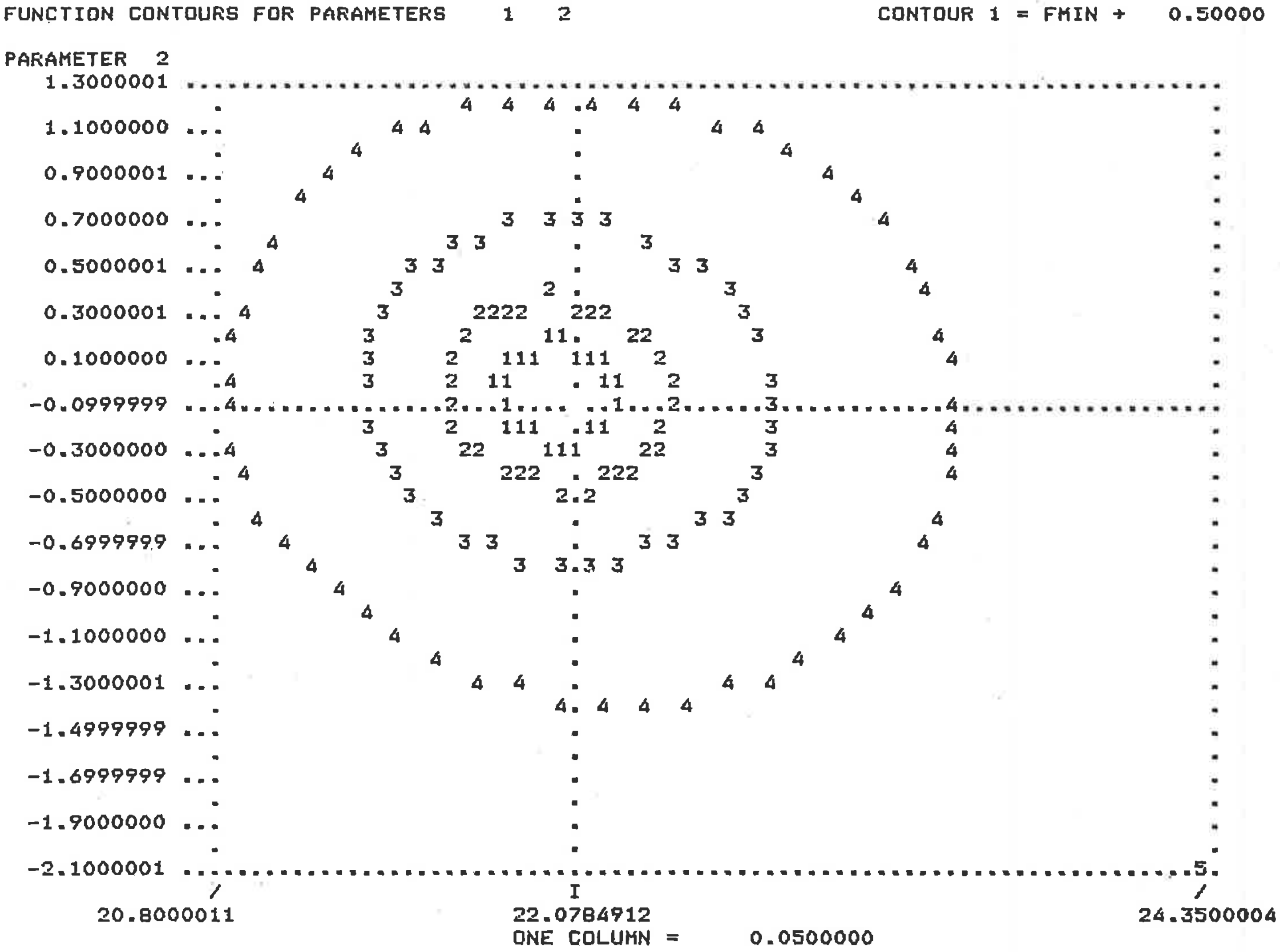

Figure 5.11 Contours of $\chi^2$ produced by MINUIT, for an event that has been placed on hut A at (0,22).

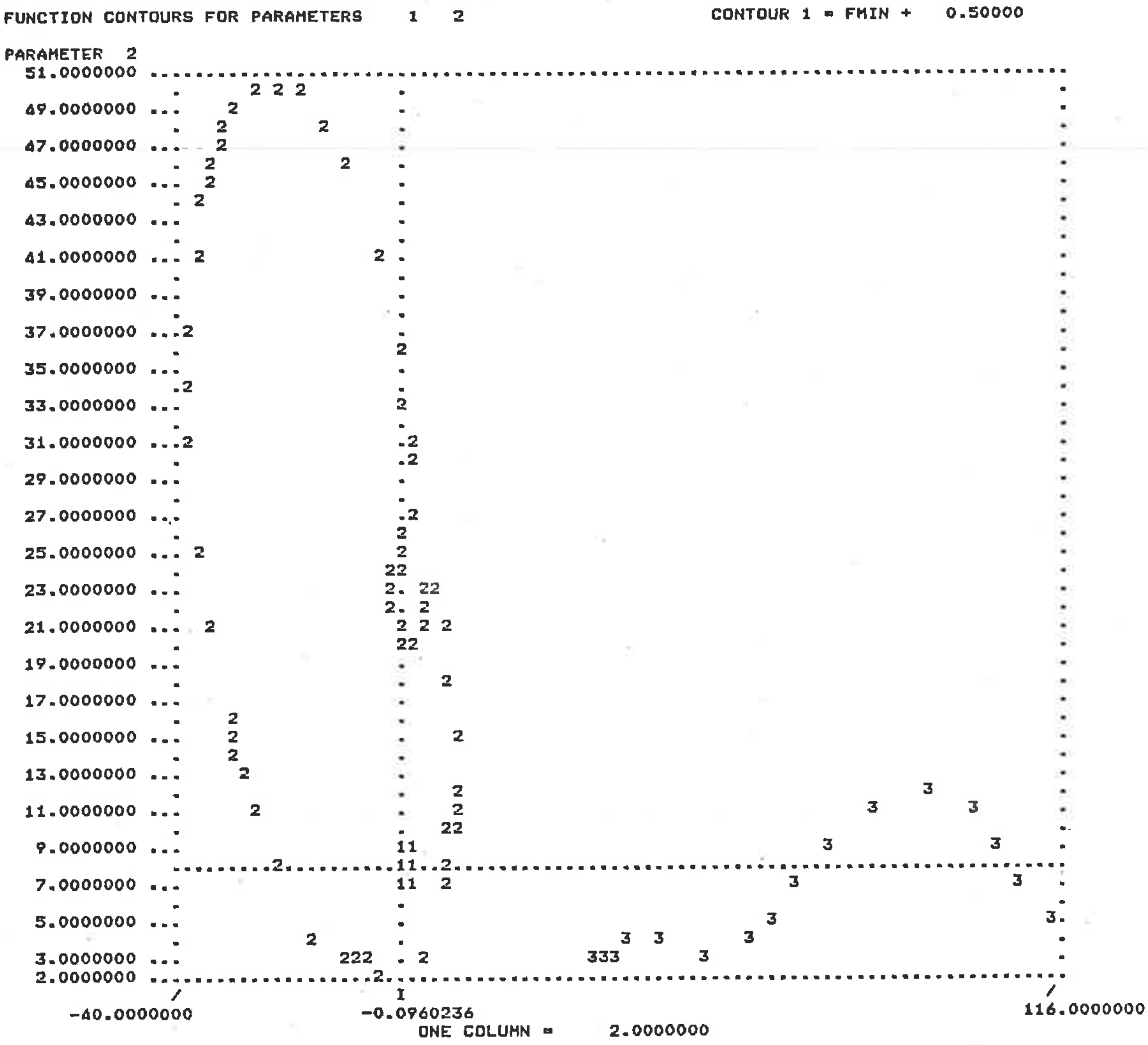

Figure 5.12 Contours of $\chi^2$ as produced by MINUIT, for an event that has been placed on hut A1 at (0,8.5).

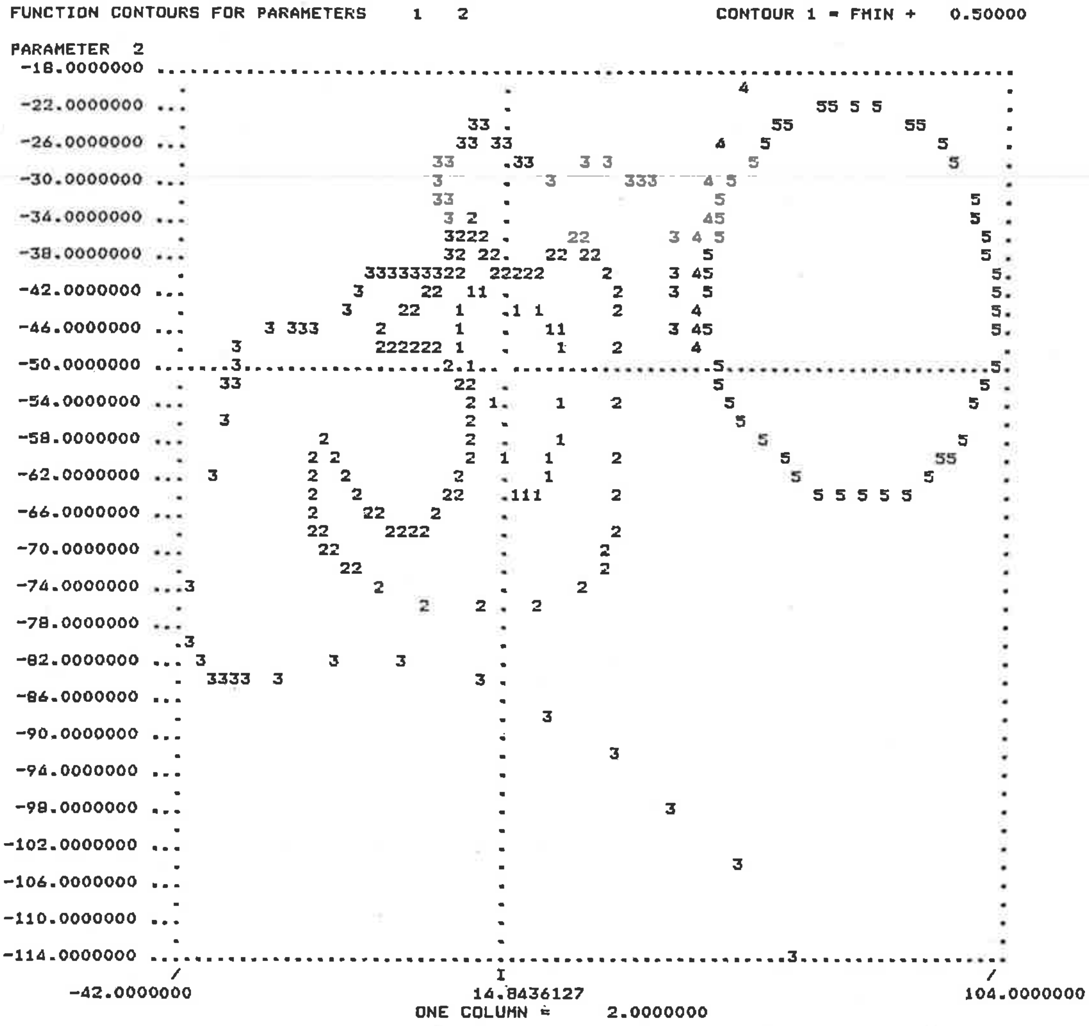

Figure 5.13 Contours of $\chi^2$ as produced by MINUIT, for an event that has been placed in an empty region of the array, at (14.8,-50).

and the events were binned into seven shower size bins. These bins were ( in particles ): Ne < $2x10^4$, $2x10^5$ < Ne <= $5x10^4$, $5x10^4$ < Ne <= $10^5$, $10^5$ < Ne <= $2x10^5$, $2x10^5$ < Ne <= $5x10^5$, $5x10^5$ < Ne <= $10^6$, and Ne > $10^6$. The ages in each size range were placed into age bins from 0.5 up to 2.0 in steps of 0.1. However the events with ages 0.5 or 2.0 have not been included in the diagrams or in the calculations as these bins mostly contain events that have not been well fitted and have hit the age limits given to MINUIT. ( This is seen in many instances by a large excess in these bins, and this excess in a few instances extends to the adjacent bins ). In Figure 5.14, for the hybrid $X^2$, the set of seven histograms for the size ranges are seen. The boxes contain the information relevant to each histogram, namely the size range, mean size of the sample, mean age with the error in the mean age, and the percentage of events that have not been included due to the events being in the 0.5 or 2.0 age bins. It can be seen that it is only when the shower size exceeds 5 x $10^5$ particles that substantial numbers of events are excluded in the end age bins.

Figure 5.15 shows the age histograms obtained when the maximum likelihood method is used. A total of 12,015 events were analysed. In general the mean ages are larger for this method than for the hybrid $X^2$ and the distributions are broader. However, there are many poorer fits and the percentage of events that must be excluded in the 0.5 and 2.0 bins is larger, especially between 5 x $10^5$ and $10^6$ particles. There are also more excesses observed in the other high age bins which will contribute to the higher average ages. Hence it was felt that the age results from this method were not as reliable as results obtained using the hybrid $X^2$.

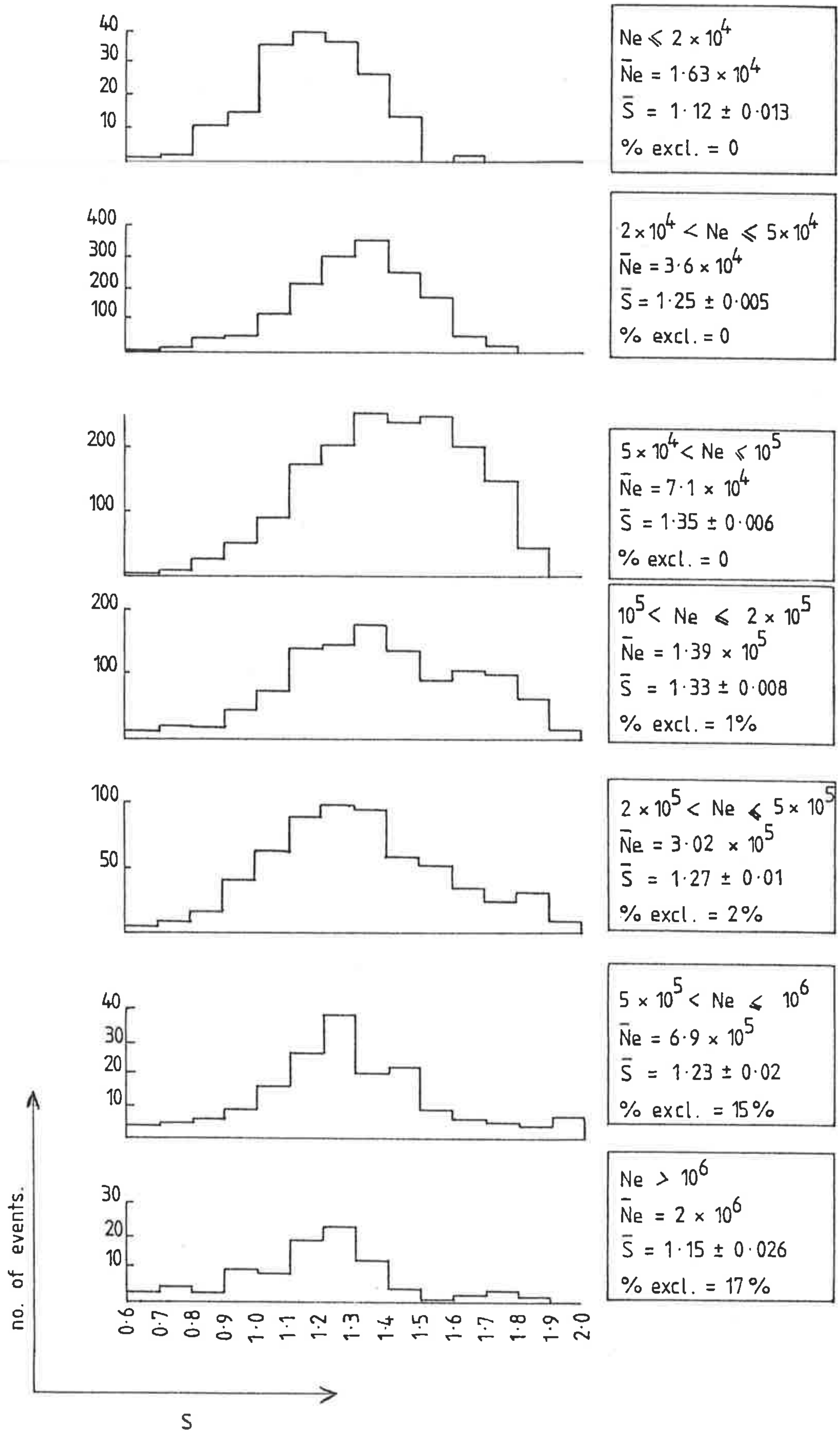

Figure 5.14 Age distribution histograms, for seven size ranges, using the "hybrid" $\chi^2$ method. (for showers with $\theta < 20^o$)

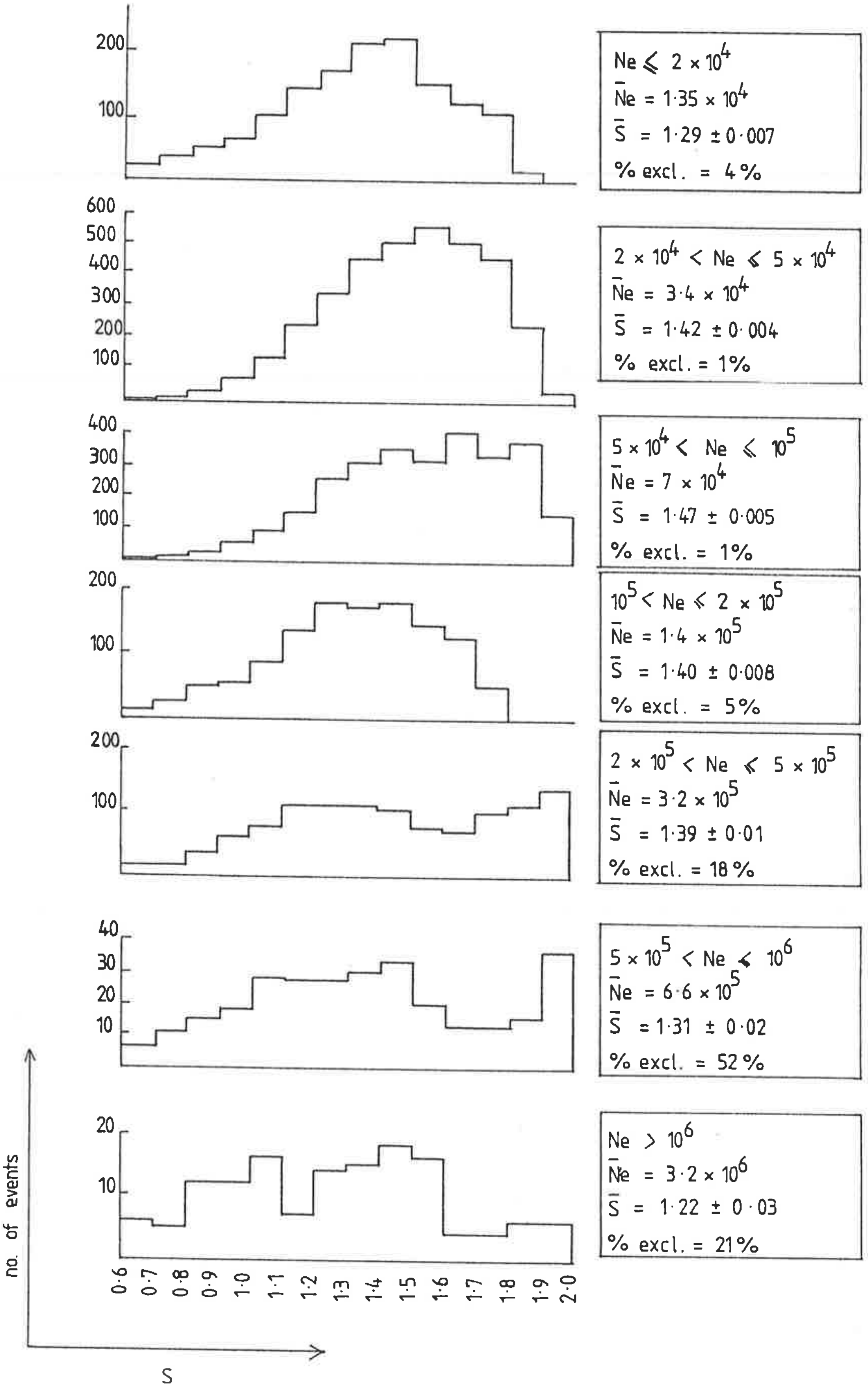

Figure 5.15 Age distribution histograms, for seven size ranges, using the maximum likelihood method. (for showers with $\theta < 20^o$)

The mean ages found using the hybrid $\chi^2$ were plotted against mean size and are shown in Figure 5.16. Also shown are age results from other workers who have undertaken similar work, as well as the vertical shower age results for the original Buckland Park array ( Acharya et al. (1979), Abdullah et al. (1981), Chaudhuri et al. (1985), Clay et al. (1981) ). It can be seen that above the size of $2 \times 10^5$ particles, the results are in agreement with most others including the earlier Buckland Park results. Below this size, down to $10^5$ particles, the mean age is higher than other workers have found. This may be a genuine effect due to the greater ability of the array to observe smaller showers without selection effects, and that the observed reduction in mean shower age for other groups results from their own selection biases. Similarly, the results of this work below $5 \times 10^4$ particles which indicate a lessening in the mean age are probably a result of the array selection effects, as discussed in section 4.1 (d). This is likely, as when the age distribution for the smallest size range is examined, there are practically no events fitted with ages greater than 1.5.

## 5.7 THE SIZE RESULTS

The observed differential rate spectra produced by the two methods, the hybrid $\chi^2$ and maximum likelihood, have also been obtained. These rate spectra can be used to derive the size spectrum for the array. To find the true size spectrum, an event should only be included if it has landed in a region that has a known triggering probability for that shower size. Generally this probability is chosen to be 100%. As it has been impossible to find sufficiently reliable triggering contours for either of these analysis methods, a size spectrum has not been

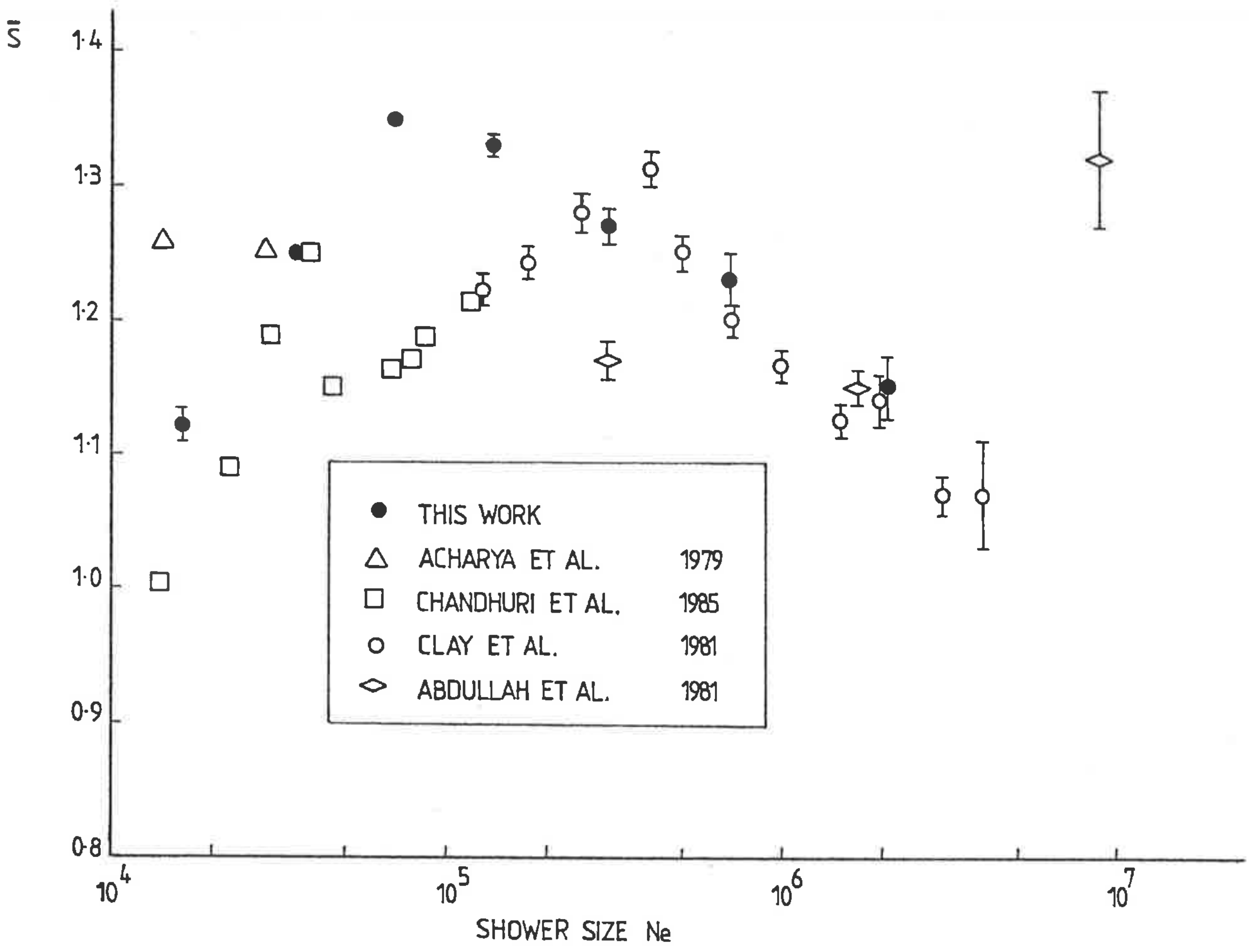

Figure 5.16 The mean age found using the "hybrid" version of $\chi^2$, for different sizes, compared to other work.

included here. However, the rate spectra that are presented show that the array analysis, although not yet perfect, is giving generally reasonable results.

The rate spectra are shown in Figure 5.17 as well as an approximate predicted rate spectrum for the array. This was calculated from the simulated 100% triggering contours shown in Figure 4.1 and the differential spectrum of cosmic rays at the top of the atmosphere as seen in Figure 1.2. Combination of these two figures yields the approximate differential spectrum that the array should observe. Two reasons for this prediction being approximate are that the simulated 100% contours are only approximations to the true contours of the array ( as mentioned in section 4.1 (b) ) and that the differential spectrum that is used can only, at present, be an approximate one.

It is seen that the spectrum found for the hybrid $X^2$ is quite close to the appromimate predicted spectrum. The spectrum produced from the maximum likelihood method is not as close but is still well approximated by it, at least for sizes greater than $5 \times 10^4$ particles. The spectrum produced for the hybrid $X^2$ shows the expected sharp fall-off for small sizes as the triggering probability for these sizes diminishes to zero. Unfortunately the maximum likelihood method does not show this effect and hence appears to be assigning many showers too small a size.

In conclusion it appears that the methods, and in particular the hybrid method of $X^2$, are producing reasonable estimates of the sizes and ages of showers that are detected by the Buckland Park array. It is also possible that the majority of showers that have been acceptably analysed are contained in the near 100%

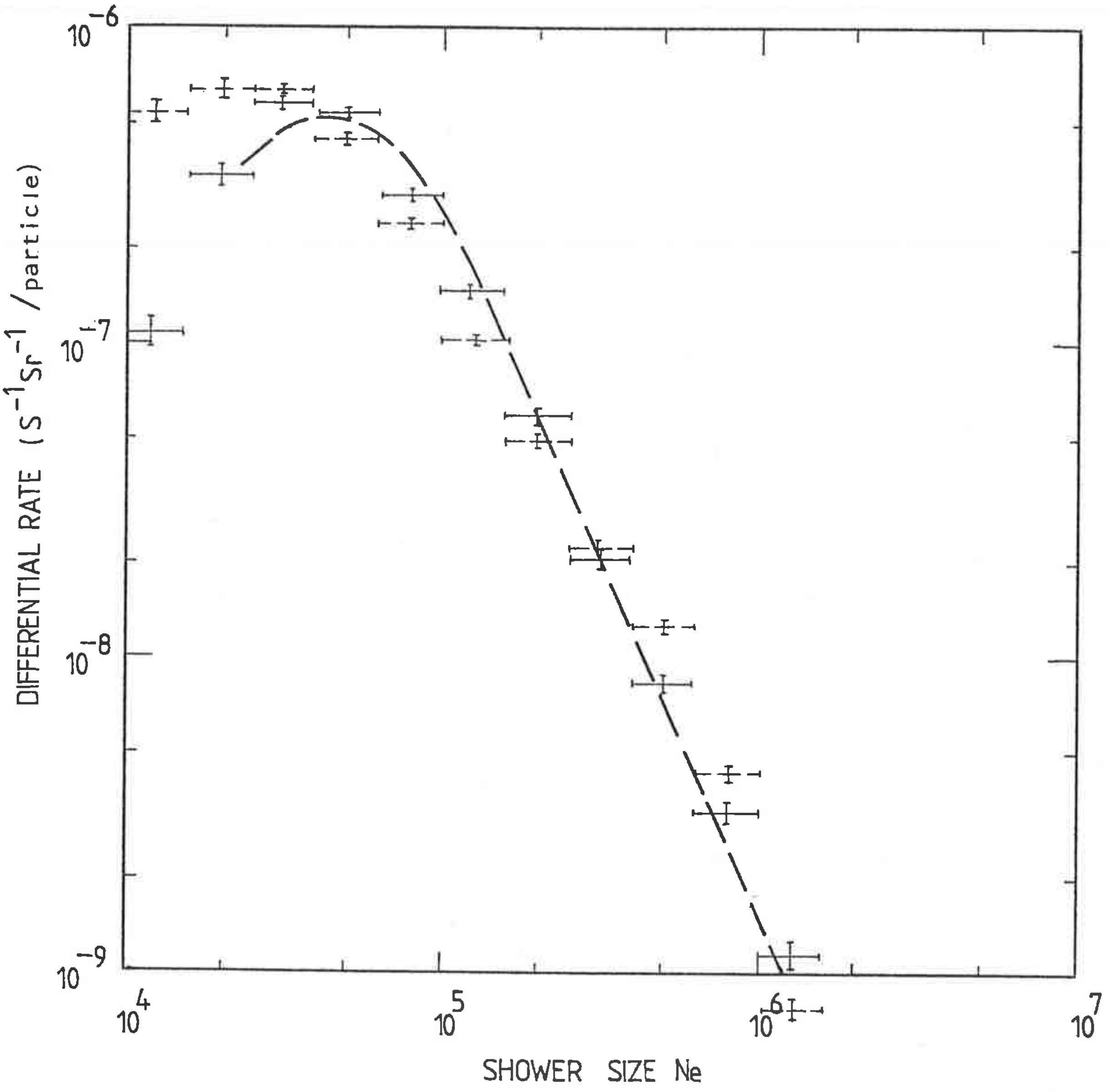

Figure 5.17 The observed differential rate spectrum of the array, using two methods of analysis. The solid bin lines are from the "hybrid" form of $\chi^2$. The dashed bin lines are from the maximum likelihood method. The dashed line is a rough estimate of the expected spectrum using the differential spectrum of Figure 1.2 and the simulated 100% triggering contours in Figure 4.1.

triggering areas of the array. Figures 5.14 and 5.16 provide convincing evidence that the shower sizes and ages derived using the hybrid $\chi^2$ formula are approximately correct for the majority of analysed showers.

# CHAPTER SIX

## CONCLUSION AND SUGGESTIONS FOR FURTHER WORK

This thesis has described the work performed in connection with the extensions to the Buckland Park array, together with a thorough examination of analysis methods applicable to the air shower data. As seen, the analysis of this data is not a simple process and difficulties have emerged as to which technique should be used. This thesis has presented the problems that arose and concluded that an analysis method that is reliable in every way has yet to be found. However, the hybrid form of the chi-squared goodness of fit test suggested here appears to have resulted in the best option that is currently available. This method, in conjunction with the NKG lateral distribution function and the minimisation package MINUIT, finds only approximate shower cores but any core errors do not appear to severely affect the fitted shower sizes and ages. However, a set of accurate collection areas for different size ranges has yet to be produced and so a differential size spectrum similar to those appearing in Figures 2.7 (a) and (b) has not been derived here. This area of the analysis needs further work and will provide an interesting field of study to produce a size spectrum of the knee region.

The exact cause of difficulties with the shower analysis is not known. The assumption has been made that the NKG function is the best available fitting function for the shower lateral

# APPENDIX 1

## Matrix Algebra for Shower Arrival Direction Analysis

The projection of the shower direction vector, $\bar{e}$, onto the hut location vector, $\bar{r}_i$, is given by:

$$\bar{e} \cdot \bar{r}_i = c\,(\,t_i - t_{in}\,)$$

$$= -(l(x_i - x_{in}) + m(x_i - y_{in}))$$

So that $\quad c\,(t_i - t_{in}\,) = -\,(\,l(x_i - x_{in}) + m(y_i - y_{in})\,)$

Then the least squares fit parameter, S, is defined as follows:

$$S = \sum_i \left(\,c(t_i - t_{in}) + l(x_i - x_{in}\,) + m(y_i - y_{in})\,\right)^2$$

Minimising S with respect to $l$ and $m$ leads to solvable equations in $l$ and $m$.

i.e. $$\frac{\delta S}{\delta l} = 2\sum_i \left(\,c(t_i - t_{in}) + l(x_i - x_{in}) + m(y_i - y_{in})\right)\;(x_i - x_{in})$$

and $$\frac{\delta S}{\delta m} = 2\sum_i \left(\,c(t_i - t_{in}) + l(x_i - x_{in}) + m(y_i - y_{in})\right)\;(y_i - y_{in})$$

These partial derivatives must both equal zero for S to be a minimum. Therefore:

$$c\sum_i(t_i-t_{in})(x_i-x_{in}) \;+\; l\sum_i(x_i-x_{in})^2 \;+\; m\sum_i(y_i-y_{in})(x_i-x_{in}) \;=\; 0$$

and

$$c\sum_i(t_i-t_{in})(y_i-y_{in}) \;+\; l\sum_i(x_i-x_{in})(y_i-y_{in}) \;+\; m\sum_i(y_i-y_{in})^2 \;=\; 0$$

These two equations in $l$ and $m$ are best written in matrix form:

$$\begin{bmatrix} \sum_i (x_i - x_{in})^2 & \sum_i (x_i - x_{in})(y_i - y_{in}) \\ \sum_i (x_i - x_{in})(y_i - y_{in}) & \sum_i (y_i - y_{in})^2 \end{bmatrix} \begin{bmatrix} l \\ m \end{bmatrix} = -c \begin{bmatrix} \sum_i (t_i - t_{in})(x_i - x_{in}) \\ \sum_i (t_i - t_{in})(y_i - y_{in}) \end{bmatrix}$$

This matrix equation can be rewritten as follows:

$$A\,X = B$$

The solution to this equation is given by:

$$X = A^{-1}\,B$$

where $A^{-1}$ is the inverse of matrix A.

For a 2 x 2 matrix of the form:

$$AA = \begin{bmatrix} a & b \\ c & d \end{bmatrix}$$

$$\text{then} \quad AA^{-1} = \frac{1}{(ad-bc)} \begin{bmatrix} d & -b \\ -c & a \end{bmatrix}$$

$$\text{Hence } A^{-1} = \frac{\begin{bmatrix} \sum_i (y_i - y_{in})^2 & -\sum_i (x_i - x_{in})(y_i - y_{in}) \\ -\sum_i (x_i - x_{in})(y_i - y_{in}) & \sum_i (x_i - x_{in})^2 \end{bmatrix}}{\sum_i (x_i - x_{in})^2 \sum_i (y_i - y_{in})^2 - (\sum_i (x_i - x_{in})(y_i - y_{in}))^2}$$

To find the solution matrix ( X ) containing $l$ and $m$, the matrix multiplication $A^{-1} B$ is performed.

Hence X =

$$-c\,\frac{\begin{bmatrix} \sum_i (y_i-y_{in})^2 \sum_i (t_i-t_{in})(x_i-x_{in}) - \sum_i (x_i-x_{in})(y_i-y_{in}) \sum_i (t_i-t_{in})(y_i-y_{in}) \\ \\ \sum_i (x_i-x_{in})^2 \sum_i (t_i-t_{in})(y_i-y_{in}) - \sum_i (x_i-x_{in})(y_i-y_{in}) \sum_i (t_i-t_{in})(x_i-x_{in}) \end{bmatrix}}{\sum_i (x_i-x_{in})^2 \sum_i (y_i-y_{in})^2 - \left(\sum_i (x_i-x_{in})(y_i-y_{in})\right)^2}$$

The direction cosines, $l$ and $m$, can then be calculated as follows:

$$l = -c\,\frac{(\sum_i (y_i-y_{in})^2 \sum_i (t_i-t_{in})(x_i-x_{in}) - \sum_i (x_i-x_{in})(y_i-y_{in}) \sum_i (t_i-t_{in})(y_i-y_{in})}{\sum_i (x_i-x_{in})^2 \sum_i (y_i-y_{in})^2 - \left(\sum_i (x_i-x_{in})(y_i-y_{in})\right)^2}$$

And

$$m = -c\,\frac{\sum_i (x_i-x_{in})^2 \sum_i (t_i-t_{in})(y_i-y_{in}) - \sum_i (x_i-x_{in})(y_i-y_{in}) \sum_i (t_i-t_{in})(x_i-x_{in})}{\sum_i (x_i-x_{in})^2 \sum_i (y_i-y_{in})^2 - \left(\sum_i (x_i-x_{in})(y_i-y_{in})\right)^2}$$

densities follow Poisson statistics the standard deviation, $\sigma_i$, can be replaced with $( \rho_i )^{1/2}$. Hence the variance, $\sigma_i^2 = \rho_i$ so that the weights, $w_i = 1/\rho_i$.

To find the shower size the value of A must be found. This is done by minimising $\chi^2$ with respect to A, as follows:

$$\frac{\delta\chi^2}{\delta A} = \sum_i w_i \, 2( \rho_i - A \, f( \frac{r_i}{r_o} ) ). -f( \frac{r_i}{r_o} ) ) = 0 \quad \text{for minimum}$$

Rearranging this leads to:

$$A = \frac{\sum_i w_i \, \rho_i \, f( \frac{r_i}{r_o} )}{\sum_i w_i \, [ f( \frac{r_i}{r_o} ) ]^2}$$

That is:

$$A = \frac{\sum_i w_i \, \rho_i \, \frac{e^{-r_i/r_o}}{r_i/r_o}}{\sum_i w_i \left( \frac{e^{-r_i/r_o}}{r_i/r_o} \right)^2}$$

Hence the shower size, Ne, is given by $2 \pi r_o^2 A$.

(b) Using The NKG Lateral Distribution Function

The notation used in section (a) can be similarly applied to the NKG function as follows:

$$\rho_{i\ calc} (r_i) = \frac{Ne \; f(r_i/r_m)}{r_m^2}$$

where the constant $r_m$ = 79 m for air at sea level

and the $r_i$ are as defined in part (a)

$$\text{and} \quad f\left(\frac{r_i}{r_m}\right) = C(s)\left(\frac{r_i}{r_m}\right)^{s-2.0}\left(1+\frac{r_i}{r_m}\right)^{s-4.5}$$

With C(s), a normalising factor involving the Gamma function, as defined section in 1.4 (e)

The chi-squared function is written as follows:

$$\chi^2 = \sum_i w_i \left[ \rho_i - \frac{Ne}{(r_m)^2} \cdot f\left(\frac{r_i}{r_m}\right) \right]^2$$

with the weights, $w_i = 1/\rho_i$

Now minimising $\chi^2$ with respect to Ne gives:

$$\frac{\delta\chi^2}{\delta Ne} = \sum_i w_i\, 2 \left[ \rho_i - \frac{Ne}{(r_m)^2} f\left(\frac{r_i}{r_m}\right) \right] \cdot -(1/r_m^2)\, f\left(\frac{r_i}{r_m}\right) = 0$$

so that

$$Ne = (r_m)^2 \cdot \frac{\sum_i w_i\, \rho_i\, f\left(\frac{r_i}{r_m}\right)}{\sum_i w_i \left[ f\left(\frac{r_i}{r_m}\right) \right]^2}$$

with $f\left(\frac{r_i}{r_m}\right)$ as defined above.

# REFERENCES

Abdullah M.M., Ashton F. and Fatemi J. (1981) Proc. 17th ICRC (Paris), 6 151.

Abulova V.G., Dezhurko M.D., Mandritskaya K.V., Rakobolskaya I.V., Sazhina G.P., Zamchalova E.A. and Zatsepin V.I. (1981) Proc. 17th ICRC (Paris), 2, 114.

Acharya B.S., Rao M.V.S., Sivaprasad K. and Rao S. (1979) Proc. 16th ICRC (Kyoto), 9 109.

Acharya B.S., Naranan S., Rao M.V.S., Sivaprasad K. and Streekantan B.V. (1981) Proc. 17th ICRC (Paris), 11 385.

Acharya B.S., Rao M.V.S., Sivaprasad K. and Sreekantan B.V. (1983) Proc. 18th ICRC (Bangalore), 9 191.

Aliev N.A., Alimov T.A., Kakhkharov M.K., Khakimov N.Kh., Makhmudov B.M., Rakhimova N.R., Tashpulatov R.T., Khristiansen G.B., Prosin V.V. and Zhukov V.Yu. (1985) Proc. 19th ICRC (La Jolla), 7 195.

Alimov T.A. et al. (10 co-authors) (1983) Proc. 18th ICRC (Bangalore), 11 387.

Andam A.A., Chantler M.P., Craig M.A.B., McComb T.J.L., Orford K.J., Turver K.E. and Walley G.M. (1981) Proc. 17th ICRC (Paris), 11 281.

Antonov R.A. and Ivanenko I.P. (1975) Proc. 14th ICRC (Munich), 8 2708.

Asakimori K., Jogo N., Kameda T., Maeda T., Mizushima K., Toyoda Y. and Yoshida M. (1981) Proc. 16th ICRC (Kyoto), 8 247.

Ashton F., Nejabat H., Stewart T.R., Thompson M.G. and Treasure M.W. (1979a) Proc. 16th ICRC (Kyoto), 13 243.

Ashton F., Darjazi M.M.S., Nejabat H., Stewart T.R., Thompson M.G. and Treasure M.W. (1979b) Proc. 16th ICRC (Kyoto), 13 238.

Auger P., Maze R., and Grivet-Mayer T. (1938) C.R. Acad. Sci (Paris), 206 1721.

Auger P., Ehrenfest Jr. P., Maze R., Daudin J., Robley J. and Freon A. (1939) Rev. Mod. Phys., 11 288.

Awaya T. (1979) N.I.M., 165 317.

Baltrusaitis R.M., Cady R., Cassidy G.L., Cooper R., Elbert J.W., Gerhardy P.R., Ko S., Loh E.C., Salamon M., Steck D. and Sokolsky P. (1985a) N.I.M. (Phys.Res.Sect.A), A240 no.2 410.

Baltrusaitis et al. (1985b) (11 co-authors) Proc. 19th ICRC (La Jolla), 2 146.

Barthelmy, S.D., Israel, M.H. and Klarmann, J. (1985) Proc. 19th ICRC (La Jolla), 2 24.

Battistoni G. et al. (1985) (27 co-authors) Proc. 19th ICRC (La Jolla), 2 158.

Bell M.C., Kota J. and Wolfendale A.W. (1974) J. Phys., A7 420.

Benjamin J.R. and Cornell C.A. (1970) Probability Statistics and Decision for Civil Engineers. McGraw-Hill Book Company (New York).

Bevington P.R. (1969) Data Reduction and Error Analysis for the Physical Sciences. McGraw-Hill Book Company (New York).

Bothe, W. and Kolhörster, W. (1929) Physik Zeits., 56 751. for translation see Hillas A.M. (1972) Cosmic Rays, p161. Pergamon Press)

Bower A.J., Cunningham G., England C.D., Lloyd-Evans J., Reid R.J.O., Walker R. and Watson A.A. (1981) Proc. 17th ICRC (Paris), 9 166.

Bradt H.L., Clark G.W., La Pointe M., Domingo V., Kamata K., Murakami K., Suga K. and Toyoda Y. (1965) Proc. 9th ICRC (London), 2 715.

Burnett T.H. et al. (1982) ( 20 co-authors ) Workshop on Very High Energy Cosmic Rays, Univ. of Pennsylvania, 22-24 April 1982. M.L. Cherry et al. (eds) p220.

Burnett T.H. et al. (1985a) ( 26 co-authors ) Proc. 19th ICRC (La Jolla), 2 32.

Burnett T.H. et al. (1985b) ( 29 co-authors ) Proc. 19th ICRC (La Jolla), 2 48.

Catz Ph., Gawin J., Grochalska B., Hibner J., Hochart J.P., Milleret G., Stanczyk J. and Wdowczyk J. (1975) Proc. 14th ICRC (Munich), 12 4329.

Chan S.K. and Ng L.K. (1985) Proc. 19th ICRC (La Jolla), 7 131.

Chappell J.H. and Webber W.R. (1981) Proc. 17th ICRC (Paris), 2 59.

Chaudhuri N., Basak D.K., Goswami G.C. and Ghosh B. (1985) Proc. 19th ICRC (La Jolla), 7 101.

Cho C., Higashi S., Hiraoka N., Ozaki S., Sato T., Suwada T., Takahashi T. and Umeda H. (1985) Proc. 19th ICRC (La Jolla), 7 115.

Ciampa D. and Clay R.W. (1986) Proc. Astron. Soc. Aust. (in the press)

Clay J. (1927) Proc. Roy. Acad. of Amsterdam, 36 1115.

Clay R.W. and Gregory A.G. (1978) N.I.M., 153 p.471.

Clay R.W., Gerhardy P.R., Liebing D.F., Thornton G.J. and Patterson J.R. (1981) Nuo. Cim., 4C No. 6 668.

Clay R.W. and Gerhardy P.R. (1982a) Aust. J. Phys., 35 59.

Clay R.W. and Gerhardy P.R. (1982b) Aust. J. Phys., 35 441.

Cocconi G. (1961) Handbuch der Physik, XLVI(1) 215.

Compton A.H. (1932) Phys. Rev., 41 111 681.

Cowsik R. (1968) Can. J. Phys., 46 S142.

Cowsik R. and Wilson L.W. (1973) Proc. 13th ICRC (Denver), 3 500.

Cowsik R. and Wilson L.W. (1975) Proc. 14th ICRC (Munich), 9 195.

Cowsik R., Tonwar S.C., Viswanath P.R., Ellsworth R.W., Goodman J.A., Ito A.S., Streimatter R.E. and Yodh G.B. (1981) Proc. 17th ICRC (Paris), 2 120.

Crouch P.C., Gerhardy P.R., Patterson J.R., Clay R.W. and Gregory A.G. (1981) N.I.M., 179 467.

Cunningham G., Pollock A.M.T., Reid R.J.O. and Watson A.A. (1977) Proc. 15th ICRC (Plovdiv), 2 303.

Danilova T.V., Kabanova N.V., Nesterova N.M., Nikolskaya N.M., Nikolsky S.I., Katsarky L.M., Kirov I.N., Stamenov J.N. and Janminchev V.D. (1977) Proc. 15th ICRC (Plovdiv), 8 129.

Dawson B.R., Prescott J.R. and Clay R.W. (1985) Proc. 19th ICRC (La Jolla), 2 230.

De Beer J.F., Holyoak B., Wdowczyk J. and Wolfendale A.W. (1966) Proc. Phys. Soc., 89 567.

Dwyer R.D. and Meyer, P. (1981) Proc. 17th ICRC (Paris), 2 54.

Dyakonov et al. (1981) (13 co-authors) Proc. 17th ICRC (Paris), 6 106.

Eadie W.T., Drijard D., James F.E., Roos M., Sadoulet B. (1971) Statistical Methods in Experimental Physics. North Holland Pubs. (Amsterdam).

Earl J.A. (1961) Phys. Rev. Lett., 6 125.

Ehrenberg A.S.C. (1975) Data Reduction. John Wiley & Sons (London).

Eichten E., Hinchliffe I., Lane K. and Quigg C. (1984) Reviews of Modern Physics, 56 No.4 579.

Elbert J.W. (1982) Workshop on Very High Energy Cosmic Rays, Univ. of Pennsylvania, 22-24 April 1982. M.L. Cherry et al. (eds) p312.

Ellsworth R.W. (1977) Astr. Sp. Sci., 52 415.

Engelmann J.J. et al. (1983) ( 11 co-authors ) Proc. 18th ICRC (Bangalore), 2 17.

Engelmann J.J., Ferrando P., Koch-Miramond L., Masse P., Soutoul A. and Webber W.R. (1985) Proc. 19th ICRC (La Jolla), 2 4.

Feynman R.P. (1969) Phys. Rev. Lett., 23 1415.

Fowler P.H., Adams R.A., Cowen V.G. and Kidd J.M. (1967) Proc. Roy. Soc., 301 39.

Gaisser T.K., Protheroe R.J., Turver K.E. and McComb T.J.L., (1978) Revs. Mod. Phys., 50 (No. 4) 859.

Gaisser T.K. and Yodh G.B. (1980) Ann. Rev. Nuc. Part. Sci., 30 475.

Gerhardy P.R. (1983) PhD Thesis (Adelaide).

Giacconi R., Gursky H., Paolini F.R. and Rossi B. (1962) Phys. Rev. Lett., 9 439.

Goodman J.A. et al. (1982) (8 co-authors) Phys. Rev. D., 26 1043.

Gregory A.G. and Clay R.W. (1982) Local Publication.

Gregory J.C. et al. (1981) ( 24 co-authors ) Proc. 17th ICRC (Paris), 9 154.

Greisen K.G. (1956) Progr. Cosmic Ray Phys., 3 1.

Greisen K.G. (1960) Ann. Rev. Nuc. Sci., 10 63.

Grieder P.K.F. (1984) Nuo. Cim., 84A 285.

Grigorov N.L., Rapoport I.D., Savenko I.A., Nesterov V.E. and Prokhin V.L. (1971a) Proc. 12th ICRC (Hobart), 5 1760.

Grigorov N.L., Gubin Yu.V., Rapoport I.D., Savenko I.A., Yakovlev B.N., Akimov V.V. and Nesterov V.E. (1971b) Proc. 12th ICRC (Hobart), 5 1746.

Hammond R.T., Orford K.J., Protheroe R.J., Shearer J.A.L., Turver K.E., Waddoup W.D. and Wellby D.W. (1978) Nuo. Cim., 1C 315.

Hess V.F. (1912) Physik Zeits., 13 1084.

Hillas A.M. (1968) Can. J. of Physics, 46 S623.

Hillas A.M. (1970) Proc. 11th ICRC (Budapest), 29 Suppl. 3 355.

Hillas A.M. (1975) Physics Reports: Some Recent Developments in Cosmic Rays. Physics Letters, 20C 59.

Hillas A.M. and Lapikens J. (1977) Proc. 15th ICRC (Plovdiv), 8 460.

Hillas A.M. (1979) Proc. 16th ICRC (Kyoto), 8 7.

Hillas A.M. (1981a) Proc. 17th ICRC (Paris), 13 69.

Hillas A.M. (1981b) Proc. 17th ICRC (Paris), 2 125.

Hillas A.M. (1983) Proceedings of the Cosmic Ray Workshop Univ. of Utah, 10-14 Jan 1983., T.K. Gaisser (ed) p. 1.

Hillas A.M. (1984) Ann. Rev. of Astron. and Astroph., 22 425.

Hodson A.L., Porter M.R., Ash A.G. and Bull R.M. (1983) Proc. 18th ICRC (Bangalore), 11 201.

Israel M.H. (1981) Proc. 17th ICRC (Paris), 12, 53.

James F.E. and Roos M. (1975) Computer. Phys. Comm., 10 343.

Johnson T.H. (1933) Phys. Rev., 43 834.

Kakimoto F., Tsuchimoto I., Enoki T., Suga K. and Nishi K. (1985) Proc. 19th ICRC (La Jolla), 7 324.

Kalmykov N.N., Nechin Yu.A., Prosin V.V., Fomin Yu.A., Khristiansen G.B., Berezhko I.A., Grigoriev V.M. and Efimov N.N. (1979) Proc. 16th ICRC (Kyoto), 9 73.

Kamata K. and Nishimura J. (1958) Progr. Theor. Phys., Suppl. 6 93.

Karakula S., Osborne J.L. and Wdowczyk J. (1974) J. Phys., A7 437.

Kempa J., Wdowczyk J., and Wolfendale A.W. (1974) J. Phys., A7 1213.

Khristiansen G.B. (1979) Proc. 16th ICRC (Kyoto), 14 360.

Kolhörster W. (1914) Deutsch. Phys. Gesell. Verh., 16 719.

Krasilnikov D.D., Dyakonov M.N., Ivanov A.A., Kolosov V.A., Sleptsov I.Ye. (1983) Proc. 18th ICRC (Bangalore), 9 206.

Kraushaar W.L., Clark G.W. and Garmire G.R. (1968) Ap. J., 153 L203.

Kubiak G., Szabelski J., Wdowczyk J. and Wolfendale A.W. (1985) Proc. 19th ICRC (La Jolla), 7 16.

Lai K.F. and MacKeown P.K. (1981) Proc. 17th ICRC (Paris), 11 258.

La Pointe M., Kamata K., Gaebler J., Escobar I., Domingo V., Suga K., Murakami K., Toyoda Y. and Shibata S. (1968) Can. J. Phys., 46 S68.

Liebing D.F. (1983) PhD Thesis (Adelaide).

Liebing D.F., Clay R.W., Gregory A.G. and Patterson J.R. (1984) J.Phys. G:Nucl.Phys., 10 1283.

Linsley J. and Watson A.A. (1981) Proc. 17th ICRC (Paris), 2 137.

Longair M.S. (1981) High Energy Astrophysics. p. 115 Cambridge University Press (Cambridge).

McCusker C.B.A. (1967) Proc. 10th ICRC (Calgary), Part A 397.

McCusker C.B.A. (1975) Physics Reports, 20C 229.

Meyer J.P. (1981) Proc. 17th ICRC (Paris), 2 265.

Morello C., Navarra G. and Vernetto S. (1983) Proc. 18th ICRC (Bangalore), 1 127.

Muller D. (1982) Workshop on Very High Energy Cosmic Rays, Univ. of Pennsylvania, 22-24 April 1982. M.L. Cherry et al. (eds) p448.

Nagano M., Hara T., Hatano Y., Hayashida N., Kawaguchi S., Kamata K., Kifune T. and Mizumoto Y. (1984) J. Phys. G:Nucl. Phys., 10 1295.

Norman R.J. (1956) Proc. Phys. Soc., A69 804.

Ogato T. et al. (1981) (22 co-authors) Proc. 17th ICRC (Paris), 2 119.

Ostriker J.P. and Gunn J.E. (1969) Ap. J., 157 1395.

Peters B. (1961) Nuo. Cim., 22 800.

Pfotzer G. (1936) Physik Zeits., 102 23.

Porter M.R., Foster J.M., Hodson A.L., Hazen W.E., Hendel A.Z. and Bull R.M. (1981) Proc. 17th ICRC (Paris), 11 417.

Powell C.F., Fowler P.H. and Perkins D.H. (1959) The Study of Elementary Particles by the Photographic Method. Pergamon Press (London).

Prescott J.R. (1956) Proc. Phys. Soc., A69 870.

Prescott J.R., Clay R.W., Corani C.L., Dawson B.R., Gregory A.G. and Patterson J.R. (1983) Proc. 18th ICRC (Bangalore), 6 257.

Protheroe R.J., Clay R.W. and Gerhardy P.R. (1984) Ap.J., 280 L47.

Protheroe R.J. and Clay R.W. (1984) Proc. ASA, 5 (4) 586.

Protheroe R.J. and Clay R.W. (1985) Nature, 315 205.

Rao M.V.S. (1983) Proc. 18th ICRC (Bangalore), 12 p. 473.

Reid R.J. et al. (1961) Proc. Phys. Soc., 78 103.

Rossi B. (1964) Cosmic Rays. McGraw Hill Publishing Inc. (New York ).

Sato Y., Shimada E., Ohta I., Tasaka S., Tanaka S., Sugimoto H., Taira K. and Tateyama N. (1985) 19th ICRC (La Jolla), 2 36.

Schein M., Jesse W.P. and Wollen E.O. (1941) Phys. Rev., 59 515.

SimonM., Spiegelhauer H., Schmidt W.K.H., Siohan F., Ormers J.R. Balasubrahmanyan V.K. and Arens J.F. (1980) Ap.J., 239 712.

Skobelzyn D. (1929) Physik Zeits., 54 686.

Sood R. (1983) Nature, 301 44.

Stamenov J.N., Ushev S.Z., Janminchev V.D., Nikolskaja N.M. and Pavljuchenko V.P. (1983) Proc. 18th ICRC (Bangalore), 2 111.

Streimatter R.E., Balasubrahmanyan V.K., Ormes J.F. and Acharya B.S. (1985) Proc. 19th ICRC (La Jolla), 2 40.

Strong A.W., Wdowczyk J. and Wolfendale A.W. (1974) J. Phys, A7 1489.

Strugalski Z. (1983) Proc. 18th ICRC (Bangalore), 5 182.

Sun Louri and Winn M.M. (1984) N.I.M. in Phys. Res., 223 173.

Tang J. and Muller D. (1983) Proc. 18th ICRC (Bangalore), 9 251.

Thornton G.T. and Clay R.W. (1980) Phys. Rev. Lett., 44 959.

Thornton G.T. and Clay R.W. (1981) Phys. Rev. D., 23 No.9 2090.

Thornton G.J. (1984) PhD Thesis (Adelaide).

Tonwar S.C. (1982) Workshop on Very High Energy Cosmic Rays, Univ. of Pennsylvania, 22-24 April 1982. M.L. Cherry et al. (eds) p160.

Vernov S.N. and Khristiansen G.B. (1967) Proc. 10th ICRC (Calgary), Part A 345.

Watson A.A. and Walker R. (1981) J. Phys.G., 7 1297.

Webber W.R. (1982) Ap. J., 252 386.

Wilson C.T.R. (1901) Proc. Roy. Soc., 68 151.

Winn M.M., Ulrichs J., Peak L.S., McCusker C.B.A. and Horton L. (1986) J. Phys. G. (Nucl. Phys.), 12 653.

Wrontiak J.A. and Yodh G.B. (1985) Proc. 19th ICRC (La Jolla), 7 12.

Yodh G.B., Tonwar S.C., Goodman J.A. and Ellsworth R.W. (1982) Workshop on Very High Energy Cosmic Rays, Univ. of Pennsylvania, 22-24 April 1982. M.L. Cherry et al. (eds) p200.

Yodh G.B., Goodman J.A., Tonwar S.C. and Ellsworth R.W. (1983) Proc. 18th ICRC (Bangalore), 9 187.

Yodh G.B., Goodman J.A., Tonwar S.C. and Ellsworth R.W. (1984) Phys Rev D, 29 892.

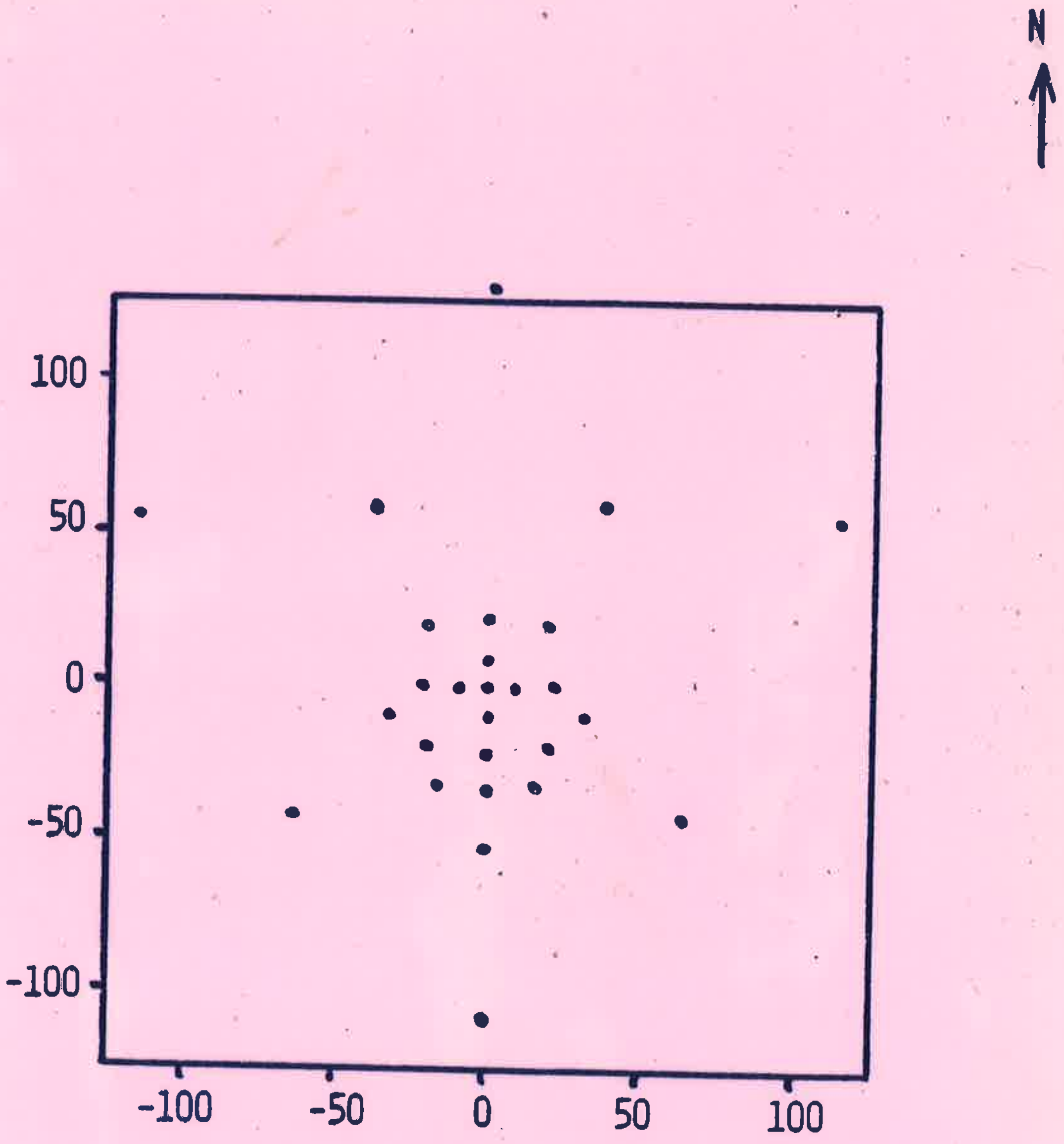
N
100
50
0
-50
-100
-100
-50
0
50
100